UTPP-79

Measurement of W+Photon Production in Proton-Antiproton Collisions at 1.96 TeV

Ai Nagano

February 2008

Measurement of W+Photon Production

in Proton-Antiproton Collisions at 1.96 TeV

Ai Nagano

(Doctoral Program in Physics)

Submitted to the Graduate School of
Pure and Applied Sciences
in Partial Fulfillment of the Requirements
for the Degree of Doctor of Philosophy
in Science

at the University of Tsukuba

Abstract

The measurement of the $W\gamma$ cross section, anomalous coupling limit and radiation amplitude zero are presented in this thesis.

The high p_T lepton data was collected at Collider Detector at Fermilab(CDF) in $p\bar{p}$ collisions at $\sqrt{s} = 1.96$ TeV. The total integrated luminosities are 1 fb^{-1}. The W bosons are selected in the lepton (electron or muon) decay channel. Photons are selected with $E_T^{\gamma} > 15$ GeV and $|\eta^{\gamma}| < 2.0$. The cross section is measured to be 7.36 ± 0.93 pb, in good agreement with the Standard Model prediction of 8.2 ± 0.6 pb. The photon E_T distribution constrains anomalous couplings at the $WW\gamma$ vertex.

Acknowledgments

I am grateful to my supervisor in University of Tsukuba, Prof. Fumihiko Ukegawa. Thanks also to $W\gamma Z\gamma$ analysis group members in Fermilab, Prof. Beate Heinemann, Prof. Al Goshaw, Prof. Tom Phillips, Jianrong Deng and Chris Lester, welcomed me in this group and support throughout $W\gamma$ analysis. This analysis would not be performed without Eric James's help assisted me especially with inclusive W cross section. I am thankful to Eva Halkiadakis, Mark Neubauer and Peter Renton in EWK, diboson group members, and also former members, Chris Hays and Elliot Lipeles, Shih-Chieh Hsu and Doug Benjamin who are the Monte Carlo coordinators, Raymond Culbertson, Maxim Goncharov and Shin-Shan Yu in photon group members who helped us achieving this result. Thank you to CDF-Japan group teachers, Prof. Shinhong Kim, Prof. Kazuhiko Hara, Prof. Takasumi Maruyama, Prof. Yuji Takeuchi, Dr. Tomonobu Tomura, Dr. Hideki Miyake, and Dr. Masakazu Kurata provided me nice advice. And finally I would like to thank to Fermilab colleagues and friends, Prof. Kunitaka Kondo, Dr. Koji Sato, Dr. Kohei Yorita, Dr. Takashi Akimoto, Dr. Masato Aoki, Dr. Yosiaki Kusakabe, Junji Naganoma, Naoki Kimura, Taichi Kubo, Tatsuya Masubuchi, Koji Nakamura, Takayuki Wakisaka, and Yoshikazu Nagai who shared good times at Fermilab.

Contents

List of Figures

List of Tables

Chapter 1

Introduction

The Standard Model [1, 2, 3] of electroweak interactions has been beautifully confirmed in recent years by many experimental results. In spite of these successes there still remain crucial parts of the model that lag behind in experimental verification. One of them is the vector-boson self-interacions which are uniquely given by the gauge structure of the Standard Model.

This chapter describes the theory of $W+$ photon production. A review of previous experimental results [16]-[48]is presented, as well.

1.1 The Standard Model

The Standard Model of elementary particles is a theory that describes three of the four known fundamental interactions between the elementary particles that make up all matter. The fundamental constituents of matter are the three generations of spin-1/2 fermions (quarks and leptons). The quarks and leptons participate in electroweak interactions, and the quarks also interact strongly. The interactions between fermions take place via the exchange of gauge bosons. The theory, describing the strong, weak and electromagnetic interactions, is a non-Abelian gauge theory based on the group $\mathrm{SU}(3)_C \times \mathrm{SU}(2)_I \times \mathrm{U}(1)_Y$. The group $\mathrm{SU}(3)_C$, which couples to the quantum number C, describes the strong force and is called Quantum Chromodynamics (QCD). The group $\mathrm{SU}(2)_I$ is analogous to the group of rotations for spin-1/2 particles, familiar from quantum mechanics. Instead of angular momentum, the quantum numbers associated with it are called weak isospin in the Standard Model. The photon is described by a $\mathrm{U}(1)_Y$ gauge theory. The electric charge Q, weak isospin $\vec{I}$, and

weak hypercharge Y are related by

$$Q = I_3 + \frac{1}{2}Y.$$

1.2 Gauge Theory

QED has the structure of an Abelian gauge theory with a symmetry group being U(1). The gauge field which mediates the interaction between the charged spin-1/2 fields is the electromagnetic field. Let us consider the Lagrangian describing a free Dirac fermion:

$$\mathcal{L}_0 = i\bar{\psi}(x)\gamma^\mu\partial_\mu\psi(x) - m\bar{\psi}(x)\psi(x).$$

where

- γ_μ are the Dirac matrices,
- ψ and its Dirac adjoint $\bar{\psi}$ are the fields representing electrically charged spin-1/2 particles

The Lagrangian $\mathcal{L}_0$ is invariant under the global U(1) transformation.

$$\psi(x) \to \psi'(x) \equiv \exp\{iQ\theta\}\psi(x),$$

where $Q\theta$ is an arbitrary real constant. This is called a global gauge transformation. The phase of $\psi(x)$ is then a pure convention-dependent quantity without physical meaning. However, the free Lagrangian is no longer invariant if one allows the phase transformation to depend on the space-time coordinate, i.e., under local phase redefinitions $\theta = \theta(x)$, because

$$\partial_\mu\psi(x) \to \exp\{iQ\theta(x)\}(\partial_\mu + iQ\partial_\mu\theta(x))\psi(x).$$

Thus once a given phase convention has been adopted at the reference point x_0, the same convention must be taken at all space-time points. This looks very unnatural.

The gauge principle is the requirement that the U(1) phase invariance should hold locally. One introduces a new spin-1 field $A_\mu(x)$, transforming as

$$A_\mu(x) \to A'_\mu(x) \equiv A_\mu(x) - \frac{1}{e}\partial_\mu\theta(x),$$

and defines the covariant derivative

$$D_\mu\psi(x) \equiv [\partial_\mu + ieQA_\mu(x)]\ \psi(x),$$

where

- $D_\mu = \partial_\mu + ieA_\mu$ is the gauge covariant derivative, with the coupling strength equal to the elementary charge
- A_μ is the covariant vector potential of the electromagnetic field

It has the required property of transforming like the field itself:

$$D_\mu\psi(x) \to (D_\mu\psi)'(x) \equiv exp\{iQ\theta(x)\}D_\mu\psi(x).$$

The Lagrangian

$$\mathcal{L} \equiv i\bar{\psi}(x)\gamma^\mu D_\mu\psi(x) - m\bar{\psi}(x)\psi(x) = \mathcal{L}_0 - eQA_\mu\bar{\psi}(x)\gamma^\mu\psi(x)$$

is then invariant under local U(1) transformation.
The new term corresponds to the interaction between the charged particle and the electromagnetic field, and its Feynman diagram is shown in Figure 1.1.

The QED Lagrangian including kinetic term of the photon field is

$$\mathcal{L} = \bar{\psi}(i\gamma^\mu D_\mu - m)\psi - \frac{1}{4}F_{\mu\nu}F^{\mu\nu}.$$

where

- $F_{\mu\nu} = \partial_\mu A_\nu - \partial_\nu A_\mu$ is the electromagnetic field tensor.

1.3 The Electroweak Theory

The standard electroweak model is based on the gauge group $G = \mathrm{SU}(2)_L \times \mathrm{U}(1)_Y$ [4, 5, 6], where L refers to the left-handed fermion fields. For simplicity, let us consider a single family of quarks, and introduce the notation

$$\psi_1(x) = \begin{pmatrix} u \\ d \end{pmatrix}_L,\ \psi_2(x) = u_R,\ \psi_3(x) = d_R$$

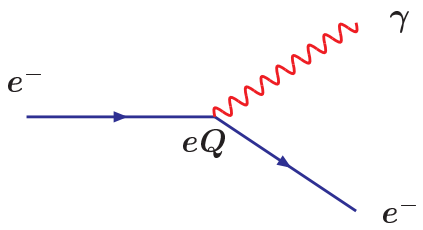

Figure 1.1: Feynman diagram of QED interaction.

Our discussion will also be valid for the lepton sector, with the identification

$$\psi_1(x) = \begin{pmatrix} \nu_e \\ e^- \end{pmatrix}_L , \ \psi_2(x) = \nu_{eR}, \ \psi_3(x) = e^-_R$$

As in the QED and QCD cases, let us consider the free Lagrangian

$$\mathcal{L}_0 = i\bar{u}(x)\gamma^\mu\partial_\mu u(x) + i\bar{d}(x)\gamma^\mu\partial_\mu d(x) = \sum_{j=1}^{3} i\bar{\psi}_j(x)\gamma^\mu\partial_\mu\psi_j(x).$$

$\mathcal{L}_0$ is invariant under global transformations in flavour space:

$$\begin{aligned} \psi_1(x) \to \psi_1'(x) &\equiv \exp\{iy_1\beta\}U_L\psi_1(x), \\ \psi_2(x) \to \psi_2'(x) &\equiv \exp\{iy_2\beta\}\psi_2(x), \\ \psi_3(x) \to \psi_3'(x) &\equiv \exp\{iy_3\beta\}\psi_3(x), \end{aligned}$$

where the $SU(2)_L$ transformation is defined as

$$U_L \equiv \exp\left\{i\frac{\sigma_i}{2}\alpha^i\right\} \quad (i = 1, 2, 3).$$

where σ_i is Pauli metrics,

$$\sigma_1 = \begin{pmatrix} 0 & 1 \\ 1 & 0 \end{pmatrix}, \sigma_2 = \begin{pmatrix} 0 & -i \\ i & 0 \end{pmatrix}, \sigma_3 = \begin{pmatrix} 1 & 0 \\ 0 & -1 \end{pmatrix}$$

and α_i is real numbers. The parameters y_i are called hypercharge, since the $\mathrm{U}(1)_Y$ phase transformation is analogous to the QED one.

We can now require the Lagrangian to be also invariant under the local $SU(2) \times U(1)$ gauge transformations. The following covariant derivative is introduced.

$$\begin{aligned} D_\mu\psi_1(x) &\equiv [\partial_\mu + ig\widetilde{W}_\mu(x) + ig' y_1 B_\mu(x)]\psi_1(x), \\ D_\mu\psi_2(x) &\equiv [\partial_\mu + ig' y_2 B_\mu(x)]\psi_2(x), \\ D_\mu\psi_3(x) &\equiv [\partial_\mu + ig' y_3 B_\mu(x)]\psi_3(x), \end{aligned}$$

where the gauge field of SU(2) is defined by

$$\widetilde{W}_\mu(x) \equiv \frac{\sigma_i}{2} W^i_\mu(x).$$

We want $D_\mu\psi_j(x)$ to transform in exactly the same way as the $\psi_j(x)$ fields; this fixes the transformation properties of the gauge fields:

$$\begin{aligned} B_\mu(x) \to B'_\mu &\equiv B_\mu(x) - \frac{1}{g'}\partial_\mu\beta(x), \\ \widetilde{W}_\mu \to \widetilde{W}'_\mu &\equiv U_L \widetilde{W}_\mu U_L^\dagger(x), \end{aligned}$$

where $U_L(x) \equiv \exp\{i\sigma_i\alpha^i(x)/2\}$. The Lagrangian

$$\mathcal{L} = \sum_{j=1}^{3} i\bar{\psi}_j(x)\gamma^\mu D_\mu\psi_j(x)$$

is invariant under local transformations. The interaction term has appeared.

In order to build the gauge-invariant kinetic term for the gauge fields, we introduce the corresponding field strengths:

$$\begin{aligned} B_{\mu\nu} &\equiv \partial_\mu B_\nu - \partial_\nu B_\mu, \\ \widetilde{W}_{\mu\nu} &\equiv -\frac{i}{g}\left[(\partial_\mu + ig\widetilde{W}_\mu), (\partial_\nu + ig\widetilde{W}_\nu)\right] \\ &= \partial_\mu\widetilde{W}_\nu - \partial_\nu\widetilde{W}_\mu + ig\left[W_\mu, W_\nu\right], \\ \widetilde{W}_{\mu\nu} &\equiv \frac{\sigma_i}{2} W^i_{\mu\nu}, \\ W^i_{\mu\nu} &= \partial_\mu W^i_\nu - \partial_\nu W^i_\mu - g\epsilon^{ijk} W^j_\mu W^k_\nu. \end{aligned}$$

$B_{\mu\nu}$ remains invariant under transformations, while $\widetilde{W}_{\mu\nu}$ transforms covariantly:

$$B_{\mu\nu} \to B_{\mu\nu},$$

$$\widetilde{W}_{\mu\nu} \to U_L \widetilde{W}_{\mu\nu} U_L^\dagger.$$

The gauge field part of the electroweak Lagrangian is

$$\mathcal{L} = -\frac{1}{4}(W^a_{\mu\nu} W^{a,\mu\nu} + B_{\mu\nu} B^{\mu\nu})$$

The charged W bosons are the linear combinations of W^1 and W^2, defined as

$$W^\pm_\mu \equiv \frac{1}{\sqrt{2}}(W^1_\mu \mp i W^2_\mu).$$

The Z boson (Z_μ) and the photon (A_μ) fields are mixtures of W_3 and B. The precise mixture is determined by the Weinberg angle θ_W [7, 8]:

$$Z_\mu = \cos\theta_W W^3_\mu - \sin\theta_W B_\mu,$$

$$A_\mu = \sin\theta_W W^3_\mu + \cos\theta_W B_\mu.$$

1.4 Theory of $W+$ photon production

The electroweak theory, being a non-Abelian gauge theory, has as the crucial consequence that triple and quadratic gauge boson couplings exist. The self-couplings of the W, Z, and γ are presented in the Standard Model. Since the field of strength $W^i_{\mu\nu}$ contain a quadratic piece, the Lagrangian gives rise to cubic and quartic self-interactions among the gauge theory. The Lagrangian of tri-linear interaction is described as

$$\begin{aligned}\mathcal{L}_{cubic} = ie\cot\theta_W\{&(\partial^\mu W^\nu - \partial^\nu W^\mu)W^\dagger_\mu Z_\nu - (\partial^\mu W^{\nu\dagger} - \partial^\nu W^{\mu\dagger})W_\mu Z_\nu + W_\mu W^\dagger_\nu(\partial^\mu Z^\nu - \partial^\nu Z^\mu)\} \\ &+e\{(\partial^\mu W^\nu - \partial^\nu W^\mu)W^\dagger_\mu A_\nu - (\partial^\mu W^{\nu\dagger} - \partial^\nu W^{\mu\dagger})W_\mu A_\nu + W_\mu W^\dagger_\nu(\partial^\mu A^\nu - \partial^\nu A^\mu)\}\}.\end{aligned}$$

The corresponding Feynman diagram of self-interaction is shown in Figure 1.2.

The leading order Feynman diagrams for $W + \gamma$ production in hadron-hadron collisions are shown in Figure 1.3. The two diagrams (t-channel and u-channel) arise from initial state radiation, where the photon radiated from incoming quark. In the s-channel diagram, which arises from the interesting triple gauge coupling, the photon is radiated from W boson.

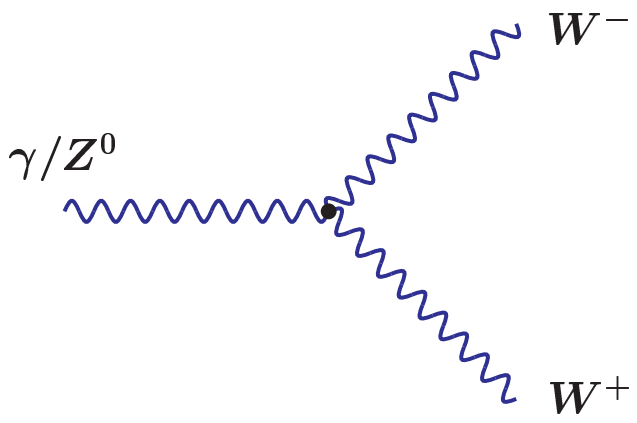

Figure 1.2: Feynman diagram of self-interaction among the gauge bosons.

The $W\gamma$ production is observed by using $W \to \ell\nu$ decay shown in Figure 1.4

The final state radiation, where the photon is radiated from the lepton in Bremsstrahlung process should also be considered.

The Lagrangian of $W + \gamma$ process [9, 10, 11] is given by

$$\mathcal{L}_{WW\gamma} = -ie[(W^{\dagger}_{\mu\nu}W^{\mu}A^{\nu} - W^{\dagger}_{\mu}W^{\mu\nu}A_{\nu}) + \kappa W^{\dagger}_{\mu}W_{\nu}F^{\mu\nu} + \frac{\lambda}{M^2_W}W^{\dagger}_{\lambda\mu}W^{\mu}_{\nu}F^{\nu\lambda}],$$

where

- e is the proton charge.
- M_W is the W boson Mass.

Here A^{μ} and W^{μ} are the photon and W^- fields, respectively, $W_{\mu\nu} = \partial_{\mu}W_{\nu} - \partial_{\nu}W_{\mu}$, $F_{\mu\nu} = \partial_{\mu}A_{\nu} - \partial_{\nu}A_{\mu}$.

All possible $WW\gamma$ interaction terms are described in the effective Lagrangian, obeying certain rules such as Lorentz invariance, as an extension to the Standard Model. CP violation terms are ignored in this thesis since they are not likely to produce observable effects. κ and λ do not violate any discrete symmetries. In the Standard Model, $\Delta\kappa \equiv \kappa - 1 = 0$ and $\lambda = 0$ are predicted. The deviation from the Standard Model would lead to new physics.

The couplings $\Delta\kappa$ and λ are related to the magnetic dipole moment, μ_W, and the electronic quadrupole moment, Q_W, of the W^+ boson:

$$\mu_W = \frac{e}{2M_W}(1+\kappa+\lambda),$$

$$Q_W = -\frac{e}{M_W^2}(\kappa-\lambda).$$

The cross section of the $W+\gamma$ process increases with the parton center-of-mass energy $\hat{s}$. Figure 1.5 shows the cross section of W^+W^- production in e^+e^- annihilation as a function of the center of mass energy $\sqrt{\hat{s}}$ [46]. At the tree level, the W-pair production process $e^+e^- \rightarrow W^+W^-$ involves three different contributions, corresponding to the exchange of ν_e, γ and Z. As shown in Figure 1.5, the ν_e-exchange contribution alone would lead to an unphysical growing of the cross section at large energies and, therefore, would imply a violation of unitarity. Adding the γ-exchange contribution softens this behavior, but a clear disagreement with the data persists. The Z-exchange mechanism, which involves the ZWW vertex, appears to be crucial in order to explain the data. Tree-level unitarity, e.g., for the process of $e^+e^- \rightarrow W^+W^-$, uniquely restricts the $WW\gamma$ couplings to their standard model gauge theory values at asymptotically high energies shown in Figure 1.5. If anomalous couplings are introduced, the cancellation caused by interference between initial state radiation and self-interaction process is ruined and the couplings are no longer restricted to their Standard Model values. This implies that any deviation from $a_f = \Delta\kappa, \lambda$ from the standard model expectation has to be described by a form factor $a_f(\hat{s}, q_W^2, q_\gamma^2)$ where $\sqrt{\hat{s}}$ is a center of mass, q_W^2 is the square of the four-momentum of the W boson, and the square of the four-momentum of the photon. The form factor vanishes when one of the arguments becomes large. In order to introduce these couplings and still produce physical results, the coupling a_f (=$\Delta\kappa$, λ) is assumed to be of the following form [12].

$$a_f(\hat{s}, q_W^2 = M_W^2, q_\gamma^2 = 0) = \frac{a_0}{(1+\hat{s}/\Lambda^2)^2}$$

where a_0 is either $\Delta\kappa$ or λ shown in the Lagrangian. The form scale factor Λ represents the scale at which new physics becomes observable in the weak boson sector due to compositness of the W boson [10]. For deviations of the three vector boson couplings from the gauge theory value, produced by some novel interactions operative at a scale Λ, one should expect that the form factors stay essentially constant for center of mass energies $\sqrt{\hat{s}} < \Lambda$ and start decreasing only when the scale Λ is reached or surpassed. Present experimental data suggests that Λ is

at least of the order of a few hundred GeV. Since the energy region covered by the Tevatron is smaller than typically expected for Λ we may assume the form factors $a_f = \Delta\kappa, \lambda$ ti be approximately constant in the following.

1.5 Limits on Anomalous couplings

The kinematic distributions of $W + \gamma$ are sensitive to anomalous couplings [13]. In all cases, the photon transverse momentum p_T distribution is the most powerful indicator of anomalous coupling [12]. Transverse momentum spectrum of the photon in the process $p\bar{p} \rightarrow W\gamma$, $W \rightarrow e\nu$ at the Tevatron, at a center-of-mass energy $\sqrt{s} = 1.8$ TeV is shown in Figure 1.6. Figure 1.6 demonstrates that anomalous couplings affect mainly the high photon p_T region. It shows events excess with setting $\Delta\kappa = 1$ or $\lambda = 0.5$. This can be easily understood by noting that the distributions of the mass $d\sigma/dM_{W\gamma}$ and the angular distribution $d\sigma/d\cos\theta$ where $\cos\theta$ is the angle between the photon and the incoming quark in the center of mass frame of the quark, both depend on the reconstructed neutrino longitudinal momentum which can only be determined with ambiguity, whereas this is not the case with the photon E_T.

A deviation from the standard model prediction, if large enough, will produce observable signature in $p\bar{p} \rightarrow W\gamma$. The anomalous coupling limits set by previous experiments are listed in Table 1.1. The $\Delta\kappa$ limits for $\lambda = 0$ and the λ limits for $\Delta\kappa = 0$ are listed here. These limits are at 95 % confidence level [47, 48]. Figure 1.7 shows the $\Delta\kappa$ and λ limit result obtained by CDF using the process $p\bar{p} \rightarrow W\gamma$ (integrated luminosity 200 pb^{-1}) and $p\bar{p} \rightarrow WW$ (350 pb^{-1}).

Experiment	$\Delta\kappa$	λ
DELPHI	$[-0.13, +0.68]$	$[-0.11, +0.23]$
ALEPH	$[-0.20, +0.26]$	$[-0.06, +0.14]$
L3	$[-0.08, +0.38]$	$[-0.14, +0.14]$
OPAL	$[-0.27, +0.07]$	$[-0.13, +0.01]$
CDF(200 pb^{-1})	$[-0.74, +0.73]$	$[-0.21, +0.19]$
D$\emptyset$ (135 pb^{-1})	$[-1.05, +1.04]$	$[-0.28, +0.27]$

Table 1.1: Summary of anomalous coupling limits at 95% C.L from previous measurements.

1.6 Radiation Amplitude Zero

The initial state radiation and s-channel diagrams interfere with each other and lead to "Radiation Amplitude Zero". The differential cross section of $q_i\bar{q_j} \to W^-\gamma$ is given by

$$\frac{d\sigma}{dt}(q_i\bar{q_j} \to W^-\gamma) = \frac{\alpha}{s^2}\frac{M_W^2 G_F}{\sqrt{2}} g_{ij}^2 \left\{ \left(Q_i + \frac{1}{1+t/u} \right)^2 \frac{t^2+u^2+2sM_W^2}{tu} \right.$$
$$+\Delta\kappa \left(Q_i + \frac{1}{1+t/u} \right) \frac{t-u}{t+u}$$
$$\left. + \frac{\Delta\kappa^2}{2(t+u)^2} \left[tu + (t^2+u^2)\frac{s}{4M_W^2} \right] \right\}$$

where s, t, and u are the Mandelstam variables.

$$t = -\frac{1}{2}(s - M_W^2)(1 - \cos\theta)$$

$$u = -\frac{1}{2}(s - M_W^2)(1 + \cos\theta)$$

$g_{ij} = \cos\theta_c$ for $q_i\bar{q_j} = d\bar{u}$ and $s\bar{c}$, and $g_{ij} = \sin\theta_c$ for $q_i\bar{q_j} = s\bar{u}$ and $d\bar{c}$. $Q_i|e|$ is the charge of the quark q_i and θ_c is Cabbibo angle. θ is the angle between γ and incoming quark, in the center-of-mass frame of $W\gamma$ shown in Figure 1.8. All quark masses have been neglected.

For definiteness, we will concentrate on $W^-\gamma$ production via the subprocess $d\bar{u} \to W^-\gamma$. In this case, the differential cross section is given by

$$\frac{d\sigma}{d\cos\theta}(d\bar{u} \to W^-\gamma) = \frac{1}{2}(s - M_W^2)\frac{d\sigma}{dt}(d\bar{u} \to W^-\gamma).$$

The Standard Model predicts the vanishing of $d\sigma/dt$ at a particular angle. This zero in

$d\sigma/dt$ can be traced to the coefficient

$$\left(Q_i + \frac{1}{1+t/u}\right)^2,$$

which vanishes for $t/u = -(1+1/Q_i)$, namely for

$$\cos\theta = -(1+2Q_i).$$

Since $Q_i = -1/3$ for the d quark, we get $\cos\theta = -1/3$ [14]. Figure 1.9 shows the differential cross section for the process $d\bar{u} \to W^-\gamma$ as a function of $\cos\theta$ in the $W\gamma$ frame.

In practice, however, this zero is difficult to observe. Structure function effects, higher-order QCD corrections and the finite W width tend to fill the dip. Experimentally, the unobservable longitudinal neutrino momentum, p_z^ν smears out the dip caused by the Standard Model radiation zero. Instead it has been proposed by U.Baur [15] to use the distributions of the difference in the lepton and photon pseudo-rapidities, is defined as

$$\Delta\eta(\ell,\gamma) = Q_\ell(\eta_\gamma - \eta_\ell),$$

where η_γ is the photon pseudo-rapidity and η_ℓ is the pseudo-rapidity of the lepton=(e, μ) originating from the W decay, Q_ℓ is the sign of the lepton charge. This quantity does not require the knowledge of the longitudinal momentum of the neutrino, and so one can be free from possible event misreconstruction problem. Figure 1.11 (right) exhibits a pronounced minimum for pseudo-rapidities satisfying $\Delta\eta(\gamma,\ell) = -0.3$. In the Standard Model, the dominant W helicity in $W^\pm\gamma$ production is $\lambda_W = \pm 1$ implying that the charged lepton tends to be emitted in the direction of the parent W, and thus reflects most of its kinematic property. The difference in rapidity between W boson and the lepton originating from W decay $\Delta y(W,\ell) = y(W) - y(\ell)$ is small on average. This is demonstrated in Figure 1.10 which shows $\Delta y(W,\ell)$ distributions with cuts listed in the following (solid line).

- $p_T(\gamma) > 5$ GeV, $|\eta(\gamma)| < 3.$,
- $p_T(\ell) > 20$ GeV, $|\eta(\ell)| < 3.5$,
- $\not{E}_T > 20$ GeV, $\Delta R(\gamma,\ell) > 0.7$,
- $M_T(\ell,\gamma,\not{E}_T) > 90$ GeV.

The distributions sharply peaks at $\Delta y(W,\gamma) = 0.3$. For approximately, 98% of all events, $|\Delta y(W,\ell)| < 1$. The W-lepton rapidity difference distribution is slightly asymmetric with respect to the peak position. This is due to the lepton and missing transverse momentum cuts, with favor events with small lepton rapidity. If the $p_T(\ell)$ and $\not\!\!E_T$ cuts are removed, the tail of the $\Delta y(W,\gamma)$ distribution extends to significantly higher positive rapidity difference (dashed line) with peak position remaining essentially unchanged. The production of $W\gamma$ Born approximation at the Tevatron is shown in Figure 1.11 (right). The double differential cross section, $d^2\sigma/dy_{(\gamma)}dy_{(W^+)}$ is shown in Figure 1.11 (left). In order to simulate the finite acceptance, the phase space region which covered by the CDF detector ($|\eta(\gamma)| < 3.$, $|\eta(\ell)| < 3.5$) is imposed. Uncertainty in energy measurements are simulated by Gaussian smearing of the particle four-momentum vector with standard deviation σ, corresponding to the detector resolution. The double differential distribution for rapidity difference in the photon and W boson and that in the photon and lepton are very similar.

In this analysis, we consider $\Delta\eta(\ell,\gamma)$ as tools to observe the radiation amplitude zero in the process $p\bar{p} \to W\gamma$.

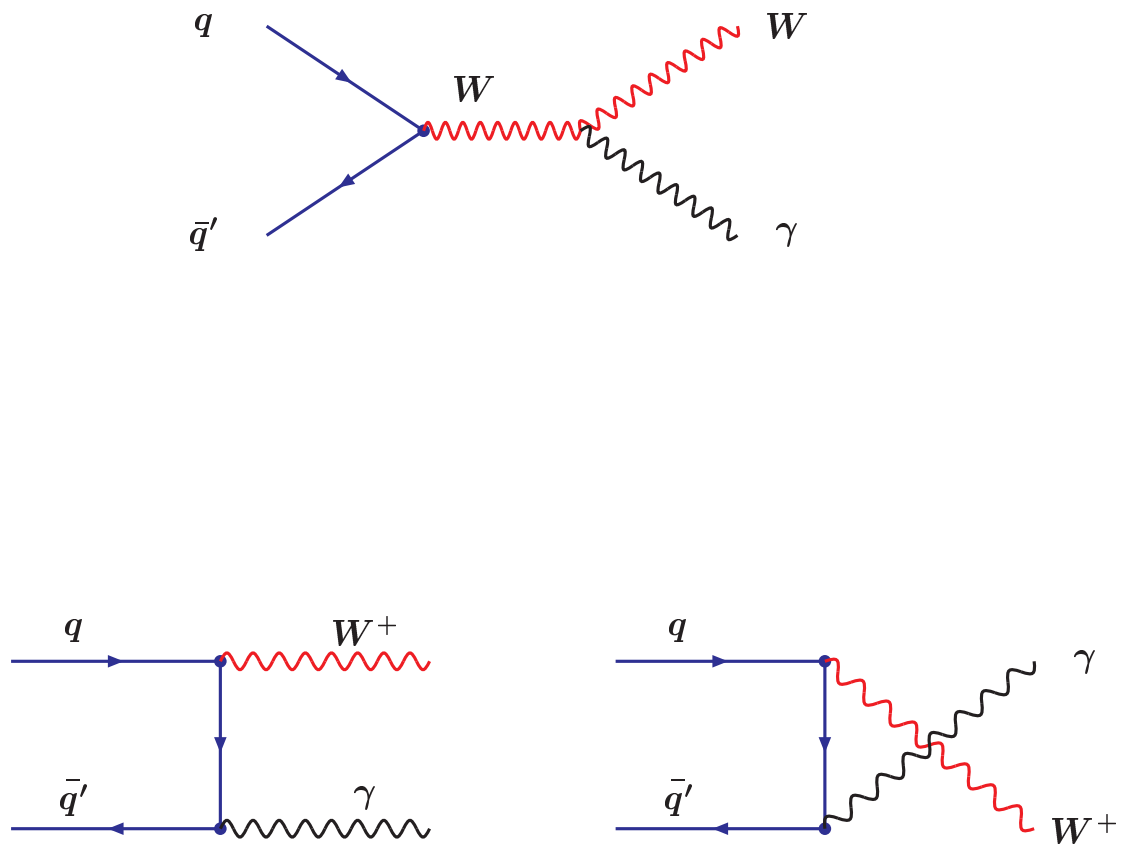

Figure 1.3: $W + \gamma$ leading order Feynman diagrams. Upper : s-channel. Lower left : t-channel. Lower right : u-channel.

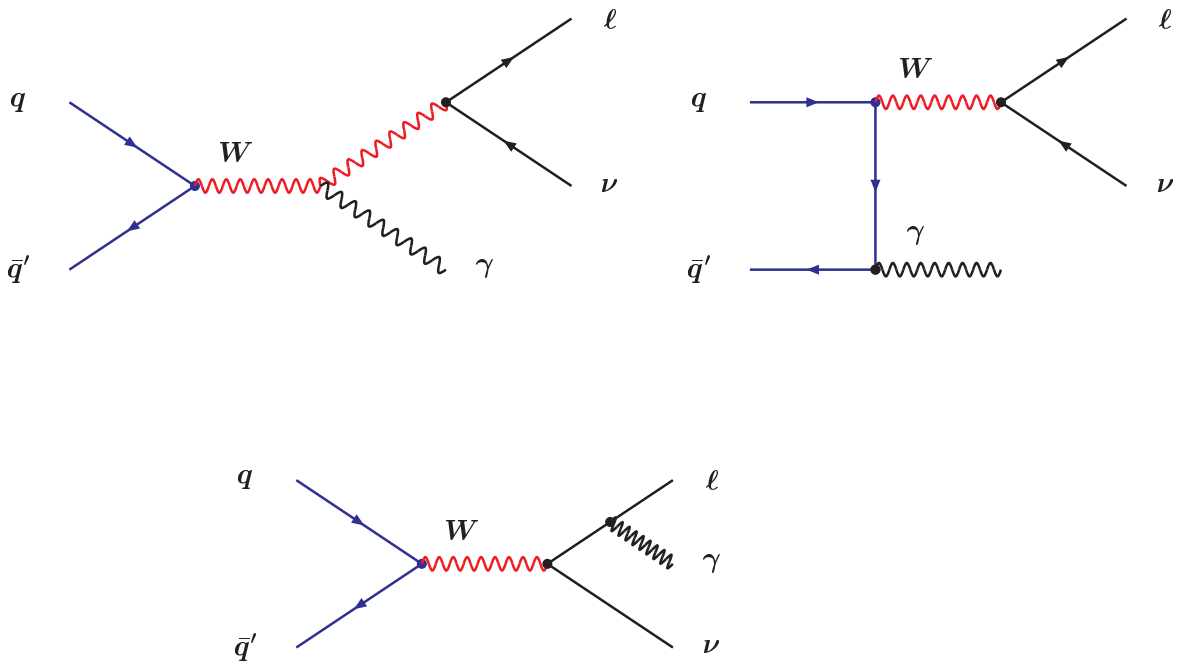

Figure 1.4: $W+\gamma$ leading order Feynman diagrams W decays to lepton and neutrino. Upper : s-channel. Upper left : t-channel. Lower : Photon is radiated from Bremsstrahlung process.

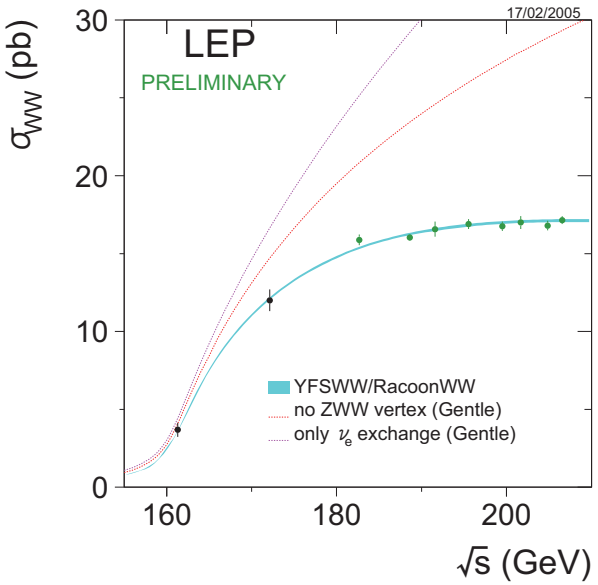

Figure 1.5: Measured energy dependence of $\sigma(e^+e^- \to W^+W^-)$. The three curves are shown for the W pair production corresponding to only the ν_e exchange contribution (upper curve), ν_e exchange plus photon exchange (middle curve), and all contributions including also the ZWW vertex (lower curve).

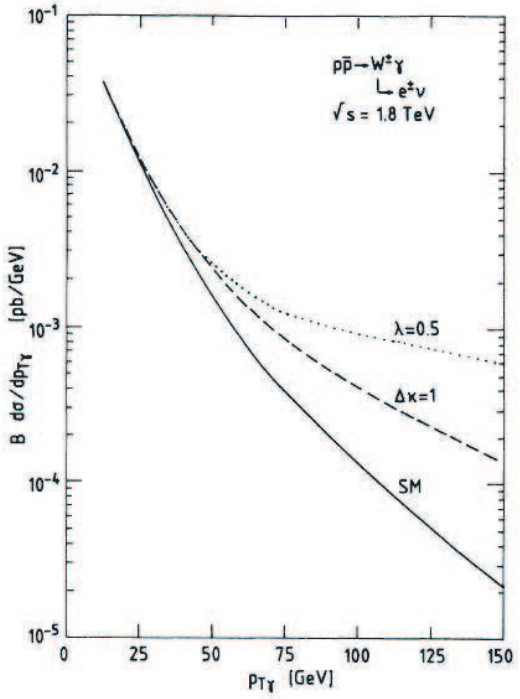

Figure 1.6: Transverse momentum spectrum of the photon in the process $p\bar{p} \to W\gamma, W \to e\nu$ at the Tevatron, at a center-of-mass energy $\sqrt{s} = 1.8$ TeV. The dotted line is the transverse momentum spectrum of $\lambda = 0.5$. The dashed line is the transverse momentum spectrum of $\Delta\kappa = 1$.

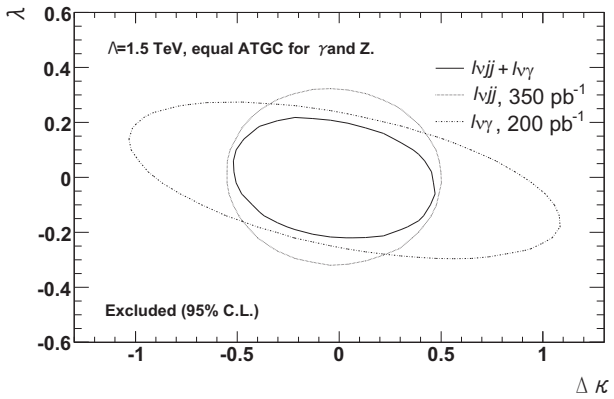

Figure 1.7: $\Delta\kappa$ and λ limit at CDF using the process $p\bar{p} \to W\gamma$ (200 pb^{-1}) and the process $p\bar{p} \to WW$ (350 pb^{-1}) The region is excluded at 95 % C.L.

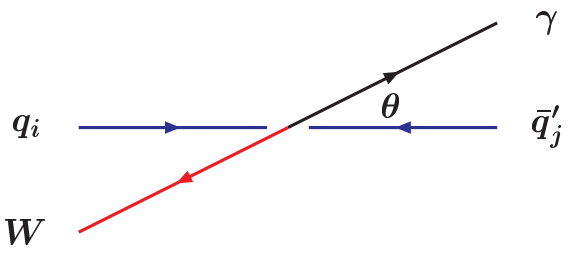

Figure 1.8: Definition of θ assuming $P_T(W\gamma) = 0$ in the center-of-mass frame of $W\gamma$.

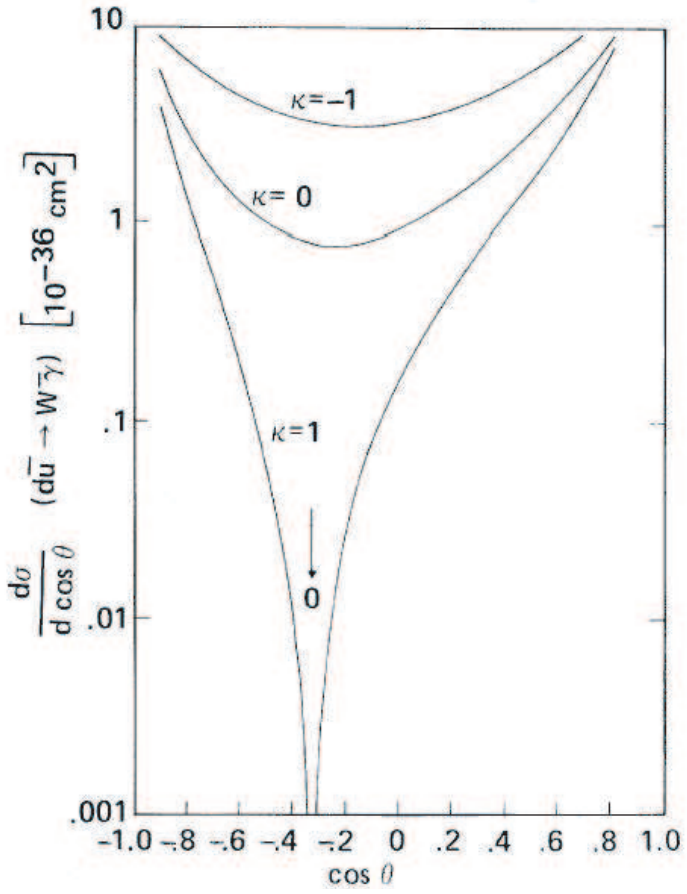

Figure 1.9: The differential cross section for $d\bar{u} \to W^-\gamma$. $\sqrt{s} = 200$ GeV and $M_W = 85$ GeV/c^2 are supposed.

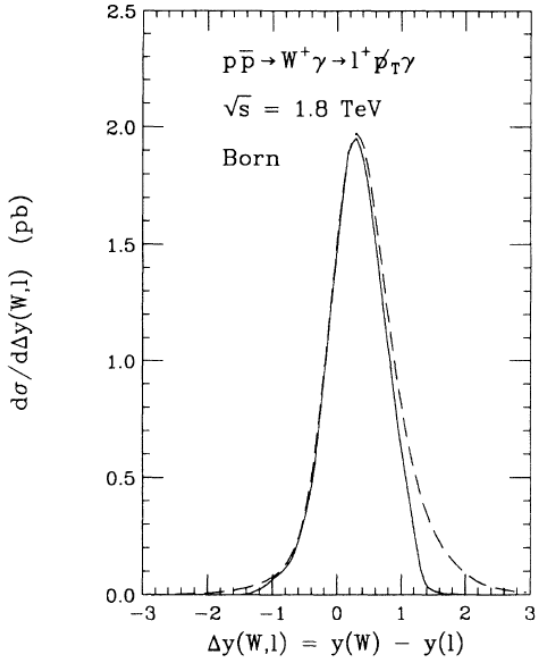

Figure 1.10: The W-lepton rapidity difference distribution, $d\sigma/d\Delta y(W,\ell)$ for $p\bar{p} \to W^+\gamma \to \ell^+\nu\gamma$ in the Born Approximation at the Tevatron. The solid line shows the result obtained for the cuts. The dashed line displays the rapidity difference distribution if the $p_T(\ell)$ and $\not{E}_T$ cuts are removed.

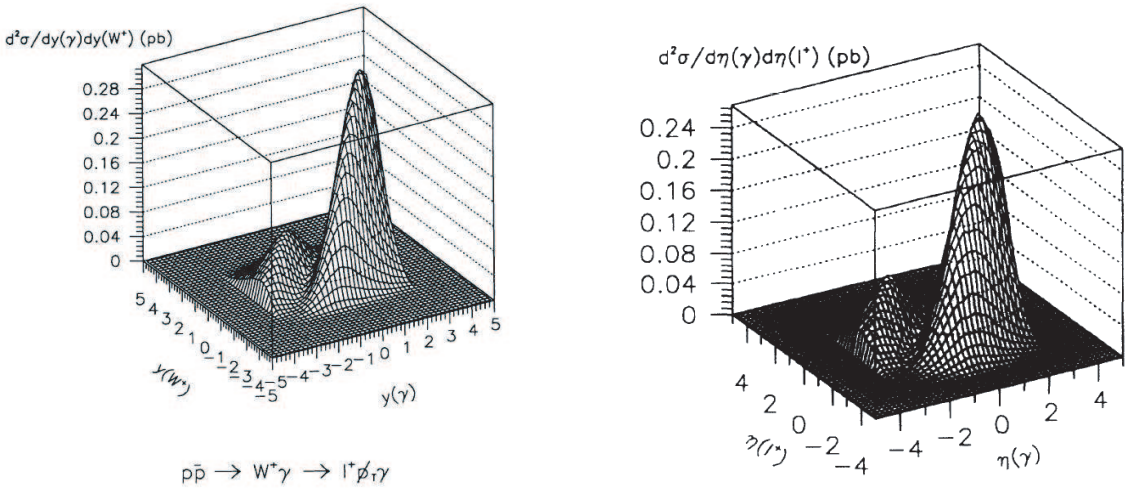

Figure 1.11: Left : The double differential distribution $d^2\sigma/d\eta_\gamma d\eta_{W^+}$ for $p\bar{p} \to W^+\gamma$. Right : The double differential distribution $d^2\sigma/d\eta_\gamma d\eta_{\ell^+}$ for $p\bar{p} \to W^+\gamma \to \ell^+\nu\gamma$. Born approximation at the Tevatron $\sqrt{s} = 1.8$ TeV [15].

Chapter 2

Experimental Apparatus

This analysis was performed using the Collider Detector at Fermilab (CDF), a general purpose experiment designed to study proton-antiproton collisions at $\sqrt{s} = 1.96$ TeV. The data used in this analysis is collected from February 2002 to February 2006. In this chapter, the Tevatron accelerator (proton-antiproton collider) and the CDF detector are described.

2.1 Tevatron Accelerator

The Tevatron is the proton antiproton accelerator at Fermi National Accelerator Laboratory. Its schematic layout is shown in Figure 2.1. Proton and antiprotons collide at a center-of-mass energy of $\sqrt{s} = 1.96$ TeV.

2.1.1 Preacc

The Pre-accelerator (Preacc) is the Cockcroft-Walton style electrostatic Pre-accelerator. It converts hydrogen gas to ionized hydrogen gas and accelerates to an energy of 750 keV.

Gaseous hydrogen is extracted from a small tank and injected into the ion source, out of which emerges H^- ions. These ions are extracted from the source at 18 keV and transferred to a Cockcroft-Walton electrostatic pre-accelerator (Preacc), which accelerates H^- to 750 keV. The acceleration process can be thought of roughly in the following terms: the dome containing H^- ions is held at an electric potential of 750 keV; a column connects the dome to a ground potential, and the ions rush toward through the column to achieve the final energy of 750 keV. According to nominal specifications, the source-accelerator system gives rise to pulses of H^- of current of 50 mA and pulse length of 30 seconds.

2.1.2 Linac

The Linear Accelerator (Linac) is the next level of acceleration and consists of a series of drift tubes. It takes 750 keV hydrogen ions to 400 MeV. The Linac consists of two main sections, the low energy drift tube Linac and the high-energy side coupled cavity Linac. The drift tube Linac makes up the first five radio-frequency (RF) stations. A large power amplifier tube powers each drift tube. These tubes amplify the 201 MHz RF signal used to drive the low energy cavities and accelerate H^- to 116 MeV. The last nine cavities are Klystron amplifiers operating at 805 MHz. The Linac can accelerate beam once every 66 milliseconds (a 15 Hz repetition rate).

2.1.3 Booster

The Booster consists of a series of magnets around 75 meters in radius with 18 RF cavities interspersed. The Booster is made up of 96 combined function magnets in a series of 24 repeating periods. Their magnetic field varies from about 740 gauss at injection to 7,000 gauss at extraction. The Booster tunnel is a concrete tunnel 8 feet high and 10 feet wide, covered by 15 feet of earth shielding. It strips off electrons from 400 MeV hydrogen ion and makes proton accelerate to 8 GeV. The ionized hydrogen beam passes through a carbon foil which removes the electrons leaving bare protons.

2.1.4 Main Injector

The Main Injector is a circular synchrotron. It can accelerates 8 GeV proton to 120 GeV or 150 GeV. The Main Injector has 18 accelerating cavities. As well as accepting protons from the Booster, the Main Injector can accept antiprotons from the Antiproton Source. The Main Injector can accelerate beam as fast as every 2.2 seconds.

2.1.5 $\bar{p}$ production

The 120 GeV beam extracted from the Main Injector strikes a nickel target. Out of the spray of random secondary particles, 8 GeV antiprotons are taken.

The largest bottleneck in a proton-antiproton collider is the time required to accumulate the required number of antiprotons. The process is inherently inefficient. Typically for every 10^5 protons striking a target, only one or two antiprotons are captured and stored.

The antiproton Source is comprised of a target station, two rings called the Debuncher and Accumulator. The incident beam is focused to a small spot size using a series of quadrupole magnets. The beam strikes the nickel production target. The resulting cone of secondary particles is focused and rendered parallel by means of a Lithium lens known as the "Collection Lens". A pulsed dipole magnet bends all negatively-charged particles of approximately 8 GeV kinetic energy into the line to the Debuncher while most of the other particles are absorbed within a beam dump. The survived particles are injected into the Debuncher where the momentum spread of the 8 GeV beam of secondaries is reduced. Just before the next pulse arrives from the target, the antiprotons are extracted from the Debuncher and injected into the Accumulator. The purpose of the Accumulator is to accumulate antiprotons. This is accomplished by momentum stacking successive pulses of antiprotons from the Debuncher over several hours or days. Both RF and cooling systems are used in the momentum stacking process. The RF decelerates the recently injected pulses of antiprotons from the injection energy. Cooling systems keep the antiprotons at the desired momentum and minimize the transverse beam size.

2.1.6 Tevatron

The Tevatron is a circular synchrotron with a circumference of approximately 4 miles. It accelerates protons or antiprotons from 150 GeV to 980 GeV. It receives 36 proton and 36 antiproton bunches with a minimum spacing of 392 ns. The protons and antiprotons share the same ring and move in the opposite directions.

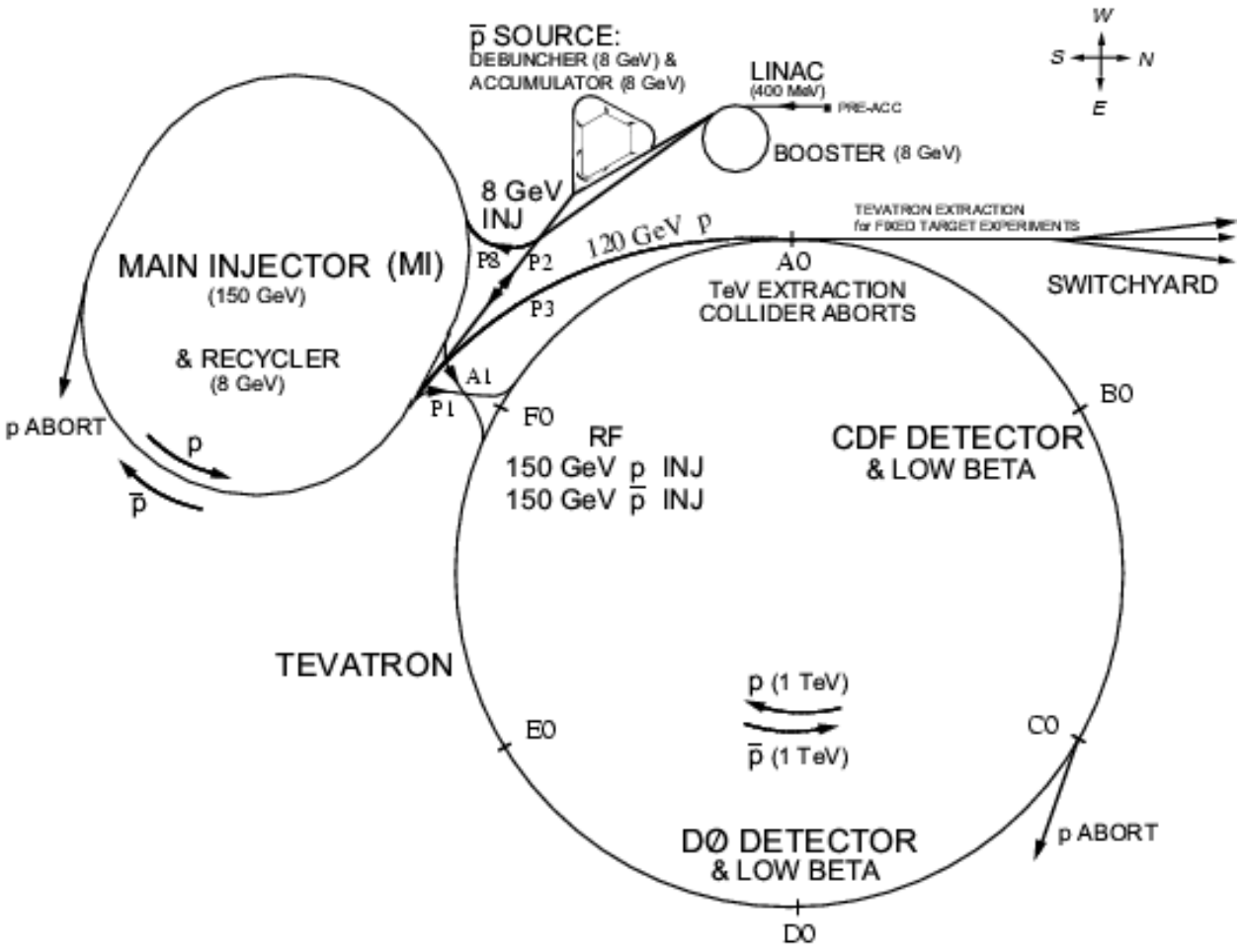

Figure 2.1: Tevatron Accelerator with a circumference of approximately 4 miles which accelerates protons or antiprotons from 150 GeV to 980 GeV. The protons and antiprotons share the same ring. The protons travel clockwise.

2.2 CDF Detector

The data used in this analysis was collected with the Collider Detector at Fermilab (CDF) [49]. The CDF detector is a complex device that consists of many subdetectors as shown in Figure 2.2 and Figure 2.3. It is cylindrically symmetric around the beam axis and forward-backward symmetric about the interaction region. It is a general purpose solenoidal detector which combines precision charged particle tracking with fast projective calorimetry and fine grained muon detection. Tracking systems are contained in a superconduction solenoid, 1.5 m in radius and 4.8 m in length, which generates a 1.4 T magnetic field parallel to the beam axis. Calorimetry and muon systems are all located outside the solenoid. We use a coordinate system where the polar angle θ is measured from the proton direction, the azimuthal angle ϕ is measured from the horizontal plane going toward the outside of the Tevatron, and the pseudo-rapidity is defined as $\eta = -\ln(\tan(\theta/2))$.

2.2.1 Tracking System

Silicon Detectors

The silicon detector system provides high precision tracking of charged particles near the interaction point. The silicon tracking system consists of three subdetectors, Layer00 (L00), the Silicon Vertex Detector (SVX II) and the Intermediate Silicon Layers detector (ISL). Figure 2.4 illustrates the silicon detector geometry in the plane transverse to the beam axis.

L00 is placed in the innermost part at a radius of 1.35 cm [50]. It consists of single-sided micro-strip silicon detectors. The position resolution is 21 μm for low p_T ($2-3$ GeV/c) track and 11 μm for high p_T track.

SVX II is placed outside of L00 [51]. The radial coverage is from 2.4 cm to 10.7 cm and the total length is 96 cm. It consists of three barrels. Each barrel has five layers of double-sided silicon micro-strip detector. Rapidity coverage is $|\eta| < 2.0$. The resolution is 12 μm.

ISL is located between SVX II and COT [52]. It consists of the central detector at radius of 23 cm, and the two forward detectors at radius from 20 cm and 29 cm. The impact parameter resolution is 40 μm using both SVX and ISL. The collision location in z-axis (Z_0) resolution is 70 μm using both SVX and ISL.

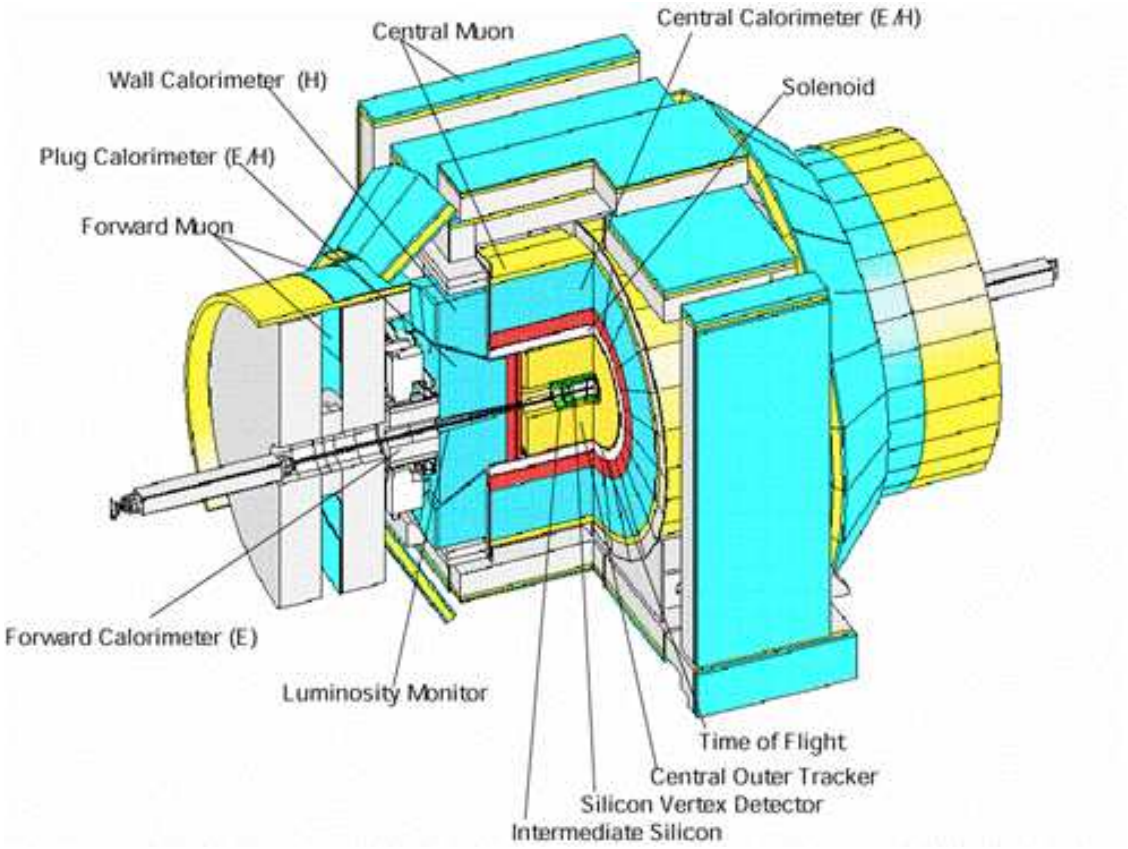

Figure 2.2: The cutaway view of CDF detector

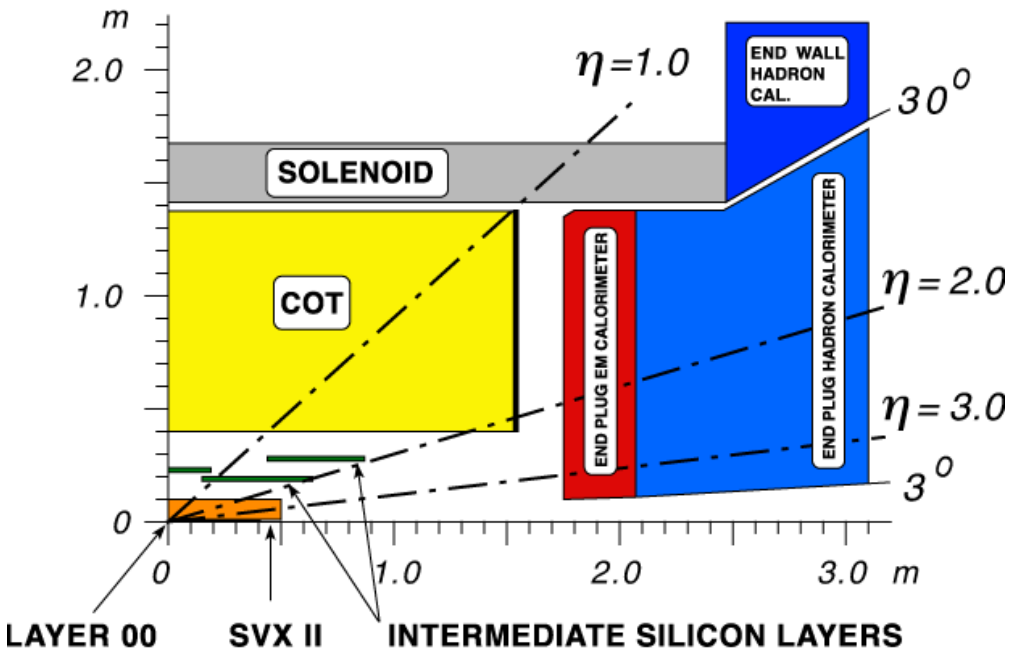

Figure 2.3: The longitudinal view of the CDF tracking system representing a quarter of the detector.

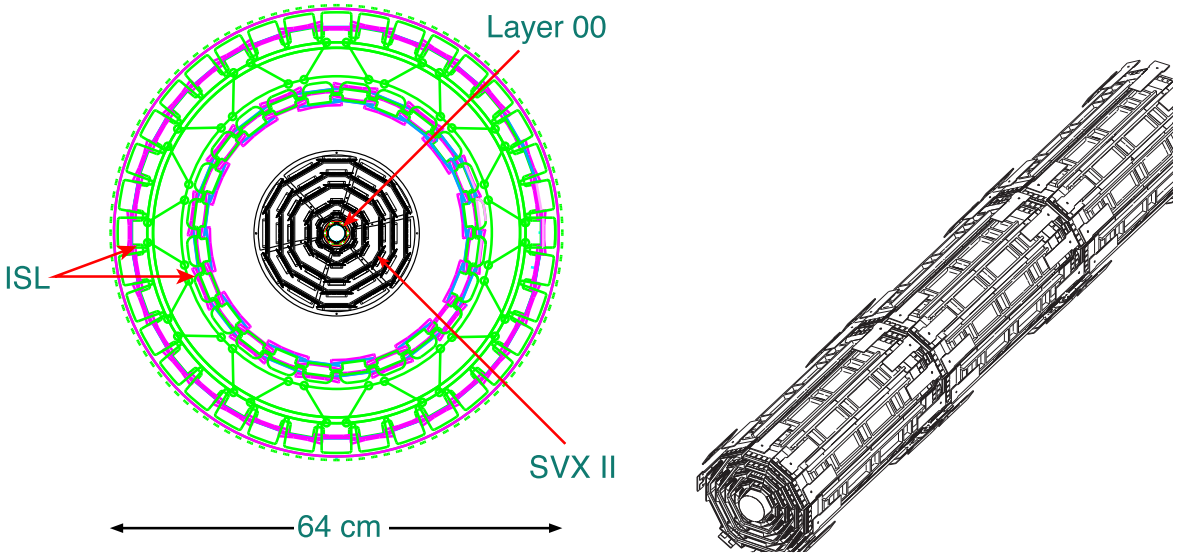

Figure 2.4: The silicon detector geometry in $r-\phi$ end view (left) and the view of three barrels of SVX II(right).

Central Outer Tracker (COT)

Outside of the silicon detector, the Central Outer Tracker (COT) covers the region $|\eta| < 1$ with a radial range from 40 cm to 137 cm [53]. It is the drift chamber filled with a gas mixture of Argon 50 %, Ethane 35 %, and CF_4 15 %. Figure 2.5 illustrates the COT detector geometry. COT has 96 layers grouped into eight super-layers. Each super layer consists of 12 sense wires and 13 potential wires. Four stereo super-layers and four axial super-layers are placed with crossing angle $\pm$ 2 °. Hit position resolution is about 140 micro-meters. The momentum resolution is $\sigma_{p_T}/p_T^2 = 0.015$ $(\mathrm{GeV}/c)^{-1}$ in high p_T region.

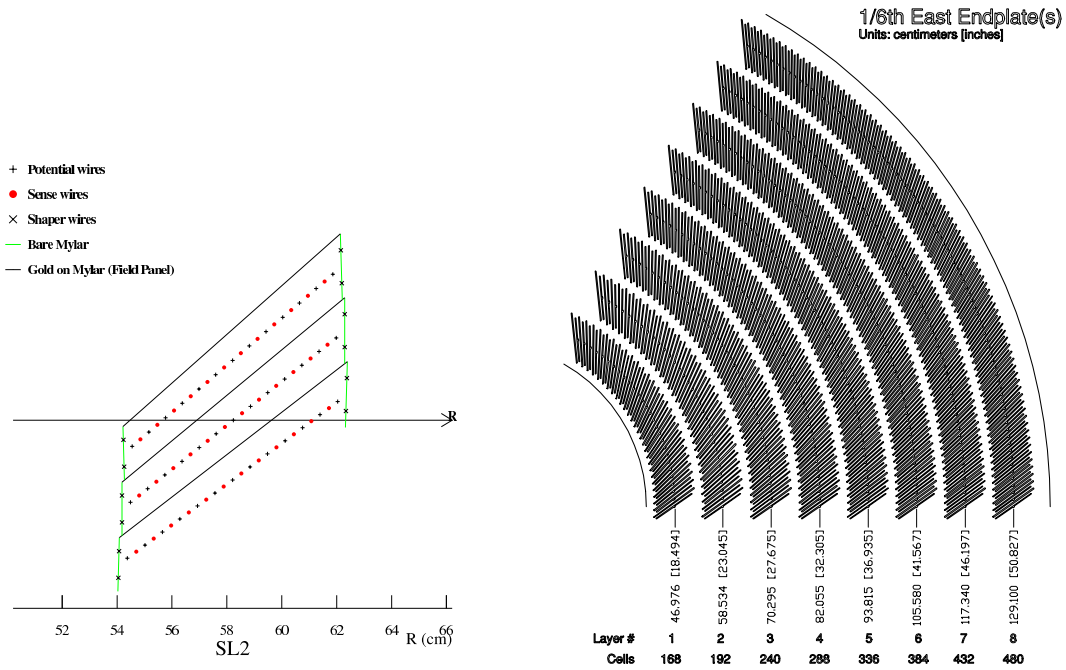

Figure 2.5: Three cells in COT detector along the beam direction (left) and 1/6 section of th COT end plate (right).

2.2.2 Calorimeters

Calorimeters are used to measure the energy of both charged and neutral particles. The CDF calorimeter consists of two sections : a central barrel calorimeter ($|\eta| < 1.1$) and the forward end-plug calorimeter ($1.1 < |\eta| < 3.6$).

Central Electromagnetic Calorimeter (CEM)

The Central Electromagnetic Calorimeter is a lead-scintillator sampling calorimeter system with projective tower geometry shown in Figure 2.6. Each tower covers 15 ° in ϕ. It covers $|\eta| < 1.1$ [54]. The energy resolution σ_E/E is $13.5\%/\sqrt{E(\text{GeV})}$.

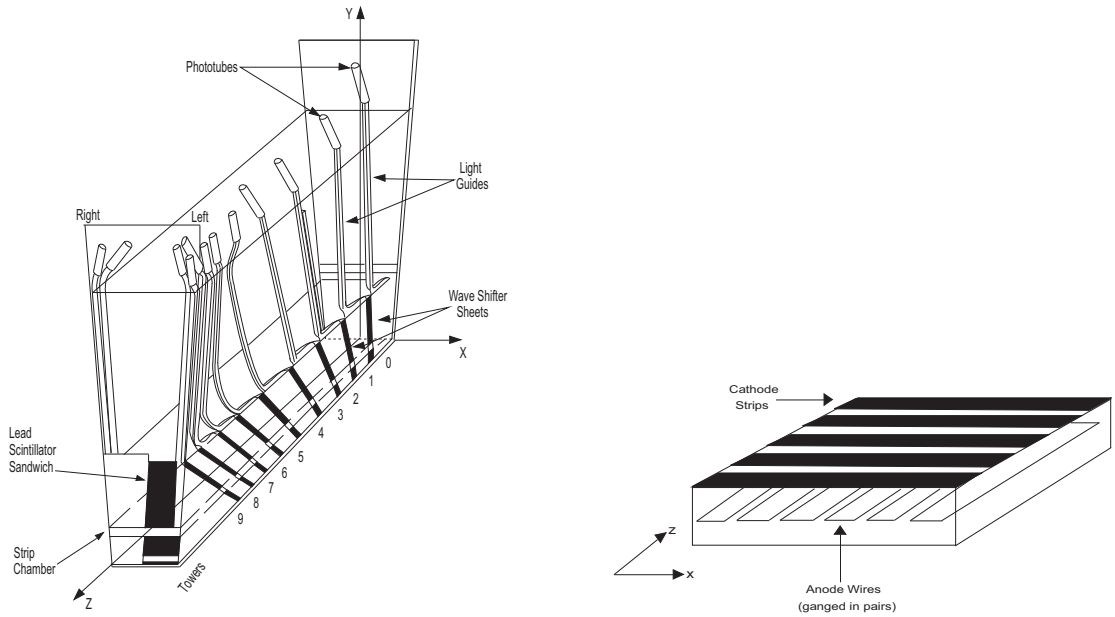

Figure 2.6: The single CEM wedge(left) and the central electromagnetic strip chamber(right).

Central Shower Max Detector (CES)

Proportional chambers (CES) are embedded in the electromagnetic section of the central electromagnetic calorimeter at a depth of 6 radiation lengths (X_0), corresponding to the region of maximum shower intensity for electrons and photons. The position resolution is 0.2 cm at 50 GeV. High-precision position measurements at shower maximum provide track linking ability and transverse shower profiles to improve particle identification. It consists of 48 modules in total, one for each CEM wedge. Each module contains 32 wires parallel to the beam axis and split in the middle for a total of 64 wire readout channels per module, and 128 strips in the direction orthogonal to the wires. Each wedge view is shown in Figure 2.6.

Central Preradiator Detector (CPR)

CPR helps discrimination between electromagnetic and hadronic showers. It uses a proportional chambers to sample the early development of the shower to measure conversions

in the coil, helping to distinguish prompt photons and electrons from photons originating from π^0 decay and electrons from conversions. A prompt photon has a 60% probability of converting, while the conversion probability of at least one photon from $\pi^0 \to \gamma\gamma$ is about 80%.

Central Hadron Calorimeter (CHA)

The Central Hadron Calorimeter is a steel-scintillator sampling calorimeter system [55]. It measures the energy of hadronic showers in the central region. The energy resolution σ_E/E is $50\%/\sqrt{E(\mathrm{GeV})}$. It is located in the central detector outside of CEM, and covers the pseudo-rapidity range of $|\eta| < 0.9$, 32 layers deep. It consists of 384 towers in total, organized into 24 wedges in ϕ and 8 tower groups in η on each side. Each tower is read out by two PMTs.

Plug Electromagnetic Calorimeter (PEM)

Figure 2.7 shows the cross section of plug calorimeter system [56]. The Plug Electromagnetic Calorimeter is a lead-scintillator sampling system. It covers $1.1 < |\eta| < 3.6$. A total thickness is about 21 X_0 (radiation length). The energy resolution is $14.4\%/\sqrt{E(\mathrm{GeV})}$ with a 0.7% constant term.

Plug Shower Max Detector (PES)

The Plug Shower Max Detector is located at the depth of the electromagnetic shower maximum (approximately 6 X_0) and is made of the two layers of 5 mm scintillator strips, with one layer having a 45 ° crossing angle relative to the other. The two layers are called U and V.

Plug Hadron Calorimeter(PHA)

The Plug Hadron Calorimeter is a steel-scintillator sampling system. The energy resolution is $80\%/\sqrt{E(\mathrm{GeV})}$.

2.2.3 Muon Chambers

Muon detector coverage is shown in Figure 2.8. The muon systems consist of four separated subsystems: the central muon chambers(CMU), the central muon upgrade(CMP), the central

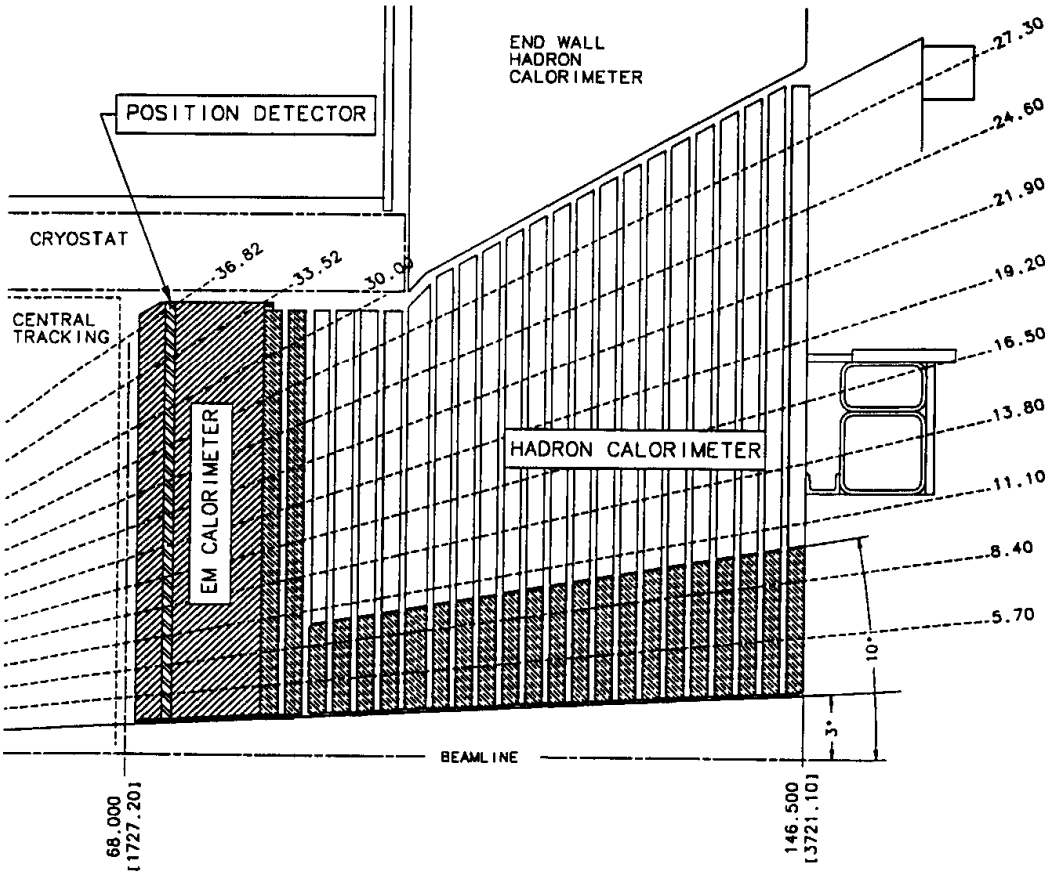

Figure 2.7: The cross section of plug calorimeter system.

muon extension(CMX), the barrel muon detector(BMU). The central muon system is capable of detecting muons with transverse momentum $p_T > 1.4$ GeV/c, through their interaction with the gas and subsequent drift on the produced electrons toward the anode wires [57].

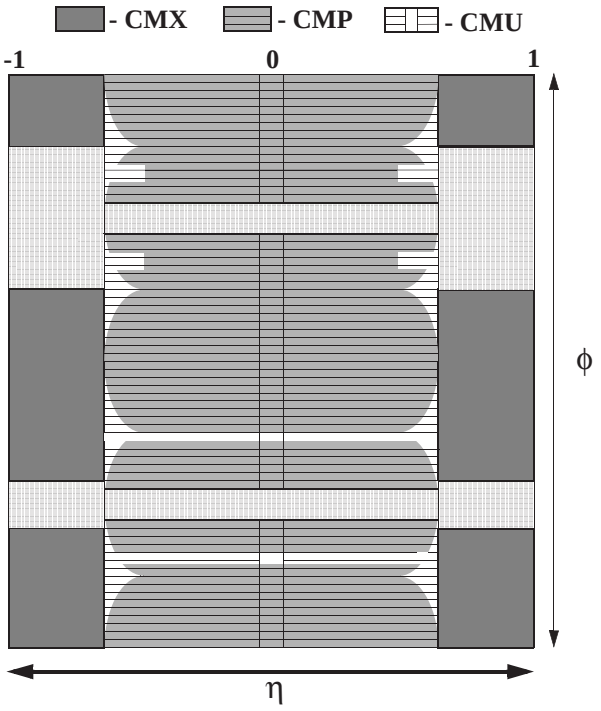

Figure 2.8: Muon Detector Coverage.

Central Muon Detector(CMU)

Outside of Central Hadron Calorimeter, the Central Muon Detector (CMU) is located. It covers $|\eta| < 0.7$ at a radial distance of 3470 mm. The muon chamber operate with argon 50 % and ethane 50 % gas. A stainless steel 50 μm sense wire is located at the center of cell. Figure 2.9 illustrates the layout of the central muon chamber. A single hit TDC is used for measurements in the drift time. An rms resolution of 250 μm in the drift direction and an rms resolution of 1.2 mm along the sense wire are attainable.

Central Muon Upgrade Detector (CMP)

The Central Muon Upgrade Detector (CMP) is located behind an additional 60 cm of steel. It covers $|\eta| < 0.6$. It provides confirmation for CMU tracks but with reduced non-muon (hadronic) background. It consists of 4 layers of single-wire drift cells.

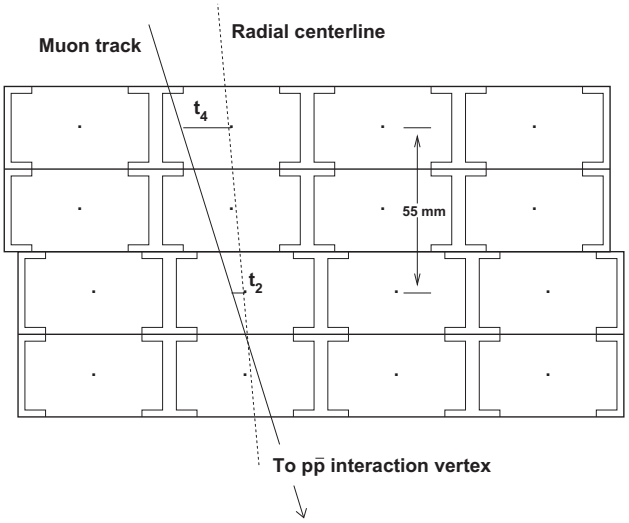

Figure 2.9: Cross section view of muon chamber. Each cell is filled with a gas of argon and ethane mixture. A sense wire is located at the center of cell.

Central Muon Extension Detector (CMX)

The Central Muon Extension (CMX) is located at each end of the central detector. It covers $0.6 < |\eta| < 1.0$.

2.2.4 Luminosity Monitor (CLC)

The Luminosity Monitor consists of long conical gaseous Cherenkov counters that point to the collision region and monitor the average number of inelastic $p\bar{p}$ interactions [58]. The detector consists of two modules which are located in the forward and backward region, which covers $3.7 < |\eta| < 4.7$. The total integrated luminosity ($\mathcal{L}$) is derived from the rate of the inelastic $p\bar{p}$ events measured with CLC, $R_{p\bar{p}}$, the CLC acceptance, ϵ_{CLC}, and the inelastic $p\bar{p}$ cross section at 1.96 TeV, σ_{in}, according to the expression,

$$\mathcal{L} = \frac{R_{p\bar{p}}}{\epsilon_{CLC} \cdot \sigma_{in}}.$$

The CLC acceptance, ϵ_{CLC} is 60.2 ± 2.6 %. The inelastic $p\bar{p}$cross section σ_{in} is 60.7 ± 2.4 mb. The 5.8 % quoted uncertainty is dominated by the uncertainty in the absolute normalization of the CLC acceptance for a single $p\bar{p}$ inelastic collision. Integrated luminosity is shown in Figure 2.10.

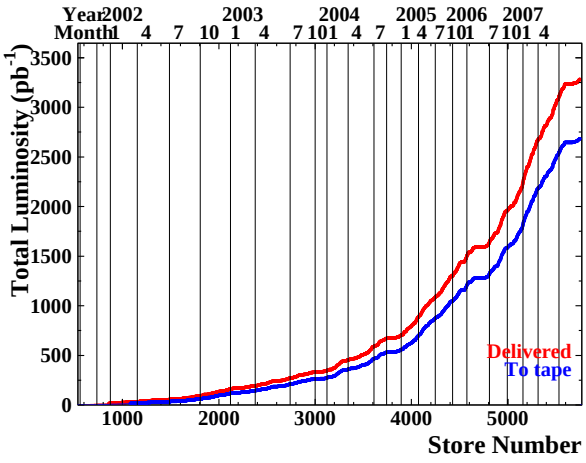

Figure 2.10: Total integrated luminosity recorded by CDF.

2.2.5 Trigger System

In hadron collider experiments, the trigger system plays an important role. The crossing rate of the Tevatron under 36-on-36 bunch operation is 7.6 MHz, corresponding to 396 ns separation. Since the crossing rate is much higher than the rate at which events can be recorded, the trigger system is designed to select the most interesting physics events. The CDF trigger system has a three level architecture. The block diagram of the trigger system is presented in Figure 2.11. Level 1 of the trigger system selects events based on information in the calorimeter, tracking chambers, and muon detector. The maximum Level 1 event accept rate is roughly 20 kHz, corresponding to an available Level 2 processing time of 50 μsec per event. In Level 2, the cluster finder processes the data collected from Level 1 and from the shower max detectors. And also Level 2 provides jet reconstruction and secondary vertex information provided by silicon tracker. These events are transformed to Level 3 processor farm where the events are reconstructed and filtered with $\leq$ 50 Hz.

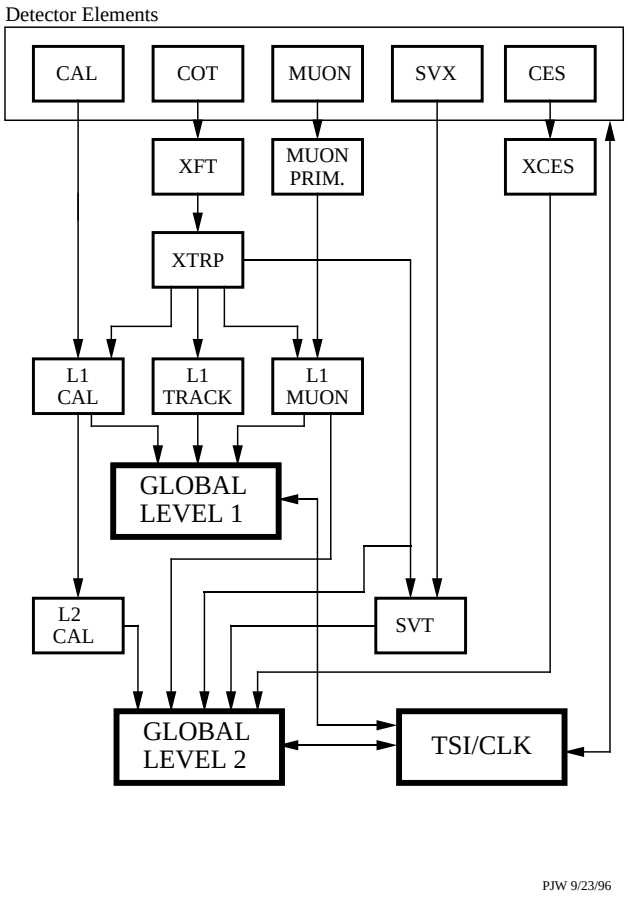

Figure 2.11: Trigger System.

Chapter 3

Inclusive W Production Cross Section

In Run II, with more than one million identified W boson candidates, a high precision measurement of the inclusive production cross section of the W boson can be made with negligible statistical uncertainty. The W production cross section is predicted theoretically with a precision of about 3% and thus measuring this cross section, comparing the electron and muon decay channels, is an ideal test of the selection procedures, the background estimates and the luminosity calculation.

Then this can be used as the basis for more exclusive measurements, such as $W\gamma$ production.

3.1 Introduction

At hadron collider the W boson can most easily be detected through leptonic decay modes. This chapter presents measurement of $\sigma_W \cdot Br(W \to l\nu)$ for $l = e, \mu$ based on the 1 fb^{-1}data collected at CDF from February 2002 to February 2006. The W boson of the unified electroweak theory proposed by Weinberg, Salam, and Glasgow. The W boson was discovered in 1983 using UA1 and UA2 detector. The W are produced via the process shown in Figure 3.1.

Experimentally, the cross section times branching ratio is calculated from

$$\sigma_W \cdot Br(W \to \ell\nu) = \frac{N_{observed} - N_{background}}{\mathcal{A} \cdot \epsilon \cdot \int \mathcal{L} dt}$$

where $N_{observed}$ and $N_{background}$ are the number of $W \to \ell\nu$ candidates observed in the data and the number of expected background events, respectively. $\mathcal{A}$ are the acceptance of the

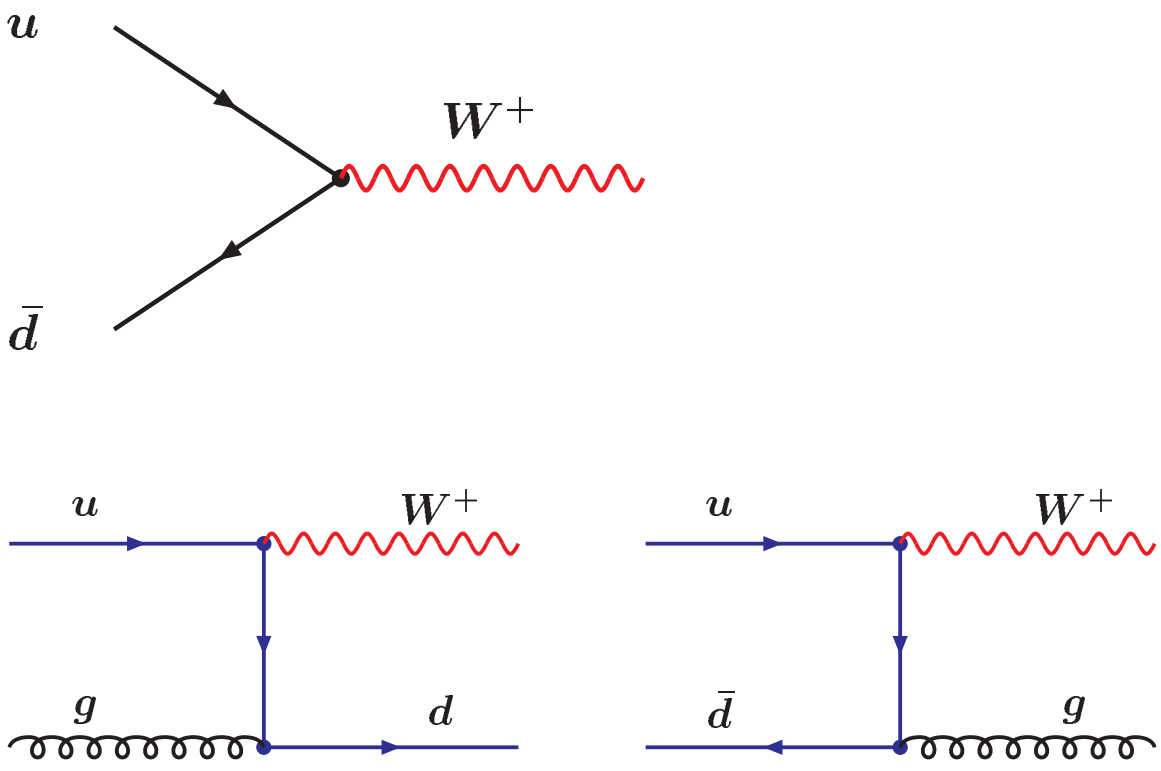

Figure 3.1: Diagrams for production and leptonic decay of W boson. Upper : Leading order. Lower : Next-to-leading order.

W decays ($W \to \ell\nu, \ell = e, \mu$) defined as the fraction of these decays satisfying the geometric constraints of our detector and the kinematic constraints of our selection criteria, ϵ are the combined efficiencies for the identifying W falling within our acceptance, and $\int \mathcal{L}dt$ is the integrated luminosity. We search for W bosons decaying into highly energetic charged lepton ($\ell = e, \mu$) and a neutrino, which is identified via large missing transverse energy, $\not\!\!E_T$ defined in the following subsection.

3.2 Data and Monte Carlo Samples

The datasets used are high p_T leptons data for the this analysis. The $W \to \ell\nu$ candidates are collected with well-defined trigger requirements at each of the three levels within the CDF trigger architecture. The specific trigger requirements associated with the datasets used to make our measurements are summarized here.

3.2.1 Track Reconstruction

The tracking system of the CDF detector is briefly introduced in the previous section. It detects and reconstructs trajectories of charged particles. The track quality requirements are common to electron and muon selection. Two tracking algorithms are implemented at CDF. In the central region within the $|\eta| < 1$ coverage of the COT, a more robust algorithm is used called "Outside-In". In the plug region, the tracking based on the "Silicon Stand-Alone" tracking. The track reconstruction starts in the COT. The algorithm reconstructs track segments with four or more hits in each super layer. The COT tracking efficiency is nearly 100 % for isolated tracks with $p_T > 5$ GeV/c. The "Outside-In" tracking extends the COT tracks into the silicon. It attaches silicon hits to COT tracks. Then the track is extrapolated until the track reaches to the inner most silicon wafer. At the end, the track combination with the highest number of hits and lowest χ^2/dof is kept. The "Silicon Stand-Alone" method reconstructs tracks from the remaining hits in the silicon which are not matching to the COT tracks with the highest number of hits and lowest χ^2/dof.

3.2.2 Central Electron Trigger

`ELECTRON_CENTRAL_18` Trigger

- Level 1 : At least one tower which has $E_T > 8$ GeV and $E_{\rm HAD}/E_{\rm EM} < 0.125$ associated with at least one track with $p_T > 8.34$ GeV/c.
- Level 2 : In clustering algorithm, the adjacent towers with $E_T > 7.5$ GeV are added to the seed tower found in Level 1. The total E_T of cluster > 16 GeV and $E_{\rm HAD}/E_{\rm EM} < 0.125$ are required.
- Level 3 : By reconstruction algorithm, electromagnetic cluster which has $E_T > 18$ GeV, $E_{\rm HAD}/E_{\rm EM} < 0.125$, $L_{shr} < 0.4$, $\Delta z < 8$ cm and $p_T > 9$ GeV/c must be found.

3.2.3 Muon Trigger

`MUON_CMUP18` trigger

- Level 1 : One or more hits in CMU detector match to track with $p_T > 4.09$ GeV/c. A spacial coincidences of CMU and CMP hits are required.
- Level 2 : We require at least one COT track with $p_T > 14.77$ GeV/c.
- Level 3 : Based on reconstruction algorithm, muons with $p_T > 18$ GeV/c, $\Delta x_{CMU} < 10$ cm, and $\Delta x_{CMP} < 20$ cm are selected.

`MUON_CMX18` trigger

- Level 1 : One or more hits in CMX detector match to track with $p_T > 8.34$ GeV/c.
- Level 2 : We require at least one COT track with $p_T > 14.77$ GeV/c.
- Level 3 : Based on reconstruction algorithm, muons with $p_T > 18$ GeV/c, $\Delta x_{CMX} < 10$ cm are selected.

3.2.4 Plug Electron Trigger

`PLUG_ELECTRON_20` trigger

- Level 1 : At least one tower which has $E_T > 8$ GeV and $E_{\rm HAD}/E_{\rm EM} < 0.125$.

- Level 2 : In clustering algorithm, the adjacent towers with $E_T > 7.5$ GeV are added to the seed tower found in Level 1. The total E_T of cluster > 20 GeV and $E_{\rm HAD}/E_{\rm EM} < 0.125$ are required. Candidates in $1.1 < |\eta| < 3.6$ are selected.

- Level 3 : By reconstruction algorithm, electromagnetic cluster which has $E_T > 20$ GeV, $E_{\rm HAD}/E_{\rm EM} < 0.125$ must be found. Number of events are prescaled to 25.

`MET_PEM` trigger

In addition to `PLUG_ELECTRON_20` trigger, $\not\!\!E_T > 15$ GeV is required in Level 1 and Level 3 system.

3.2.5 Luminosity

Requiring a good detector status, we obtain luminosities of 1101.665 pb^{-1} for electron, 1019.665 pb^{-1} for plug electron, and 1030.94 pb^{-1} for muon. The data called 0d, from 7th Dec 2004 to 4th Sep 2005 (run190697-run203799) called 0h, and from 5th Sep 2005 to 22nd Feb 2006 (run203819 to run212133) called 0i.

3.3 Event Selection

3.3.1 Central Electron Selection

The events are required to be triggered by the `ELECTRON_CENTRAL_18` triggers.

- E_T : Transverse energy given by $E \times sin\theta$. Total Energy E is calculated by $E_{\rm EM}$ (Energy deposited in electromagnetic calorimeter) + $E_{\rm HAD}$ (Energy deposited in hadronic calorimeter).

- η : We required η cut to ensure instrumented region of detector.

- p_T : Transverse momentum. When the momentum of a charged particle is too low, the reconstruction of its track becomes imprecise. This is due to the small radius of curvature. Therefore a cut on the measured momentum is applied; $p_T < 10$ GeV/c.

- $E_{\rm HAD}/E_{\rm EM}$: Ratio of $E_{\rm HAD}$ and $E_{\rm EM}$. An energetic electron deposit most of energy in electromagnetic calorimeter with small leakage in hadronic calorimeter. We require $E_{\rm HAD}/E_{\rm EM} < 0.055 + 0.00045 \cdot E$ GeV. The linear term in our selection criteria accounts

for the increased shower leakage of higher-energy electrons into hadronic calorimeter sections.

- Isolation : For jet suppression, we build a cone of $\Delta R = \sqrt{(\Delta\phi)^2 + (\Delta\eta)^2} < 0.4$ around the lepton central position, and sum E_T in the cone excluding lepton's energy. We required that the calorimeter energy in a cone around the lepton excluding the energy associated with the lepton be less than 10 % the energy of the lepton.

- z_0 : The z position on the beam line extrapolated from track. To restrict to a region of high track reconstruction efficiency, we require the z coordinate of the lepton track intersection with the beam axis in the $r - z$ plane, z_0, be within 60 cm of the center of the detector.

- N_{Ax}, N_{St} : The number of axial(stereo) superlayers with more than five hits are required to ensure a well measured COT track.

- χ^2_{strip} : For the separation of electromagnetic shower from jets($\pi^0 \rightarrow \gamma\gamma$), the χ^2 comparison between the CES shower profile and the electron profile from testbeam.

- L_{shr} : The lateral shower sharing variable, obtained from measured energy and expected energy from testbeam.

$$L_{shr} = 0.14 \frac{\sum_i (E_i^m - E_i^{exp})}{\sqrt{(0.14\sqrt{E_{\rm EM}})^2 + \sum_i (\Delta E_i^{exp})^2}}$$

  - E_i^m : Measured energy deposit in i th tower.
  - E_i^{exp} : Expected energy deposit from testbeam data in i th tower.
  - $E_{\rm EM}$: The total electromagnetic energy.
  - ΔE_i^{exp} : An estimate of the uncertainty of E_i^{exp}.

- Δx, Δz : The distance between CES shower measured by CES detector and track position extrapolated from COT detector in coordinate x(z).

- E/p : We cut on the ratio of the electromagnetic cluster transverse energy to the COT track transverse momentum, E/p. This ratio is nominally expected to be unity, but in cases where the electron radiates a photon in the material of the inner tracking volume, the measured momentum of the COT track can be less than the measured

energy of the corresponding cluster in the calorimeter. In cases where the electron is highly energetic, the photon and electron will be nearly collinear and are likely to end up in the same calorimeter tower. The measured COT track momentum will, however, correspond to the momentum of the electron after emitting the photon and thus be smaller than the original electron momentum. We require $E/p < 2$ which is efficient for the majority of electrons which emit a bremsstrahlung photon. Since this cut becomes unreliable for very large values of track p_T, we do not apply it to electron clusters with $E_T > 50$ GeV.

The central electron identification cuts are detailed in Table4.4. The distributions of the

Variable	**Central Electron**
E_T	> 25 GeV
$\|\eta\|$	< 1.1
p_T	> 10 GeV/c
$E_{\rm HAD}/E_{\rm EM}$	$< 0.055 + 0.00045 \times E$ (GeV)
Isolation	$< 0.1 \times E_T$ GeV
$\|z_0\|$	< 60 cm
N_{Ax}	> 2
N_{St}	> 1
χ^2_{strip}	< 10
L_{shr}	< 0.2
Δz	< 3 cm
$q \times \Delta x$	$-3 < q \times \Delta x < 1.5$ cm
E/p	< 2 or $p_T > 50$ GeV

Table 3.1: Central Electron ID variables and cut values.

central electron identification variables are shown in Figures 3.2 and 3.3. The number of events surviving each step in the $W \rightarrow$ central $e\nu$ selection is given in Table 3.2.

3.3.2 Plug Electron Selection

The events are required to be triggered by the `MET_PEM` triggers.

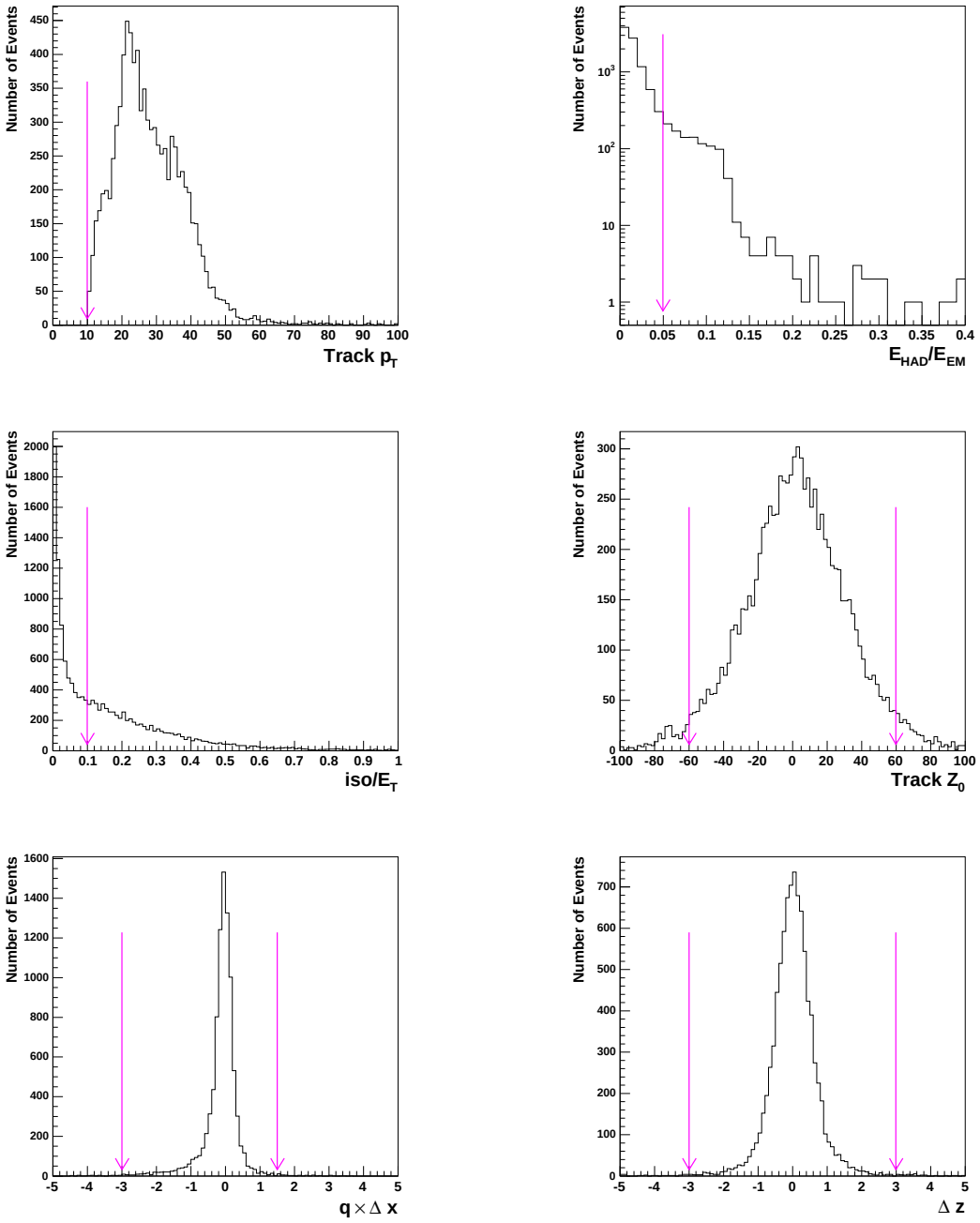

Figure 3.2: Central electron distributions of Track p_T, $E_{\rm HAD}/E_{\rm EM}$, iso/E_T, Track Z_0, q ×Δ x, and Δ z. The arrows indicate the locations of selection cuts applied on these variables.

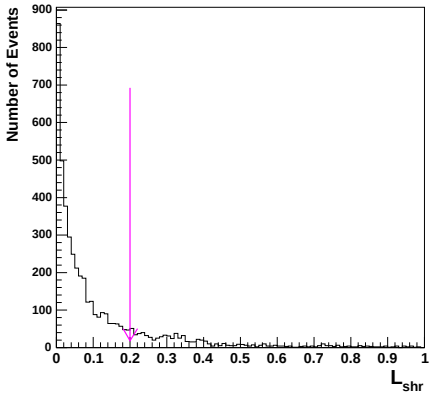

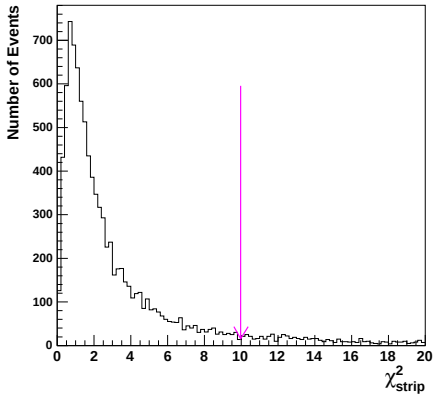

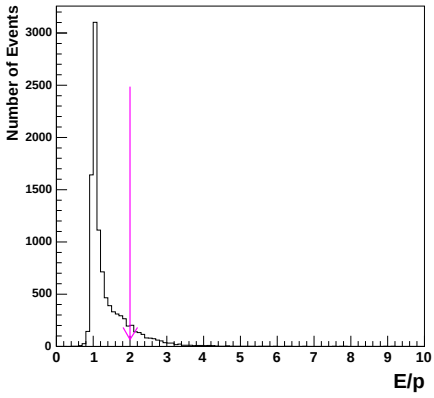

Figure 3.3: Central electron distributions of L_{shr}, χ^2_{strip}, and E/p. The arrows indicate the locations of selection cuts applied on these variables.

Selection Criteria	Central Electron (Events)
Total Processed Events	58863713
Good Run List	50622350
Electron ID	2484711
$\not\!\!E_T$ cut	618629
M_T cut	615124

Table 3.2: Number of central electron events surviving each step in the W selection.

- $PEM\eta$: The detector η best matching to PEM cluster.
- PEM3 $\times$ 3FitTower : The number of PEM calorimeter towers used in PEM cluster fit (The energy distribution in 3×3 blocks of PEM calorimeter towers around the seed tower fitted to the expected distribution from testbeam data).
- χ^2_{PEM} : We compared the distributions of tower energies in a 3×3 array around the seed tower to distributions from electron test-beam data, forming the variable χ^2_{PEM}
- PES 5x9 UV : The ratio of energy in central five strips and energy in whole nine strips for discrimination prompt photon and meson decay (ex. $\pi^0 \rightarrow \gamma\gamma$) in U-strips (V-strips).
- ΔR_{PESPEM} : The distance between the shower position measured by PES detector and the position by PEM detector.
- PHX Track Matching : The existence of a track pointing to PEM cluster.
- $N_{SiliconHits}$: Number of hits in silicon detector to ensure track.

The plug electron identification cuts are detailed in Table3.3. The distributions of the plug electron identification variables are shown in Figure 3.4. The number of events surviving each step in the $W \rightarrow$ plug $e\nu$ selection is given in Table 3.4.

3.3.3 Muon Selection

The events are required to be triggered by the `MUON_CMUP18` or the `MUON_CMX18` triggers.

Variable	**Plug Electron**
E_T	≥ 25 GeV
PES $\lvert\eta\rvert$	$1.2 < \eta < 2.0$
$E_{\mathrm{HAD}}/E_{\mathrm{EM}}$	< 0.05
Isolation Energy	≤ 4 GeV
$\lvert z_0\rvert$	< 60 cm
PEM3 $\times$ 3FitTower	$\neq 0$
χ^2_{PEM}	< 10
PES 5×9 UV	> 0.65
ΔR_{PESPEM}	≤ 3 cm
PHX Track Matching	true
$N_{SiliconHits}$	≤ 3

Table 3.3: Plug Electron ID variables and cut values.

Selection Criteria	**Plug Electron (Events)**
Total Processed Events	51181163
Good Run List	39340739
Electron ID	611726
$\not\!\!E_T$ cut	304705
M_T cut	302196

Table 3.4: Number of plug electron events surviving each step in the W selection.

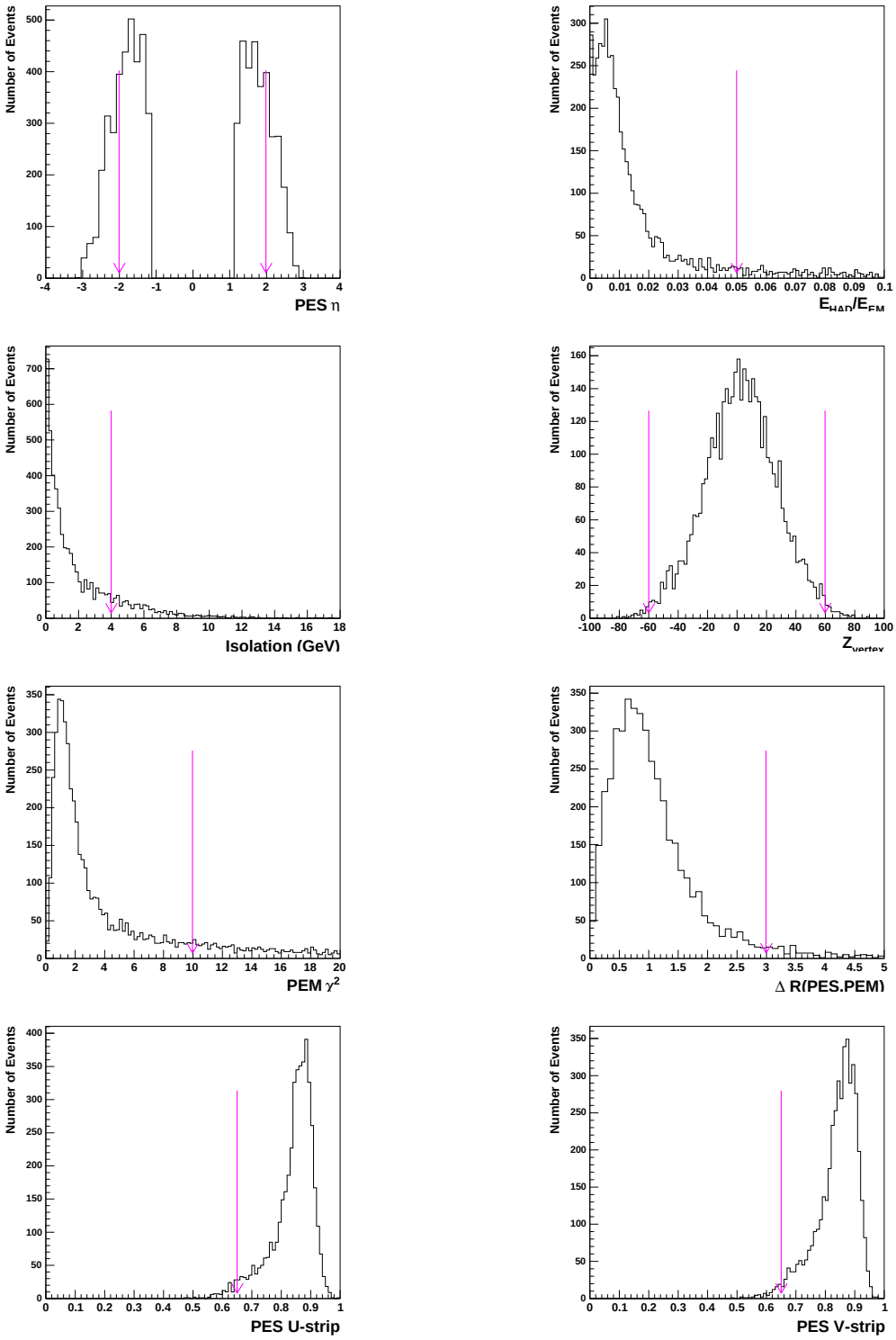

Figure 3.4: Plug electron distributions of PESη, $E_{\rm HAD}/E_{\rm EM}$, Isolation, Z_{vertex}, PEMχ^2, $\Delta R(PES, PEM)$, PES energy ratio in U-strip, and PES energy ratio in V-strip. The arrows indicate the locations of selection cuts applied on these variables.

- d_0 : The impact parameter of muon track to ensure the tracks originated from the interaction point, reducing cosmic ray contamination. $|d_0| < 0.02$ with SVX hits, $|d_0| < 0.2$ without SVX hits. Cosmic muons and muons produces in π/K decays are less likely to point back to the event vertex and therefore will typically have larger measured impact parameters.

- χ^2_{COT} : The χ^2 of COT track fitting to reduce $\pi^{\pm}$, $K^{\pm}$ contamination. We make a requirement on the quality of the final COT track fit for muon candidates. The track fit for muon backgrounds not originating from the event vertex will typically be worse.

- ρ_{COT} : Cut on COT exit radius ρ_{COT} to ensure that each reconstructed muon in sample pass through all eight COT super-layers having high efficiency for triggering the event.

$$\rho_{COT} = \frac{\eta}{|\eta|}\frac{Z_{COT} - Z_0}{tan(\lambda)},$$

  where $\lambda = \pi/2 - \theta$ and $\theta = 2 \cdot tan^{-1}(e^{\eta})$

- Δx : The distance between the position of hit on (CMU/CMP/CMX) detector and the extrapolated track from COT.

- Cosmic ray rejection :

  Energetic cosmic ray muons traverse the detector at a significant rate, can mimic the $W \rightarrow \mu\nu$ events. A cosmic ray muon passing through the detector is typically reconstructed as a pair of incoming and outcoming legs relative to the beam line of detector. We removed cosmic ray events from $W \rightarrow \mu\nu$ using the timing information.

- $Z \rightarrow \mu\mu$ veto :

  A background to $W \rightarrow \mu\nu$ is the $Z \rightarrow \mu\mu$ channel, when one of the leptons falls into an uninstrumented region of the detector, creating false $\not\!\!E_T$. We required no other track which passed

  - $p_T > 10$ GeV/c
  - Number of hits in COT (Axial)$\geq$ 3, Number of hits in COT(Stereo) $\geq$ 2
  - $|d_0| < 0.5$ cm
  - $|Z_0| < 60$ cm
  - $iso/E_T < 0.1$

The muon identification cuts are detailed in Table3.5. The distributions of the muon iden-

Variable	**Muon**
p_T	> 20 GeV/c
$E_{\rm EM}$	< 2 GeV + $\max(0, 0.0115 * (p - 100))$
$E_{\rm HAD}$	< 6 GeV + $\max(0, 0.028 * (p - 100))$
Isolation	$< 0.1 \times p_T$ GeV/c
$\lvert z_0 \rvert$	< 60 cm
$\lvert d_0 \rvert$	COT: < 0.2 cm, SVX: < 0.02 cm
N_{Ax}	> 2
N_{St}	> 1
ρ_{COT}	> 140 cm
χ^2_{COT}	< 2.75 (for the first 361pb^{-1} data), < 2.3 (for the rest of data)
Δx	< 7 cm (CMU), < 5 cm (CMP), < 6 cm (CMX)

Table 3.5: Muon ID variables and cut values for CMUP and CMX muons.

tification variables are shown in Figure 3.5 and Figure 3.6. The number of CMUP, CMX events surviving each step in the W selection is given in Table 3.6.

Selection Criteria	**CMUP (Events)**	**CMX (Events)**
Total Processed Events	13306740	13306740
Good Run List	12507948	12193775
Muon ID	679522	360159
$Z \rightarrow \mu\mu$ veto	636821	340294
iso/E_T cut	423093	222729
$\not\!\!E_T$ cut	342165	179153
M_T cut	339440	177826

Table 3.6: Number of CMUP, CMX events surviving each step in the W selection.

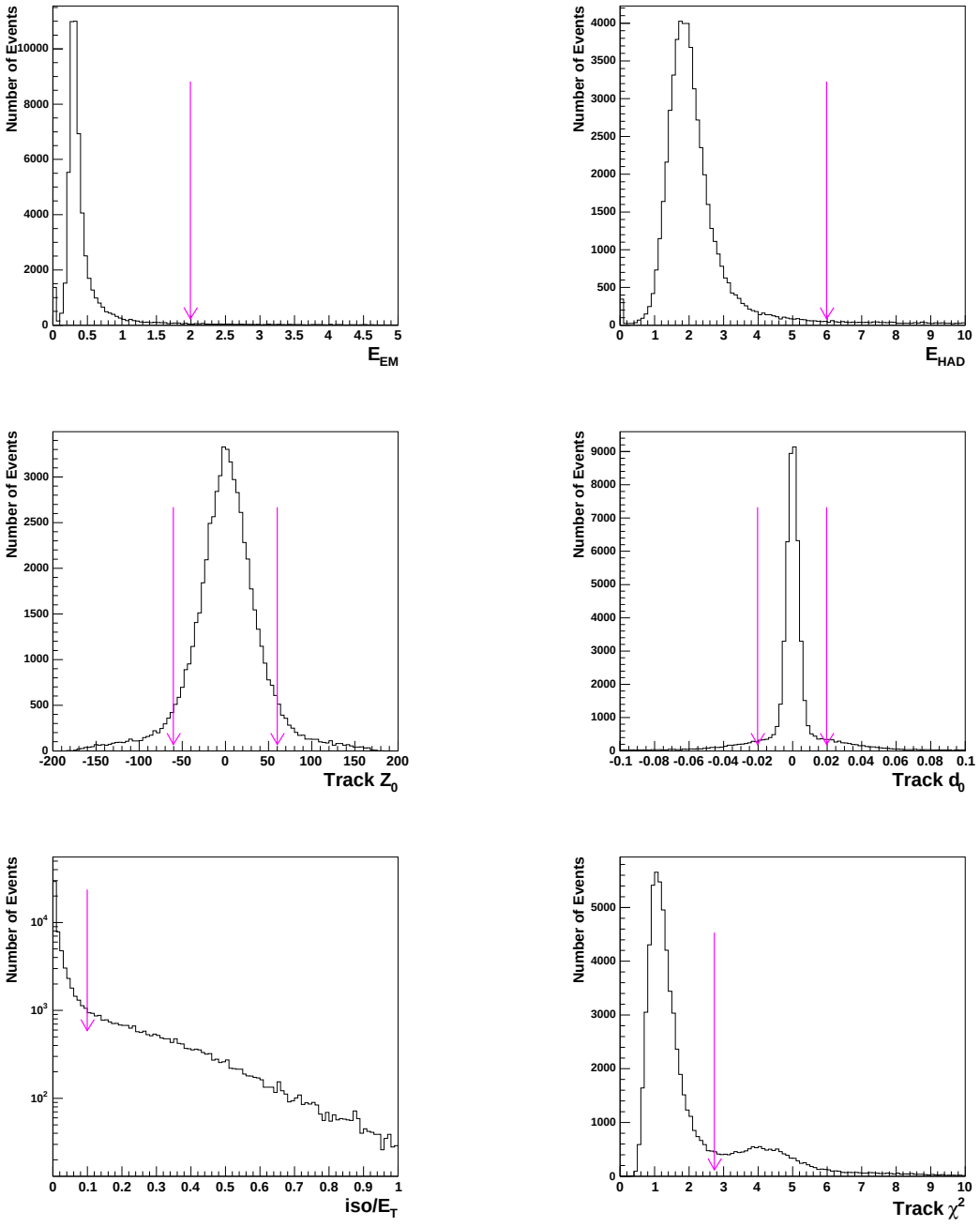

Figure 3.5: Muon distributions of E_{EM}, E_{HAD}, Track Z_0, Track d_0, iso/E_T, Track COT χ^2. The arrows indicate the locations of selection cuts applied on these variables.

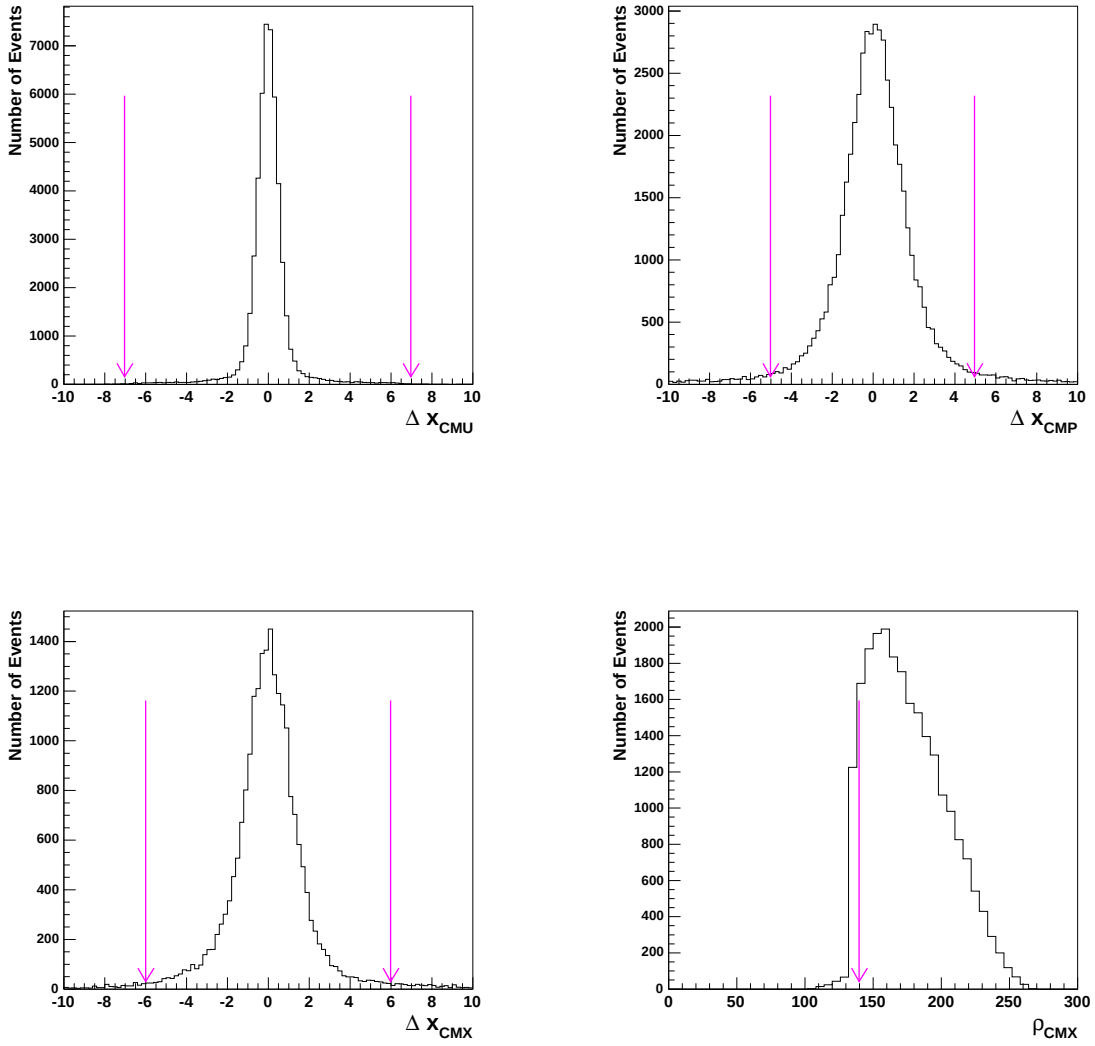

Figure 3.6: Muon distributions of Δx_{CMU}, Δx_{CMP}, Δx_{CMX}, Track ρ_{COT}. The arrows indicate the locations of selection cuts applied on these variables.

3.3.4 Missing Transverse Energy Calculation

The missing transverse energy $\not\!\!E_T$ is calculated from :

$$\vec{\not\!\!E}_T = -\sum_i \vec{E}_T^i,$$

where $\vec{E_T}$ is a vector whose magnitude is the transverse energy in a calorimeter tower and projected to $r-\phi$ plane. The sum involves all towers with total energy (hadronic and electromagnetic) above 0.1 GeV within the region $|\eta| < 3.6$, corresponding to the all central and plug calorimeter. $\not\!\!E_T$ in the calorimeter is calculated assuming that the interaction point is located at $z = 0.0$ cm. Therefore $\not\!\!E_T$ is corrected by the vertex position using the Z_0 of charged lepton track, subtracted lepton energy deposit from $\sum_i E_T^i$. x and y components of $\not\!\!E_T$ are corrected for the energy carried away by muon.

$$\not\!\!E_T^x = |\not\!\!E_T| \cdot \cos\phi_{MET}$$
$$\not\!\!E_T^y = |\not\!\!E_T| \cdot \sin\phi_{MET}$$

$$\not\!\!E_T^x(corrected) = \not\!\!E_T^x - (p_T^\mu - E_T^{EM\ \mu} - E_T^{HAD\ \mu}) \cdot \cos\phi_\mu$$
$$\not\!\!E_T^y(corrected) = \not\!\!E_T^y - (p_T^\mu - E_T^{EM\ \mu} - E_T^{HAD\ \mu}) \cdot \sin\phi_\mu$$

where $p_T^\mu E_T^{EM\ \mu} E_T^{HAD\ \mu}$ are the transverse momentum, the transverse electromagnetic energy, the transverse hadronic energy of muon. Here, $\not\!\!E_T$ is calculated with respect to the highest $\sum p_T$ Z-vertex if $|Z_v - Z_0| < 5$ cm, and with respect to the lepton Z_0 otherwise.

The transverse mass M_T of the W boson is calculated by the lepton p_T, $\not\!\!E_T$, and the azimuthal angle between the lepton momentum and the missing transverse momentum vector ($\Delta\phi = \phi_{lepton} - \phi_{MET}$):

$$M_T = \sqrt{2 \cdot p_T \cdot \not\!\!E_T \cdot (1 - \cos\Delta\phi)}.$$

since the longitudinal component of the neutrino momentum can not be measured.

3.3.5 Selection of $W \to \ell\nu$ Candidates

In addition to the lepton selection, we require $\not\!\!E_T > 25$ GeV for the electron and $\not\!\!E_T > 20$ GeV for the muon analysis. Also we require the transverse mass to be greater than 30 GeV/c^2 and less than 120 GeV/c^2

Using these selections we find 616,943 $W \rightarrow$ central $e\nu$ candidates, 302,196 $W \rightarrow$ plug $e\nu$ candidates, and 520,818 $W \rightarrow \mu\nu$ candidates. The acceptance is calculated using PYTHIA Monte Carlo simulation.

3.4 Backgrounds

Other physics processes can produce events that mimic the signature of $W \rightarrow \ell\nu$ in our detector. Some processes have similar final state event topologies to those of our signal samples and others can fake similar topologies if a non lepton object within the event is misidentified as an electron or muon. We separate the background sources into two categories: events from other electroweak process and events in which hadronic jets fake leptons. The following background sources have been considered:

- Electroweak backgrounds from $W \rightarrow \tau\nu$ and Drell-Yan production is evaluated using the corresponding Monte Carlo samples. For Drell-Yan production the decays to all three lepton flavors are considered. $Z \rightarrow \ell\ell$ events mimic the signature of $W \rightarrow \ell\nu$ events in cases where one of the two leptons passes through an uninstrumented region of the detector creating an imbalance in the observed event E_T. The $W \rightarrow \ell\nu$ signature can also be reproduced by $W \rightarrow \tau\nu$ events in which the τ lepton subsequently decays into an electron or muon.

- QCD jet background is determined from the data. This background arises from jet production where the jet is misidentified as lepton, and $\not\!\!E_T$ is mismeasured such that the event enters the selection. Real leptons are produced both in the semileptonic decay of hadrons and by photon conversions in the detector material. Some events also contain other particles in hadronic jets which are misidentified and reconstructed as leptons. Typically, these types of events will not be accepted into our W candidate samples because we require large event $\not\!\!E_T$. In a small fraction of these events, however, a significant energy mismeasument does reproduce the $\not\!\!E_T$ signature of our samples.

3.4.1 QCD Backgrounds in Central Electron or Muon Channel

This background is estimated using the "iso vs. met" method [63]. In order to estimate this background contribution, we release the section criteria on isolation and $\not\!\!E_T$ and use events

with low isolation and low $\not\!\!E_T$ as a model of background in W signal region (low isolation and high $\not\!\!E_T$). The contributions in the low and high $\not\!\!E_T$ regions are normalized to the number of events in those regions with high isolation, based on the assumption that there is no correlation between isolation and $\not\!\!E_T$ in the QCD background. The plane is divided into four regions (A, B, C and D) as shown in Figure 3.7. The QCD background in the signal region D is given by

$$N_{QCD} = A \cdot C/B.$$

We subtract the electroweak backgrounds from each of the regions. The numbers of events are given in Table 3.7. Figure 3.7 shows the isolation fraction variable plotted against event $\not\!\!E_T$ in data (no cuts on electron isolation fraction or event $\not\!\!E_T$).

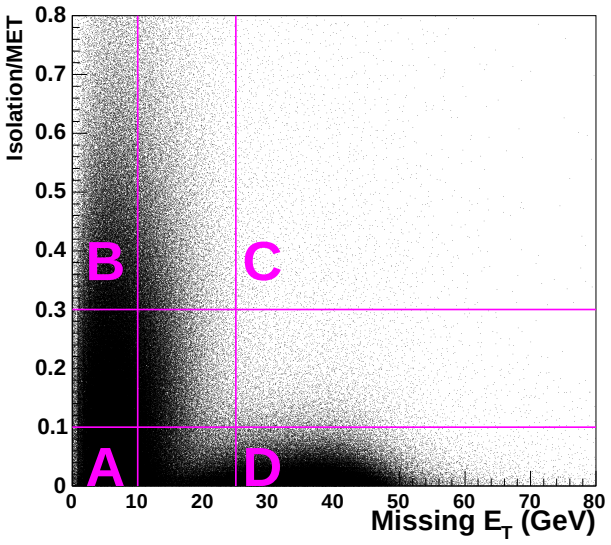

Figure 3.7: Electron iso/E_T vs $\not\!\!E_T$ in Data.

3.4.2 W in Plug Electron Channel QCD Backgrounds

Historically, CDF has adopted the "iso/E_T vs. $\not\!\!E_T$" for non-W background estimation, based on the assumption that there is no correlation between iso/E_T and $\not\!\!E_T$. Since `MET_PEM` trigger is biased by $\not\!\!E_T$, this background fraction is obtained from the Isolation fitting method. We estimated QCD background by fitting the isolation energy distribution with signal and background fraction template to the data through a standard likelihood fit using Poisson statistics.

Central Electron	Region A	Region B	Region C
Data	513770	310053	8449
MC $W \rightarrow e\nu$	5111	20	3036
MC $Z \rightarrow ee$	85258	313	48
MC $W \rightarrow \tau\nu$	1189	4	118
CMUP	Region A	Region B	Region C
Data	41943	67425	6716
MC $W \rightarrow \mu\nu$	2471	10	1480
MC $Z \rightarrow \mu\mu$	1134	4	127
MC $W \rightarrow \tau\nu$	498	1	49
CMX	Region A	Region B	Region C
Data	23128	36874	3889
MC $W \rightarrow \mu\nu$	1132	4	796
MC $Z \rightarrow \mu\mu$	587	1	61
MC $W \rightarrow \tau\nu$	271	1	21

Table 3.7: Number of central electron, CMUP muon, and CMX muon events in the four regions of the iso vs $\not\!\!E_T$ plane for data, and the electroweak Monte Carlo samples.

Signal Template Selection

Signal template is made from data with PLUG_ELECTRON_20 trigger requiring $Z \rightarrow ee$ selection. Central(tighter leg)-plug(fitting leg) or plug(tighter leg)-plug(fitting leg) are selected. Central electron tighter leg passed standard central electron ID in Table 4.4 and $iso/E_T < 0.05$ and $L_{shr} < 0.1$. Plug electron tighter leg passed standard plug electron ID (written in Table 3.3) and $iso/E_T < 0.05$. Plug electron fitting leg passed standard plug electron ID (written in Table 3.3) except isolation cut. We also required invariant mass cut, 81 GeV/c^2 $< M_{ee} <$ 101 GeV/c^2. Figure 3.8 left plot shows Isolation does not depend on E_T. We applied signal template from $Z \rightarrow ee$ data for all E_T range. Figure 3.8 right plot is $W \rightarrow e\nu$ MC Isolation v.s. $\not\!\!E_T$ in different E_T range. It shows 25 GeV $< \not\!\!E_T <$ 35 GeV region is flat and there is a behavior in 35 GeV $< \not\!\!E_T$ region, therefore we divided signal template into two sections, one is 25 GeV $< \not\!\!E_T <$ 35GeV, the other is $\not\!\!E_T >$ 35 GeV.

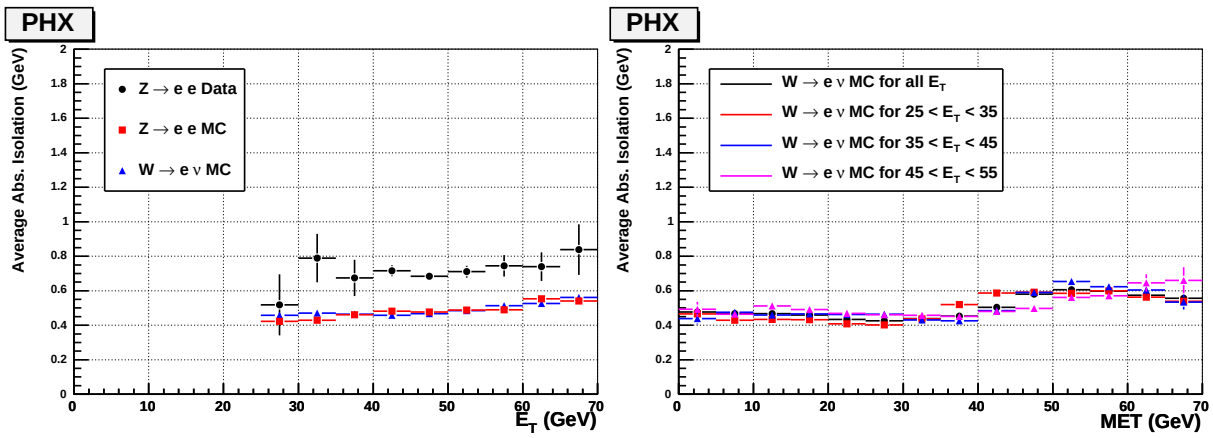

Figure 3.8: Left : isolation energy as a function of plug electron E_T. Right : $W \rightarrow \ell\nu$ Monte Carlo isolation energy as a function of $\not\!\!E_T$ in different plug electron E_T regions.

Background Template Selection

Background template is made from di-jet event in high p_T plug electron data. One anti-electron defined in Table 4.5 left column + one jet events are selected. Background template selection is detailed in Table 4.5. Figure 3.9(left) shows Isolation does not depend on E_T.

Figure 3.9(right) shows there is no significant difference between $0 < \not\!\!E_T < 10$ and $0 < \not\!\!E_T < 20$ in Isolation distributions. Therefore We applied background template for all E_T range and also all $\not\!\!E_T$ range.

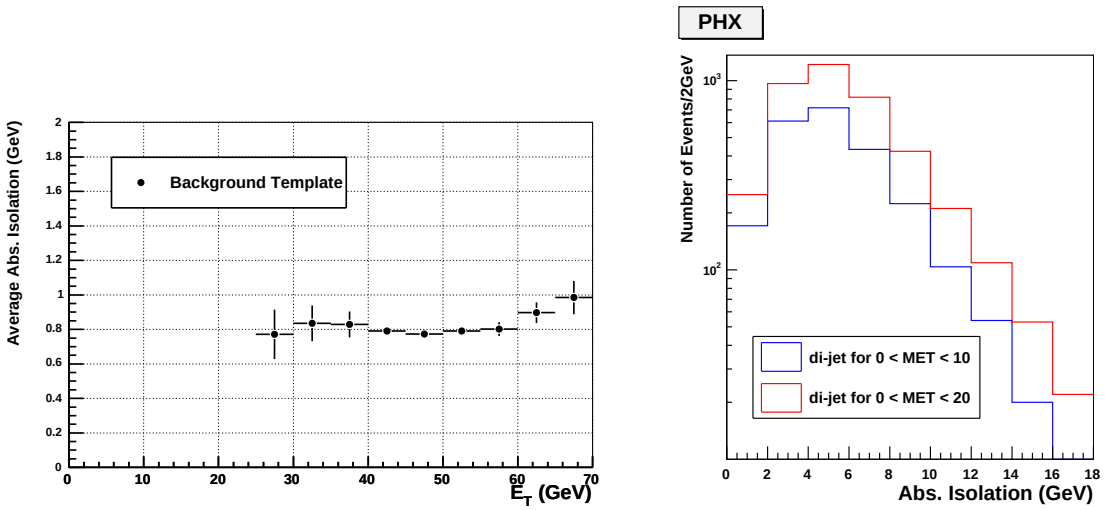

Figure 3.9: Left : Isolation energy of background template as a function of E_T. Right : Isolation energy of background template in different $\not\!\!E_T$ range.

3.4.3 QCD background fraction

Figure 3.11 shows the isolation energy fitting with signal template and background template. Table 3.10 details QCD background fraction in W candidates estimated by isolation distribution fitted with signal template from $Z \rightarrow ee$ data and background template obtained from di-jet events in high p_T plug electron data.

For cross check, using the same procedure we estimated QCD background in central region. The QCD fraction estimated by "iso v.s $\not\!\!E_T$" method is 0.959 ± 0.023. It is consistent with each other between two estimations within error.

3.5 Efficiencies and Scale Factors

3.5.1 Z vertex cut Efficiency

The Z vertex cut efficiency, ϵ_{Z_0} is measured in data. Only events with $|Z_0| < 60$ cm are

Variable	**Anti-Electron**	**Variable**	**JET**
E_T	≥ 25 GeV	E_T	≥ 25 GeV
$\|PES2DEta\|$	$1.2 < \eta < 2.0$	region	central or plug
HAD/EM	≥ 0.05	HAD/EM	≥ 0.05
$\|z_0\|$	< 60 cm	Cone size	0.4
PEM3x3FitTower	$\neq 1$	$\|\Delta\phi_{jet,jet}\|$	if $15< P_T <25 \leq 2.8$, else ≤ 2.6
χ^2_{PEM}	< 10	$N_{EMObject}$	=1
PES 5x9 UV	> 0.65	N_{Jet}	=1
ΔR_{PESPEM}	≤ 3 cm	$\not\!\!E_T$	≤ 10 GeV
PHX Track Matching	true		
$N_{SiliconHits}$	≤ 3		

Table 3.8: Di-jet Selection for background template.

Template $\not\!\!E_T$ region	$25 < \not\!\!E_T < 35$	$35 < \not\!\!E_T$	Total
Number of QCD	1015.1	188.3	1203.4
Number of Data	135900	170186	306086
QCD Fraction (%)	0.747±0.032	0.111± 0.011	0.393 ±0.034

Table 3.9: QCD background fraction in W candidates estimated by isolation distribution fitting in plug region.

Template $\not\!\!E_T$ region	$25 < \not\!\!E_T < 35$	$35 < \not\!\!E_T$	Total
Number of QCD	1293.6	948.1	2241.70
Number of Data	89478	124201	213679
QCD Fraction (%)	1.446±0.056	0.763± 0.035	1.049 ±0.021

Table 3.10: QCD background fraction in W candidates estimated by isolation distribution fitting in central region.

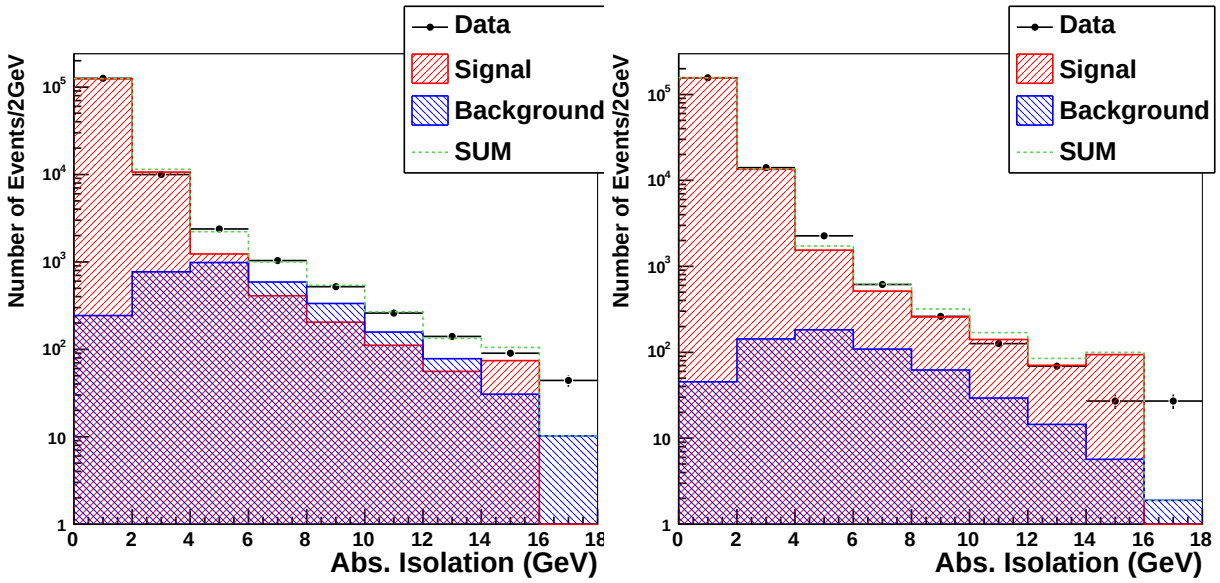

Figure 3.10: Plug Electron Isolation Energy distributions in $25 < \not\!\!E_T < 35$ (left) and in $35 < \not\!\!E_T$ (right).

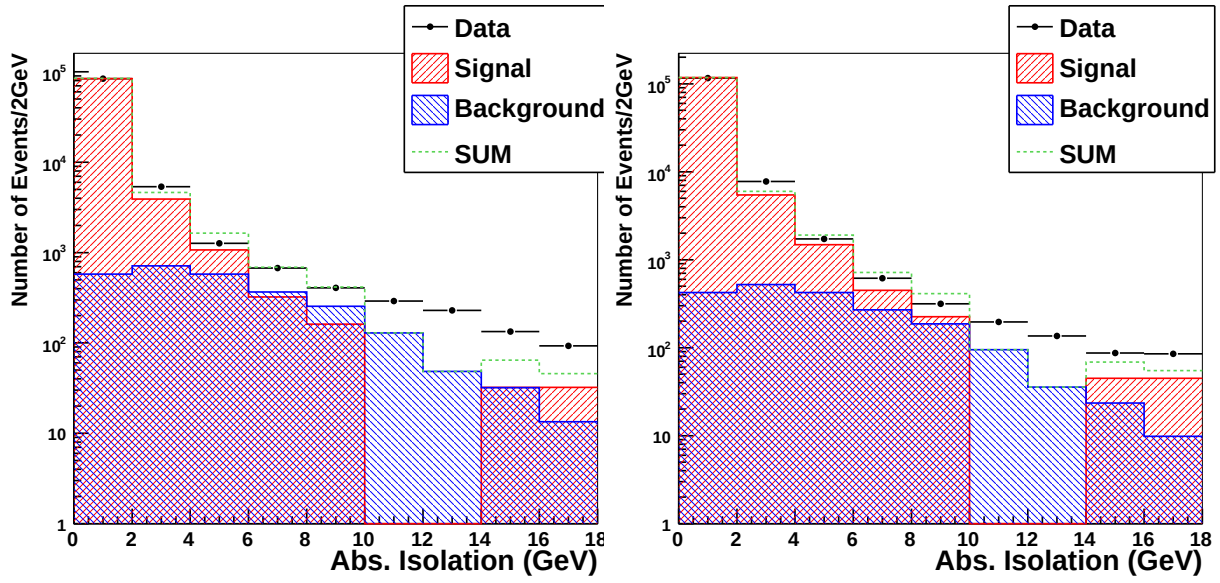

Figure 3.11: Central Electron Isolation Energy distributions in $25 < \not\!\!E_T < 35$ (left) and in $35 < \not\!\!E_T$ (right).

considered in Monte Carlo.

3.5.2 Central Tracking Efficiencies

The COT tracking reconstruction efficiency ϵ_{COT} is determined by measuring the fraction of $W \to e\nu$ events which have tracks to the $W \to e\nu$ events using only calorimeter information.

3.5.3 Trigger Efficiencies

Electron trigger efficiencies are depending on E_T, η event-by-event. Averaged trigger efficiencies of each run range, ϵ_{trig} are listed in Table 3.11.

Central Electron	**0d**	**0h**	**0i**
ϵ_{Trig}	$96.5 \pm 0.6\%$	$97.8 \pm 0.6\%$	$97.8 \pm 0.6\%$
SF_{ID}	$99.1 \pm 0.4\%$	$98.5 \pm 0.3\%$	$97.4 \pm 0.3\%$
Plug Electron	**0d**	**0h**	**0i**
ϵ_{Trig}	$96.5 \pm 0.4\%$	$97.8 \pm 0.3\%$	$97.8 \pm 0.3\%$
SF_{ID}	$94.7 \pm 0.8\%$	$92.6 \pm 0.6\%$	$92.0 \pm 0.7\%$
CMUP Muon	**0d**	**0h**	**0i**
ϵ_{Trig}	$90.2 \pm 0.4\%$	$91.9 \pm 0.4\%$	$91.8 \pm 0.5\%$
ϵ_{χ^2}	$98.5 \pm 0.2\%$	$98.8 \pm 0.1\%$	$98.6 \pm 0.2\%$
$SF_{ID} \times SF_{reconst}$	$93.6 \pm 0.5\%$	$92.9 \pm 0.5\%$	$91.7 \pm 0.6\%$
CMX Muon	**0d**	**0h**	**0i**
ϵ_{Trig}	$96.7 \pm 0.4\%$	$95.5 \pm 0.4\%$	$95.4 \pm 0.5\%$
ϵ_{χ^2}	$98.7 \pm 0.2\%$	$98.6 \pm 0.1\%$	$98.8 \pm 0.2\%$
$SF_{ID} \times SF_{reconst}$	$100.9 \pm 0.6\%$	$99.3 \pm 0.6\%$	$99.3 \pm 0.7\%$
ϵ_{COT}	$100.9 \pm 0.3\%$	$101.4 \pm 0.3\%$	$101.4 \pm 0.3\%$
ϵ_{Z_0}	$95.8 \pm 0.2\%$	$96.1 \pm 0.3\%$	$96.1 \pm 0.3\%$

Table 3.11: Lepton Trigger Efficiencies and Scale Factors.

3.5.4 Scale Factor

The efficiency of lepton ID is determined from Monte Carlo simulation. However, the simu-

lation is imperfect. The scale factor ($SF_{ID} = \epsilon_{Data}/\epsilon_{MC}$) are used to scale the Monte Carlo to better represent the efficiency measured in data. Scale Factors of each run range are listed in Table 3.11.

3.6 W Cross Section Results

The cross section times the branching ratio is calculated as

$$\sigma(W \to \ell\nu) = \frac{N_{data} - N_{BG}}{\epsilon_{Trig} \times SF_{ID} \times \epsilon_{Z_0} \times \epsilon_{COT} \times \mathcal{A} \times \int \mathcal{L}dt}$$

- N_{data} : Number of Data.
- N_{BG} : Number of background.
- ϵ_{Trig} : Trigger efficiency.
- SF_{ID} : Lepton ID Scale factor.
- ϵ_{Z_0} : Z_0 vertex efficiency.
- ϵ_{COT} : Tracking efficiency.
- $\mathcal{A}$: Acceptance.
- $\int \mathcal{L}dt$: Integrated Luminosity.

As Monte Carlo samples we use the samples $W \to e\nu$ and $W \to \mu\nu$ to determine the signal acceptance, and for the background $W \to \tau\nu$, $Z \to ee$, and $Z \to \mu\mu$ are used. Based on these values, we obtained

$$\sigma_W \cdot Br(W \to \ell\nu) = 2.78 \pm 0.01(stat.)[nb]$$

The results agree to better than 1% between all the channels. A summary of the backgrounds is given in Table 3.12 separately for central electron, in Table 3.13 for plug electron, in Table 3.14 for muon.

We did not go through a full calculation of systematic uncertainties but they are certainly larger than 1%. The results also agree well with the published result of 2775 ± 10(stat.) $\pm$ 53(syst.) $\pm$ 167(lum.) pb [63].

Figures 3.12, 3.13, and 3.14 show the lepton $E_T(p_T)$, the $\not\!\!E_T$ and the transverse mass. The agreement with the Standard Model prediction is very good.

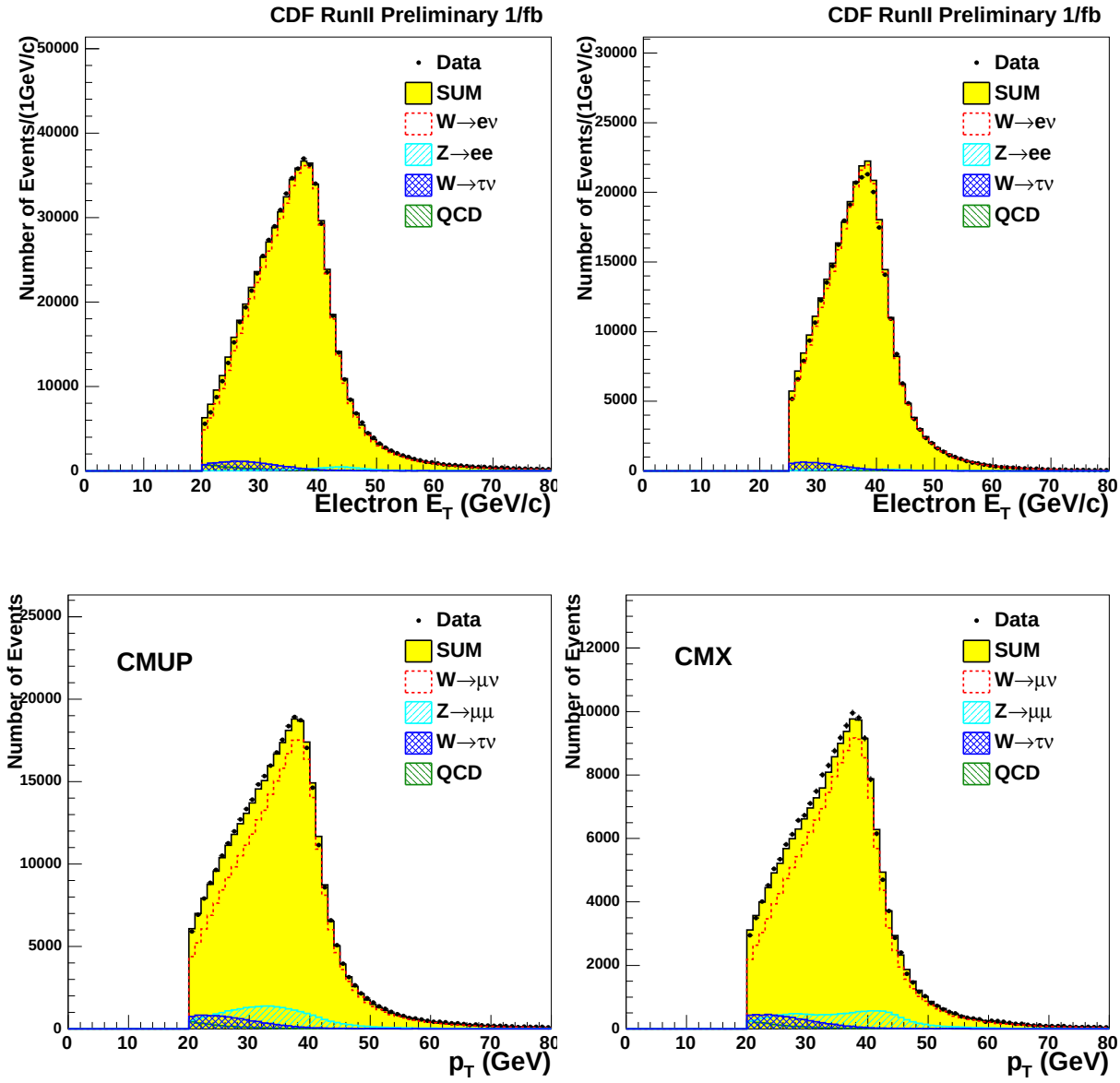

Figure 3.12: Lepton E_T or p_T distribution. Upper Left : Central Electron. Upper Right : Plug Electron. Lower Left : CMUP Muon. Lower Right : CMX Muon.

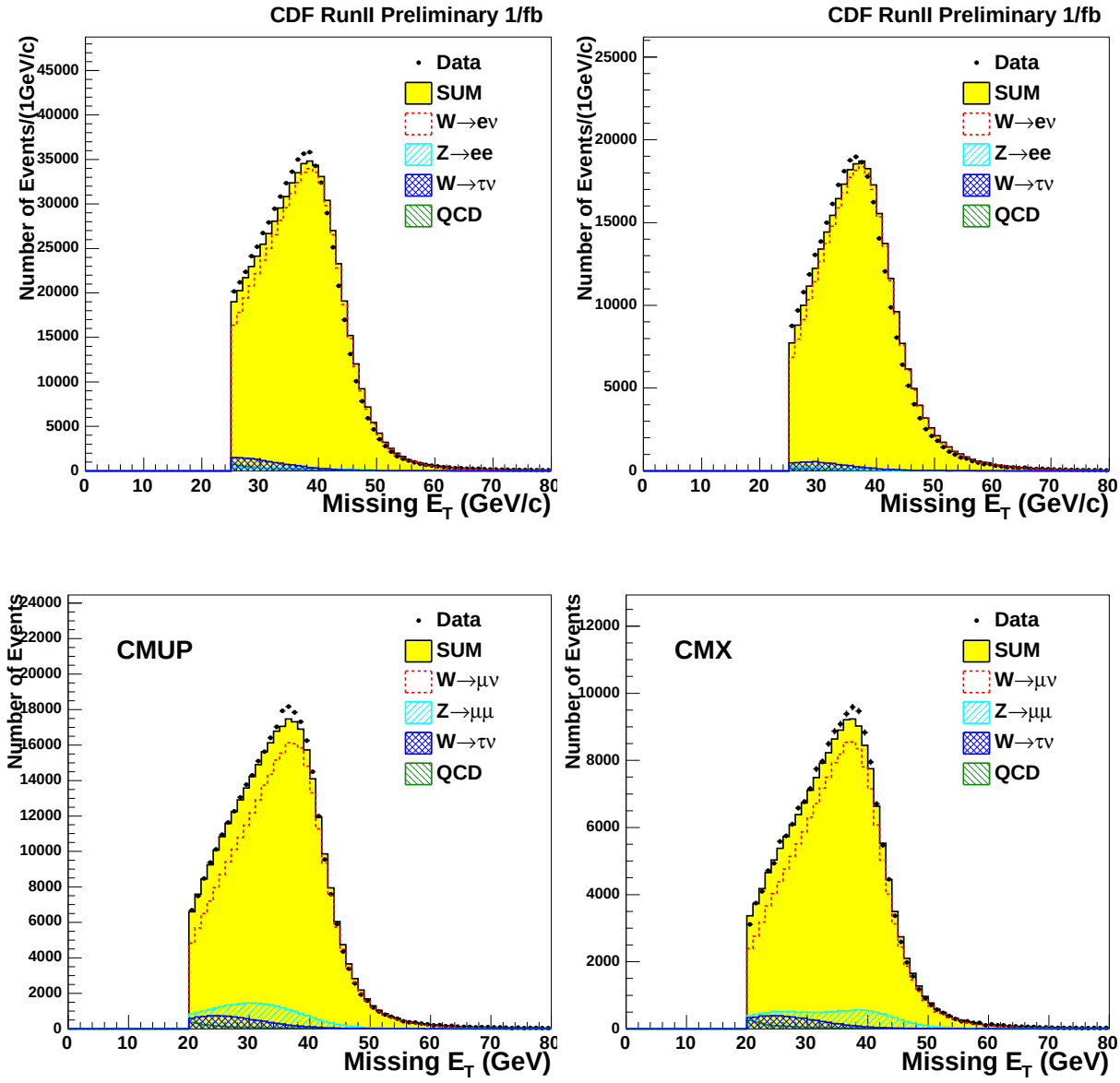

Figure 3.13: $\not\!\!E_T$ distribution. Upper Left : Central Electron. Upper Right : Plug Electron. Lower Left : CMUP Muon. Lower Right : CMX Muon.

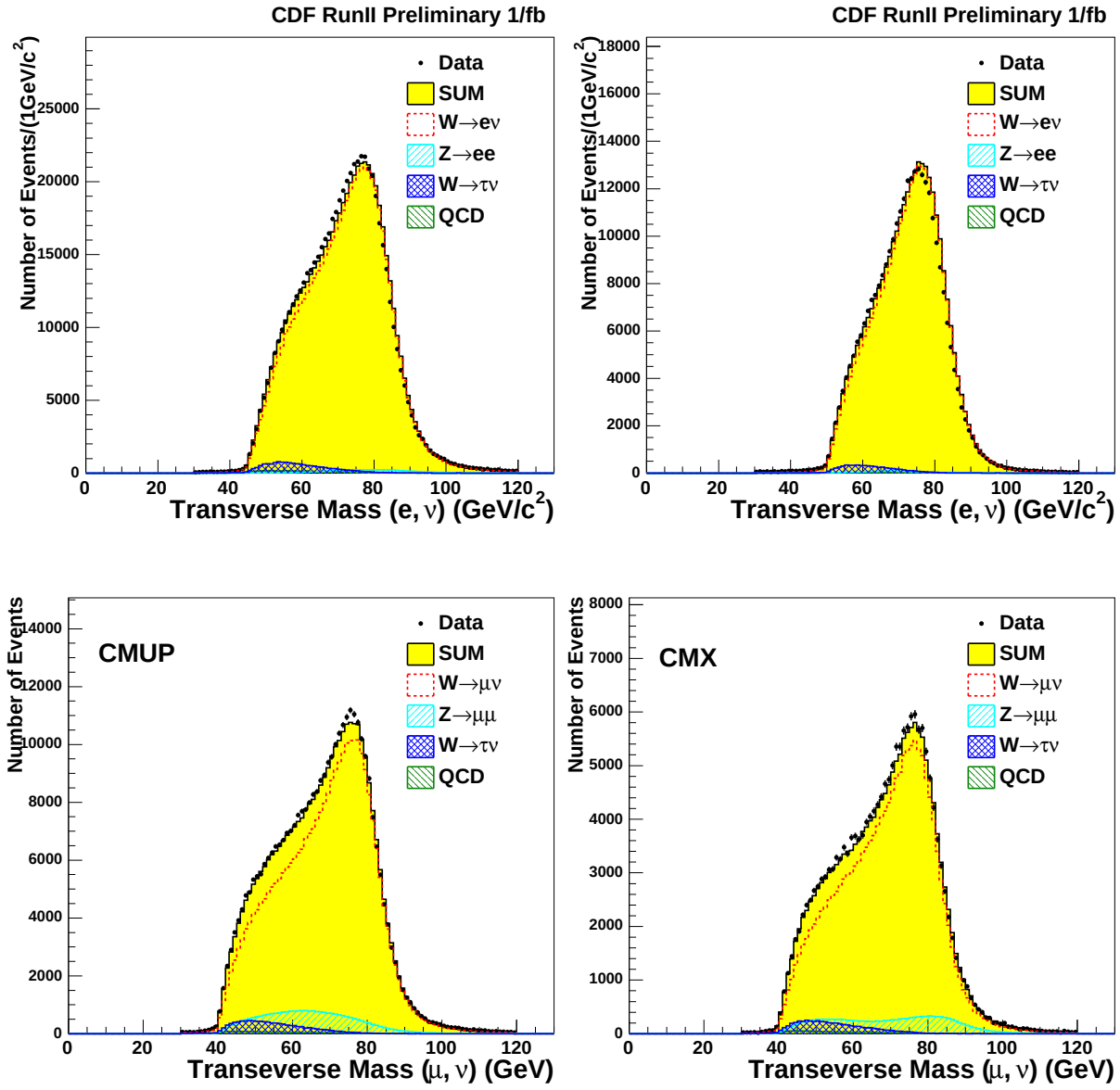

Figure 3.14: M_T distribution. Upper Left : Central Electron. Upper Right : Plug Electron. Lower Left : CMUP Muon. Lower Right : CMX Muon.

Central Electron Channel	Number of Events
Number of Data	616943
$\mathcal{A}$	0.204
ϵ_{all}	0.959
$\int \mathcal{L}dt$	1101.67±45.12
QCD	5917±143(stat.)
$W \rightarrow \tau\nu$	15568±104(stat.)
$Z \rightarrow ee$	6827±19(stat.)
$\sigma(W \rightarrow e\nu)$/nb	2.732
$\delta(\sigma)$/nb (stat.)	0.003
$\delta(\sigma)$/nb (lumi.)	0.112

Table 3.12: Summary of $W \rightarrow$ central $e\nu$ cross section

Plug Electron Channel	Number of Events
Number of Data	302196
$\mathcal{A}$	0.204
ϵ_{all}	0.990
$\int \mathcal{L}dt$	1019.67± 59.14
QCD	1186±2(stat.)
$W \rightarrow \tau\nu$	6129±35(stat.)
$Z \rightarrow ee$	2279±10(stat.)
$\sigma(W \rightarrow e\nu)$/nb	2.701
$\delta(\sigma)$/nb (stat.)	0.008
$\delta(\sigma)$/nb (lumi.)	0.157

Table 3.13: Summary of $W \rightarrow$ plug $e\nu$ cross section

3.6.1 W Event Yield

Figure 3.15 shows the event yield of W candidates per inverse pico barn as a function of run number.

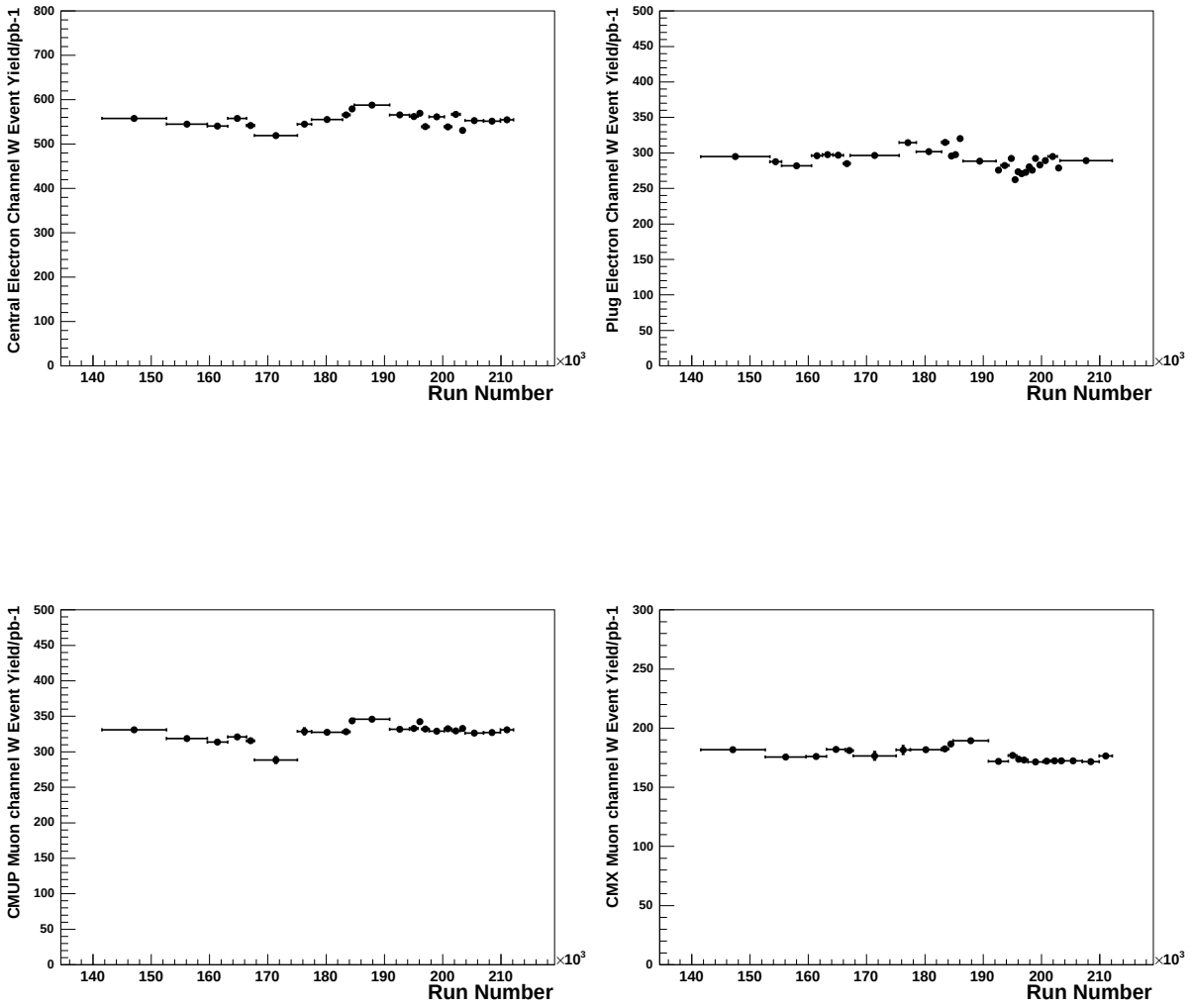

Figure 3.15: Event yield of $W \rightarrow l\nu$ candidates per luminosity. The upper left : Central Electron, the upper right : Plug Electron, the lower left : CMUP Muon, the lower right : CMX Muon.

Muon Channel	Number of Expected
Number of Data	520818
$\mathcal{A}$	0.105
ϵ_{all}	0.844
$\int \mathcal{L}dt$	1030.94±61.86
QCD	4548.62±0.15(stat.)
$W \to \tau\nu$	15807.40±0.60(stat.)
$Z \to \mu\mu$	40311.05±0.39(stat.)
$\sigma(W \to \mu\nu)$/nb	2.781
$\delta(\sigma)$/nb (stat.)	0.005
$\delta(\sigma)$/nb (lumi.)	0.167

Table 3.14: Summary of $W \to \mu\nu$ cross section

Chapter 4

Photon Identification

In this chapter, we describe a measurement of the rate at which jets fake photons by passing standard photon selection cuts is described. The jet fakes to photon event is the biggest background in $W\gamma$ events. The fake rate is applied to the jets produced in association with inclusive W/Z bosons, thus providing a data-driven measurement of this background to $W\gamma$ and $Z\gamma$ events. To measure the background from $W + jet$ events, the probability at which a jet fakes a prompt photon is estimated from the data. Using jet triggered events, the ratio of the number of prompt photon to the number of jets is estimated.

4.1 Definition of Fake probability

The number of background events from jets faking photons in central region is given by

$$\begin{aligned} N_{BG}(E_T^{\gamma}) &= \int P^{W}_{jet\to\gamma}(E_T^{jet}) \times dN_W/dE_T^{jet}dE_T^{jet} \\ &= \int P^{jet}_{jet\to\gamma}(E_T^{jet}) \times \frac{dN_W/dE_T^{jet}}{dN_{jet}/dE_T^{jet}} dN_{jet}/dE_T^{jet}dE_T^{jet} \end{aligned}$$

In plug region, we set fake rate with η dependence,

$$\begin{aligned} N_{BG}(\eta^{\gamma}) &= \int P^{W}_{jet\to\gamma}(\eta^{jet}) \times dN_W/d\eta^{jet}d\eta^{jet} \\ &= \int P^{jet}_{jet\to\gamma}(\eta^{jet}) \times \frac{dN_W/d\eta^{jet}}{dN_{jet}/d\eta^{jet}} dN_{jet}/d\eta^{jet}d\eta^{jet} \end{aligned}$$

where

- $P^{W}_{jet\to\gamma}$ is the jet to photon fake rate in W sample. We measured the jet to photon fake rate using jet sample and applied on W sample. Therefore we assigned systematic uncertainty based on the relative fraction of quark gluon fraction. In the following section, $P^{jet}_{jet\to\gamma}$ will be referred to as "true fake rate" and $P_{raw} = N_{\gamma candidate}/N_{jet}$ as the "raw fake rate". The selected γ candidates passed photon cuts are a combination of photons from hadronic decay ("fake" photons) and photons from direct production or bremsstrahlung radiation ("prompt" photons).

- $dN_W/d\eta^{jet}$ is the η distribution in W event. The term $(dN_W/d\eta^{jet})/(dN_{jet}/d\eta^{jet})$ cancels when η distribution in jet sample and η distribution in W sample are same shown in Figure 4.1. We observed E_T dependence on central fake rate but we found no E_T dependence in plug region.

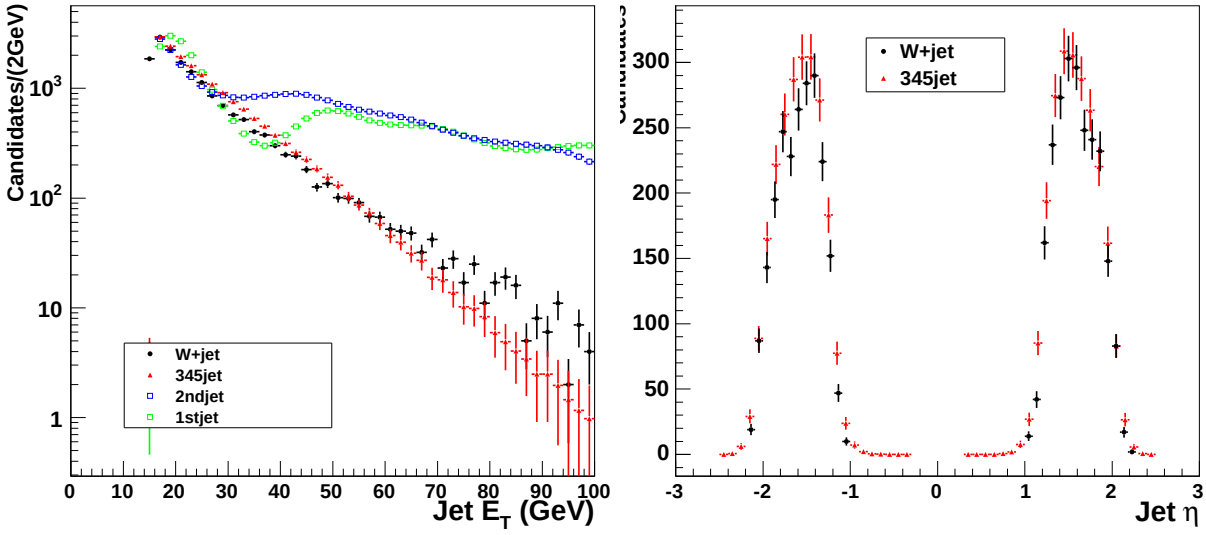

Figure 4.1: The E_T distribution in W sample comparing to the 345th E_T distribution in jet sample (left). Number of events normalized between 15 and 40 GeV. The η distribution in W sample comparing to the 345th jet η distribution in jet sample (right).

4.2 Photon Selection

The photon identification is similar to the electron identification except for the tracking requirement.

4.2.1 Central Photon Selection

Photons and electrons leave almost the same signals in the calorimeter systems of CDF. The same clustering algorithm for electromagnetic clusters and the same definitions for E and E_T are used for photons are electrons. An obvious difference is that photons will not have a track in the tracking chamber. Photon objects are formed from energy clusters in neighboring towers of the calorimeter. An energy cluster is made from an electromagnetic seed tower and at most one additional tower that is adjacent to the seed tower in η and within the same ϕ wedge. The seed tower must have $E_T > 2$ GeV and no track pointing at cluster.

Central Photon Selection Variables

The selection requirements are applied to photon candidates.

- $CES|x|, CES|z|$:
  The photon candidates are required to be in the central region of the CDF detector to ensure they pass through enough tracking volume that a track would have been detected if they were actually electrons instead of photons.

- E_{HAD}/E_{EM} :
  A photon produced at the center of the detector will deposit most of its energy in the electromagnetic calorimeter with only a small amount in the hadronic calorimeter.

- $\frac{1}{2}(\chi^2_{strips} + \chi^2_{wires})$:
  The comparison of the CES shower profile in the strip and wire views, to the profile extracted from test beam electrons, is used to distinguish between electromagnetic showers from prompt photons and from hadron decays (eg. $\pi^0 \rightarrow \gamma\gamma$). A χ^2 is formed between the data and the test beam electrons.

- Secondary CES cluster $E_{wire} \times \sin\theta$, $E_{strip} \times \sin\theta$:
  where θ is the angle of the photon. A major source of background to prompt photons are neutral mesons which decay into two photons. These should produce two CES clusters compared to the single CES cluster produced by a prompt photon.

- Calorimeter isolation :
  The calorimeter isolation is defined in the same way as for electron candidates.

- Track isolation Σp_T :

  The calculation of the track isolation variable contains the sum of all tracks with a z_0 within 5 cm of the event vertex and in 0.4 cone around the photon candidate.

- N_{tracks} :

  The number of tracks, leading to the electromagnetic energy cluster, is used to separate the photon candidates from electrons.

The central photon selection is given in Table 4.1.

Variable	**Photon Cut**
E_T^γ	> 15 GeV
$\|\eta\|$	< 1.1
$CES\|x\|$	< 21 cm
$CES\|z\|$	> 9 and < 230 cm
E_{HAD}/E_{EM}	< 0.15 or $< 0.055 + 0.00045 * E$
$\frac{1}{2}(\chi^2_{strips} + \chi^2_{wires})$	> 0 and < 20
2nd CES $E_{wire} \times \sin\theta$	$< 2.4 + 0.01E_T^\gamma$ and $< 0.14E_T^\gamma$
2nd CES $E_{strip} \times \sin\theta$	$< 2.4 + 0.01E_T^\gamma$ and $< 0.14E_T^\gamma$
Calorimeter isolation	$< 2.0 + 0.02(E_T^\gamma - 20)$ and $< 0.1E_T^\gamma$
Track isolation: Σp_T	$< 2.0 + 0.005E_T^\gamma$
N_{tracks} with $p_{T,track} \leq 1 + 0.005E_T^\gamma$	1
N_{tracks} with $p_{T,track} > 1 + 0.005E_T^\gamma$	0

Table 4.1: Central Photon selection cuts.

4.2.2 Plug Photon Selection

The plug photon identification cuts are detailed in Table 4.2. Also we selected plug photons which does not match to any tracks.

4.3 $W + \gamma$ Backgrounds

The following background sources have been considered:

Variable	Plug Photon
E_T	> 15 GeV
$PES\ \eta$	$1.2 < \|\eta\| < 2.0$
E_{HAD}/E_{EM}	$< 0.05 + 0.026 \times E$ (if $E \geq 100$)
	> 0.05 (if $E < 100$)
Isolation	< 4 GeV
$PEM3 \times 3\chi^2$	< 10
$PEM5 \times 9U, PEM5 \times 9V$	< 0.65

Table 4.2: Plug Photon ID variables and cut values.

- electroweak backgrounds from $W\gamma \to \tau\nu\gamma$ and $Z\gamma \to e^+e^-\gamma$ production are evaluated using the Monte Carlo samples described above.

- QCD jet background is determined from the data. This background arises from jet production where the jet is misidentified as a photon. Background where a jet is misidentified as a electron is negligible.

The jet background is estimated using the fake rate measurement detailed in Chapter. 4. The largest background is W+jet production with about 30%, followed by $Z\gamma$ production with about 20%. The $W \to \tau\nu\gamma$ background contributes only 2%.

4.3.1 Cluster Transverse Mass

All the $W + \gamma$ production diagrams interfere each other and then measured in the CDF detector. These diagrams can not be rigorously separated, but using the cluster transverse mass, we can reduce the contamination of the final state radiation diagram and enhance s-channel diagram contribution considerably.

The cluster transverse mass of the $W\gamma$ system is defined by [64],

$$M_T^2(\ell\gamma, \not\!\!E_T) = \left[(M_{\ell\gamma}^2 + |\mathbf{p}_T^\gamma + \mathbf{p}_T^\ell|^2)^{1/2} + \not\!\!E_T\right]^2 - |\mathbf{p}_T^\gamma + \mathbf{p}_T^\ell + \not\!\!E_T|^2.$$

4.4 Datasets

The datasets used for this analysis are `JET_20`, `JET_50`, `JET_70`, and `JET_100` which jets are triggered by E_T more than 20 GeV, 50 GeV, 70 GeV, and 100 GeV respectively. Requiring a good detector status, we obtain luminosities of 1101.665 pb^{-1}. To determine prompt photon template, high p_T plug electron data are used. As Monte Carlo samples we use the samples HERWIG di-jet Monte Carlo with Minimum Bias to determine fake photon template.

4.5 Event Selection

The events are required to be triggered by the `JET_20, JET_50, JET_70, JET_100` triggers. The jets are numbered according to their E_T. The highest E_T jet in a event is called "1st jet", second highest E_T jet called "2nd jet", third and lower called "345th jet".

- 1st jet is excluded from this analysis in order to remove trigger bias.
- 2nd jet is also excluded from fake rate measurement, used only for systematic uncertainty study because it has different E_T spectrum from W+jet.
- 1st jet and 2nd jet can exist either central or plug region.
- 1st jet and 2nd jet should be separated $\Delta R > 0.8$.
- 345th jet are required to separated $\Delta R > 0.8$ from 1st and 2nd jet.

A jet which is overlapping to a photon with $\Delta R < 0.4$ is called photon candidate.

4.6 P_{raw} measurement

The measurement of P_{raw} is shown in Figure 4.2. P_{raw} is the number of photon candidates which passed photon identification in jet sample. The numerator includes both prompt and fake photon.

$$P_{raw} = \frac{N_{\gamma\ candidates}}{N_{jet}}$$

where $N_{\gamma\ candidates} = N_{prompt\ \gamma} + N_{fake\ \gamma}$. It is about 0.4 % both in central and plug region. The plug P_{raw} versus ϕ is shown in Figure 4.3. We observed the fake rate is independent of ϕ.

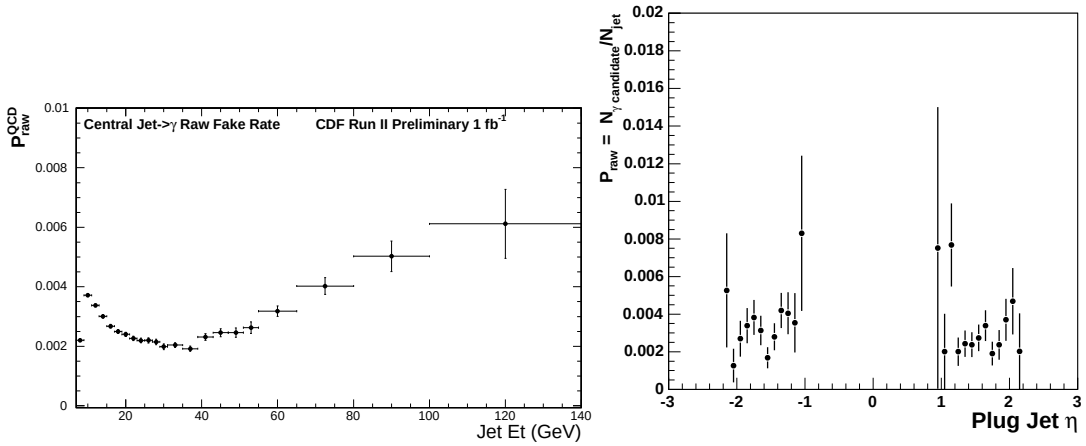

Figure 4.2: The Central P_{raw} versus E_T(left) and the plug P_{raw} versus η (right)

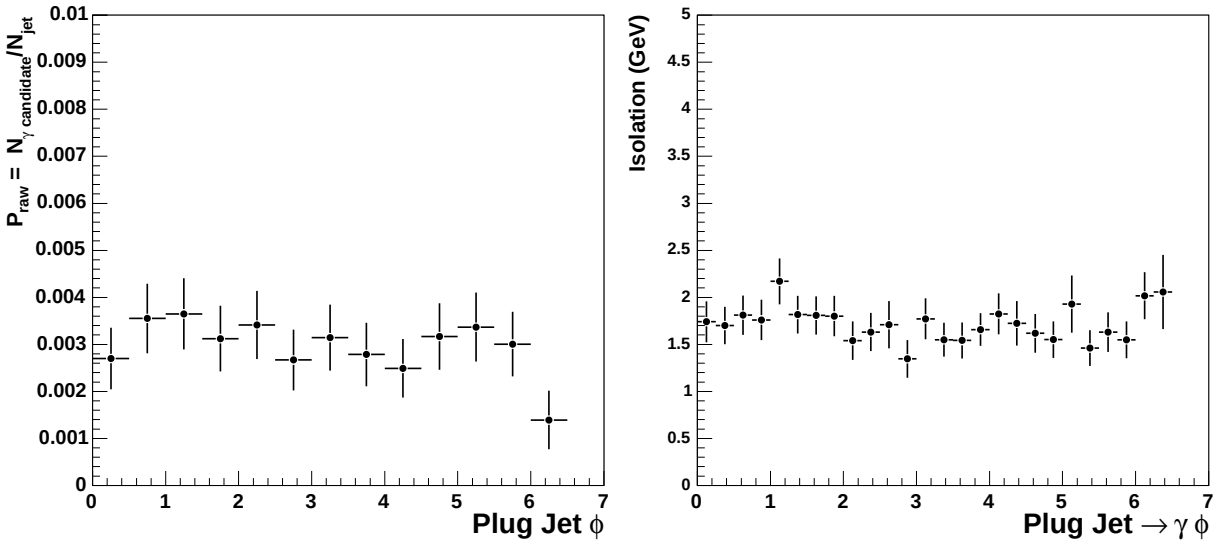

Figure 4.3: The P_{raw} versus ϕ (left) and the absolute isolation versus ϕ (right).

4.7 Fake photon fraction measurement in central region

The definition of F_{QCD} is given by $F_{QCD} = N(jet \rightarrow \gamma\ fake\ photon)/[N(jet \rightarrow \gamma\ fake\ photon)+ N(prompt\ photons)]$. F_{QCD} which estimates the fraction of fake photon, is applied to the raw fake rate to correct for prompt photon contamination. In this section, we describe three methods that are used to measure the F_{QCD} of central photon candidate.

4.7.1 CES Weighting Method

This method uses the Central Electromagnetic Shower (CES) detector, a strip and wire chamber, that is embedded in the Central Electromagnetic Calorimeter (CEM) wedges. The CES detector provides high-precision position measurement of the electromagnetic shower inside the calorimeter. A single photon shower is typically narrower than showers from $\pi^0 \rightarrow \gamma\gamma$ decays. For a given sample, the fraction of pion events can be determined from the fraction of "wide" showers in the sample.

The transverse shower profile measured from electron test beam data is used to distinguish electrons/photons from pions. A CES χ^2 variable is defined to describe how well the measured shower profile matches to an electron shower profile. A χ^2 ratio variable is calculated as:

$$\epsilon = \frac{N^{\chi^2<4}}{N^{\chi^2<20}}$$

where $N^{\chi^2<4}$ is the number of events with $\chi^2 < 4$ and $N^{\chi^2<20}$ is the number of events with $\chi^2 < 20$. Background events, in general, have larger χ^2 values and the ratio ϵ_b is smaller than ϵ_γ of photon events. This ratio in the data is equal to:

$$\epsilon_{data} = \frac{\epsilon_\gamma N_\gamma + \epsilon_b N_b}{N_{data}}$$

where,

$$N_{data} = N_\gamma + N_b$$

and the background fraction can be calculated as:

$$F_{QCD} = \frac{N_b}{N_{data}} = \frac{\epsilon_{data} - \epsilon_\gamma}{\epsilon_b - \epsilon_\gamma}$$

4.7.2 CPR Weighting Method

This method uses the Central Pre-Radiator (CPR) detector that is mounted on the inner surface of the CEM wedges. The solenoid and the Central Outer Tracking (COT) detector are served as radiators for the CPR detector. The conversion rate of prompt photons and pions in the solenoid is measured by the charge deposited in the CPR detector. Let the conversion rate of a single photon be P_γ, the conversion probability of a pion ($\pi^0 \to \gamma\gamma$), where both photons can convert, is equal to $1-(1-P_\gamma)^2$. If the single photon conversion rate is 60%, the conversion rate of a pion is then 84%. By measuring the fraction of events that deposit significant charge in the CPR detector, the background fraction can be extracted. Similar to the CES Weighting method, a CPR weight can be constructed by comparing the conversion probabilty in the data to the conversion probabilities known for signal and background.

4.7.3 Isolation ratio vs. CES χ^2 Method

In a two-dimensional distribution of the calorimeter isolation ratio variable and the CES χ^2 variable, signal events congregate in the low isolation ratio and low χ^2 region, while background events have large isolation ratio due to hadronic activity. The two-dimensional plane of isolation ratio v.s. χ^2 can be divided into four regions shown in Table 4.3, where C is the signal region and A, B, and D are control regions. Assuming no correlation between the iso/E_T and the CES χ^2 for background events, the background in region C can be determined as:

$$\frac{N_C^{BG}}{N_A} = \frac{N_B}{N_D}$$

and

$$F_{QCD} = \frac{N_C^{BG}}{N_C} = \frac{N_B N_A}{N_D N_C}$$

The CES χ^2 and the isolation ratio v.s. χ^2 method break down for events with $E_T > 40$ GeV, where the two photons from pion decays are too close together and the two-photon showers become too similar to single prompt photon showers. In the high E_T region, the CPR method is used to evaluate F_{QCD}.

4.7.4 Central F_{QCD} Result

Figure 4.4 shows the new measurement of F_{QCD} using the three methods described above as a function of E_T^{jet}. The data suggests that the raw fake rate sample possesses a small "prompt" photon contamination at lower energies and large "prompt" photon contamination at higher energies. The three methods do not agree with each other within statistical limits. Specifically, the CPR weighting method predicts a significantly higher F_{QCD} than the CES weighting method for all energy values, while the isolation ratio v.s. CES χ^2 agrees with the CPR method at lower energies and with CES method by around 30 GeV. We have taken into account this discrepancy in the form of a systematic error band, which encompasses the data points from all three methods. Additionally, because the CPR detector was replaced midway through data-taking, the CPR Weighting method could only be use for a roughly one-third of the available data. This does not represent a large statistical gain over the previous measurement and especially reduces the precision of the measurement at energies above 40 GeV, where the CPR weighting method is our only handle on F_{QCD}.

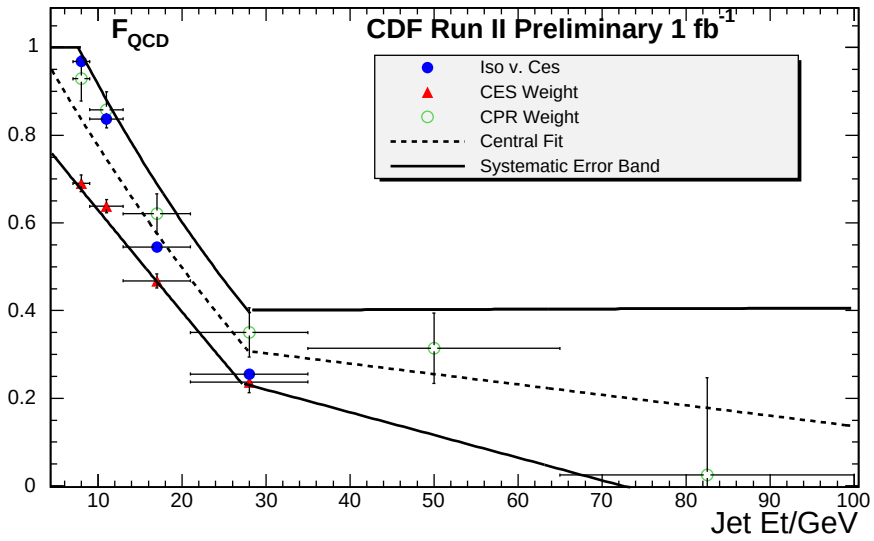

Figure 4.4: Central F_{QCD} v.s. Jet E_T. F_{QCD} is measured using three method: CES weighting method, CPR weighting method and isolation ratio v.s. CES χ^2 method.

4.8 Fake photon fraction measurement in plug region

For plug F_{QCD}, we estimated F_{QCD} in plug region by fitting the isolation energy distribution with prompt photon template and fake photon template.

4.8.1 Prompt photon template selection

Prompt photon template is made from the high p_T plug electron data with `PLUG_ELECTRON_20` trigger requiring $Z \rightarrow ee$ selection. Central(tighter leg)-plug(fitting leg) or plug(tighter leg)-plug(fitting leg) are selected. Central electron tighter leg passed central electron ID and $iso/E_T < 0.05$ and $L_{shr} < 0.1$. Plug electron tighter leg passed standard plug electron ID (written in Table 4.4) and $iso/E_T < 0.05$. Plug electron fitting leg passed standard plug electron ID (written in Table 4.4) except isolation cut. We also required invariant mass cut, 81 GeV/c^2 $< M_{ee} <$ 101 GeV/c^2.

4.8.2 Fake photon template selection

Fake photon template is made from di-jet Monte Carlo. One photon passed all photon ID except Isolation cut(Table 4.2) plus one jet events detailed in Table 4.5 are selected. Figure 4.5 shows the Isolation distribution for jet $\rightarrow \gamma$ candidate fitted with prompt photon template and fake photon template in each η region.

4.9 Central True Fake Rate

Following the procedure, we multiplied the raw fake rate by the "true" photon contamination to obtain the true fake rate for the jet sample: $P_{true}^{QCD}(E_T) = F_{QCD}(E_T) \times P_{raw}(E_T)$.

Monte Carlo studies from the previous fake rate analysis suggest that the jet sample is composed of jets with a different mixture quark and gluon parents than the W/Z sample, where the fake rate will be applied. Jets originating from quarks will have a different fake rate than those originating from gluons. As a result, the fake rate will be sensitive to the differing quark and gluon parent mixtures in the samples. Monte Carlo studies have also shown that the quark jet fake rate dominates the gluon jet fake rate, so that we can assume the fake rate in any sample is determined by its quark jet content alone (see Figure 4.7). We scale the $P_{true}^{QCD}(E_T)$ to $P_{true}^{W/Z}(E_T)$ then by the ratio of the quark jet content in the W/Z

	$E_t^\gamma < 20$		$E_t^\gamma > 20$	
A	$Iso/E_T < 0.1$	$\langle\chi^2\rangle > 20$	$(Iso - 2/E_T - 20) < 0.02$	$\langle\chi^2\rangle > 20$
B	$Iso/E_T > 0.2$	$\langle\chi^2\rangle > 20$	$(Iso - 2/E_T - 20) > 0.06$	$\langle\chi^2\rangle > 20$
C	$Iso/E_T < 0.1$	$\langle\chi^2\rangle < 20$	$(Iso - 2/E_T - 20) < 0.02$	$\langle\chi^2\rangle < 20$
D	$Iso/E_T > 0.2$	$\langle\chi^2\rangle > 20$	$(Iso - 2/E_T - 20) > 0.06$	$\langle\chi^2\rangle > 20$

Table 4.3: Cut values determining regions used for isolation ratio v.s. averaged CES χ^2 Method

Variable	Plug Electron
E_T	≥ 25 GeV
$\lvert PES2DEta\rvert$	$1.2 < \eta < 2.0$
E_{HAD}/E_{EM}	< 0.05
Isolation Energy	≤ 4 GeV
$\lvert z_0\rvert$	< 60 cm
PEM3x3FitTower	$\neq 0$
χ^2_{PEM}	< 10
PES 5x9 UV	> 0.65
ΔR_{PESPEM}	≤ 3 cm
PHX Track Matching	true
$N_{SiliconHits}$	≤ 3

Table 4.4: Plug Electron ID variables and cut values.

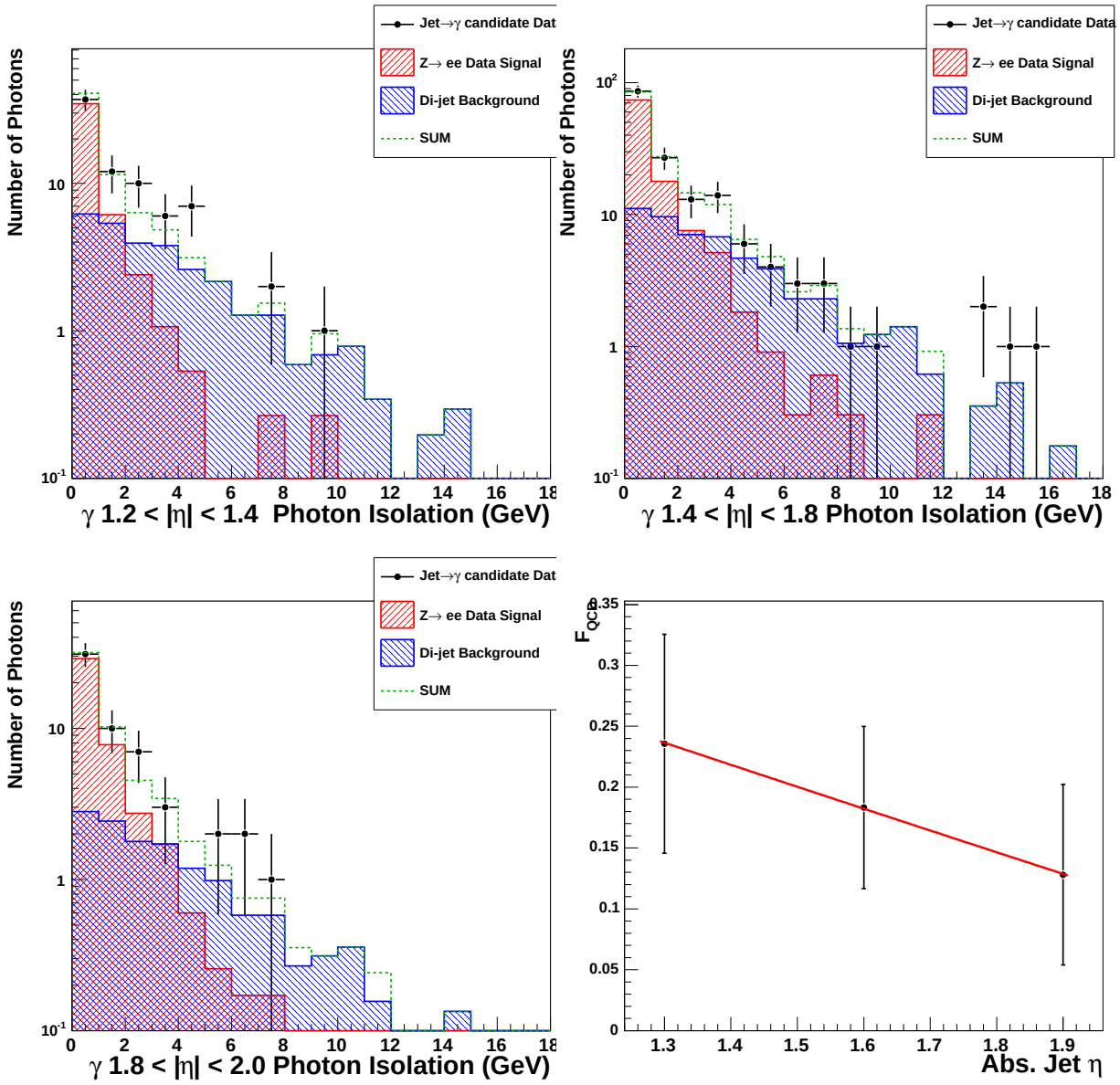

Figure 4.5: Isolation distribution for jet $\rightarrow \gamma$ candidate (black point) fitted with prompt photon template (red) and fake photon template (blue) in $1.2 < |\eta| < 1.4$ (upper left), $1.4 < |\eta| < 1.8$ (upper right) and $1.8 < |\eta| < 2.0$ (lower left).

Variable	JET
E_T	≥ 15 GeV
region	central or plug
E_{HAD}/E_{EM}	≥ 0.05
Cone size	0.4
$\lvert\Delta\phi_{jet,jet}\rvert$	≤ 2.8
$\mathrm{N}_{EMObject}$	=1
N_{Jet}	=1

Table 4.5: Jet Selection for fake photon template.

sample to quark jet content in the QCD sample, $F_{q/g}(E_T)$. Figure 4.8 plots the quark/gluon ratios for the W/Z sample from Alpgen W+1 Jet Monte Carlo and the QCD sample from Pythia Jet Monte Carlo. Figure 4.9 plots the difference of the quark ratio between the W/Z sample and the W+1 sample. The final result, $P_{true}^{W/Z}(E_T)$, is overlaid with the unscaled true fake rate, $P_{true}^{QCD}(E_T)$, and plotted in Figure 4.6 with appropriate final error bands.

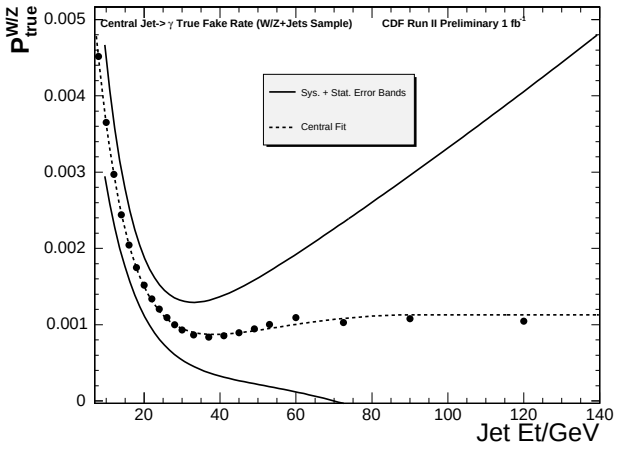

Figure 4.6: The Central P_{true} corrected by quark fraction.

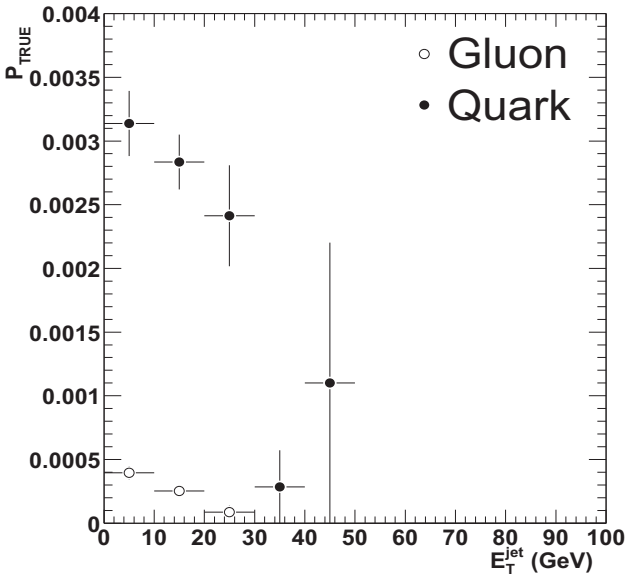

Figure 4.7: Central Fake Rate of Jets originating from Quarks (filled) and Gluons (empty)

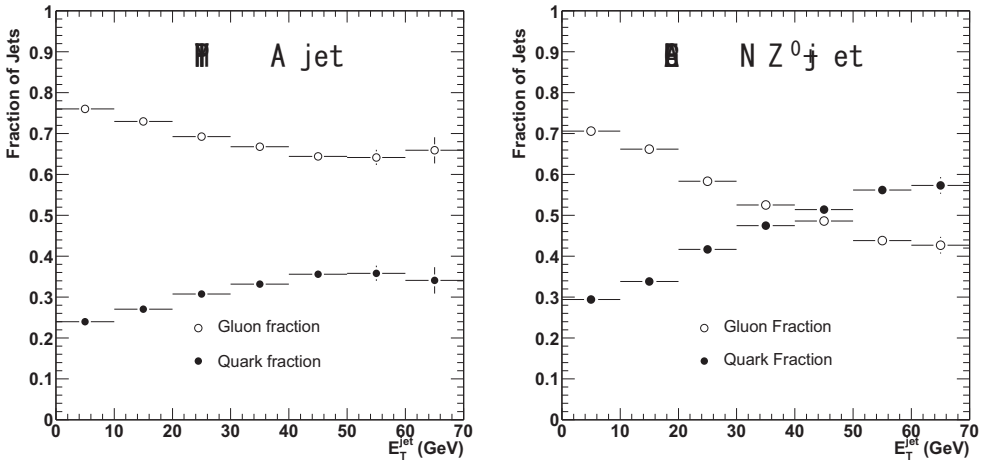

Figure 4.8: Fraction Contribution of Quark and Gluon Jets for PYTHIA jet MC (left) and Alpgen Z+jet MC (right) in central region.

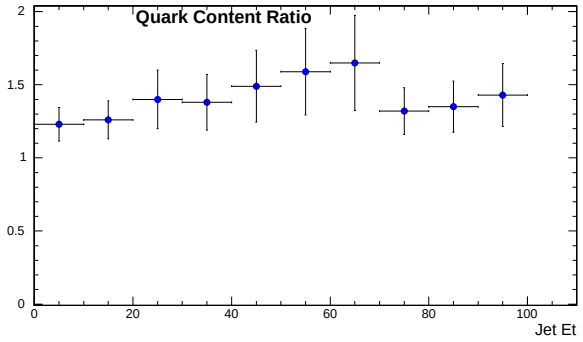

Figure 4.9: The expected quark content in W/Z sample in central region.

	Fit	Range
Central Value	$\exp(-0.117x - 4.51)$ +0.0000246x-0.000000134x^2	$7 - 92$ GeV
	0.00112	92+ GeV

Table 4.6: Central $P_{true}^{W/Z}(E_T)$ Fit Parameters

4.10 Plug Fake Probability $P_{true} = P_{raw} \times F_{QCD}$

Figure 4.10 shows jet to photon fake rate in plug region. The P_{true} is taken as the average of the distribution.

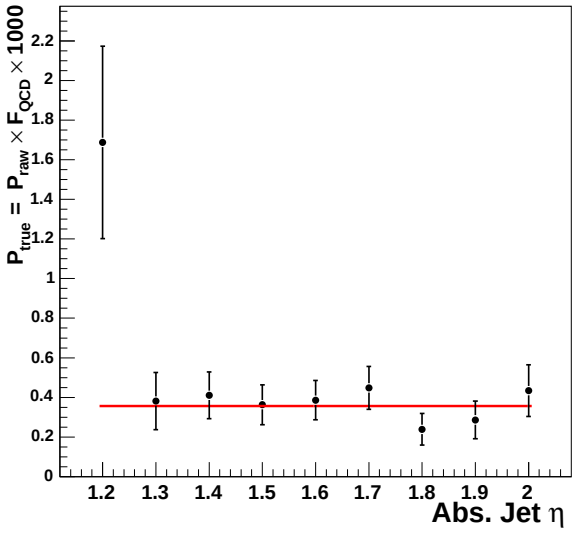

Figure 4.10: The P_{true} versus η.

4.11 Cross check isolation distribution fitting method using central photon.

We validated the isolation fitting method using central photon. The isolation distribution of jet $\rightarrow \gamma$ candidate in central region is fitted with prompt photon template which is made from high p_T central electron data with requiring $Z \rightarrow ee$ selection and fake photon template requiring one photon passed all photon ID except Isolation plus one jet events in di-jet Monte Carlo. Figure 4.11 shows F_{QCD} in central region. The F_{QCD} result is consistent with that estimated by CES-CPR weighting method or isolation ratio v.s. χ^2 method.

4.12 Systematic uncertainty

We have considered the following systematic uncertainty. We treat all these sources as uncorrelated and took the quadratic sum of all these sources. We understand that we may

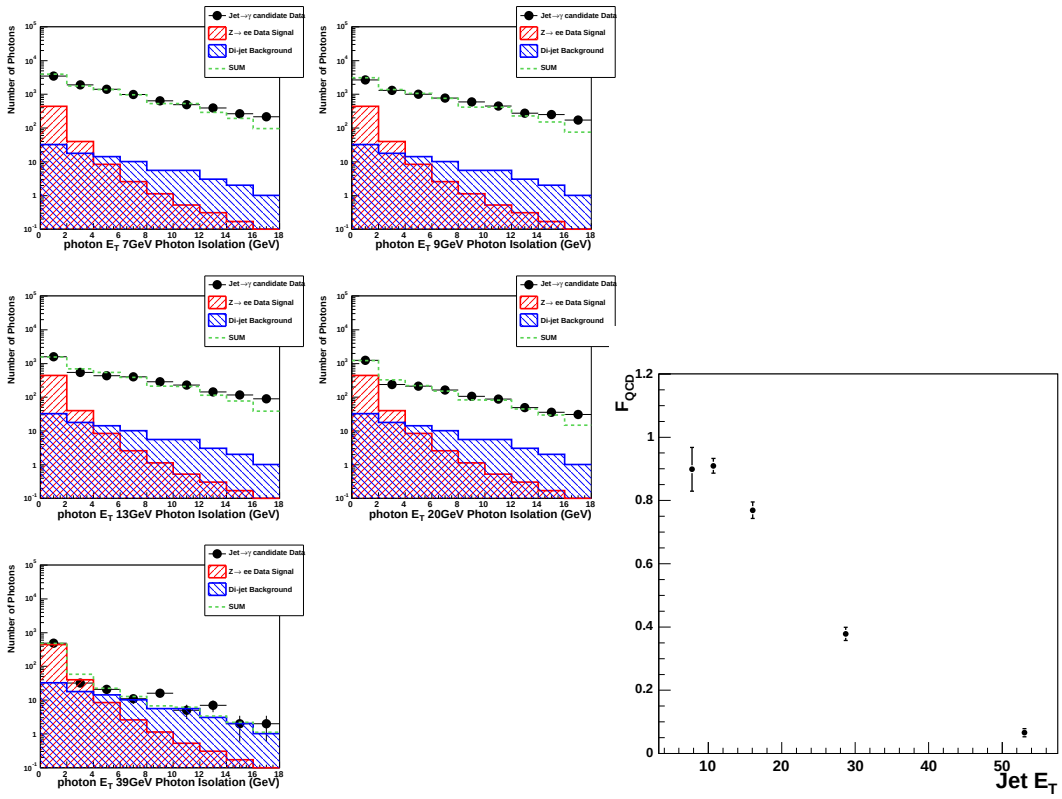

Figure 4.11: The isolation distributions and F_{QCD} in central region. The isolation distribution for jet $\rightarrow \gamma$ candidate (black point) fitted with prompt photon template (red) and fake photon template (blue) in different photon E_T range.

double-count some uncertainties however we are mostly concerned about quoting the result within the error. Relative systematic uncertainties are shown in Figure 4.12. We took the average over the quadratic sum of all these uncertainties.

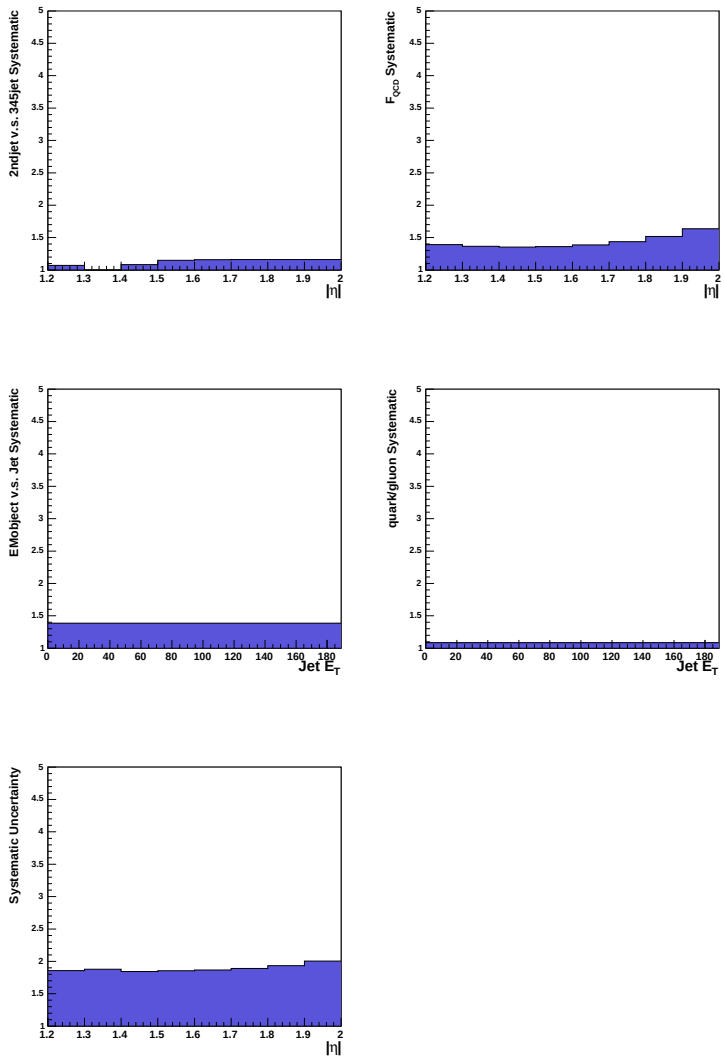

Figure 4.12: Systematic uncertainty on plug fake rate. The difference between 2nd and 345 jet (upper left). F_{QCD} fitting statistical error (upper right). The difference between EM object and jet (middle left). The difference quark/gluon fraction between jet sample and W/Z sample (middle right). Quadratic sum of all above (lower left).

4.12.1 Statistical limit on F_{QCD}

The statistical error on F_{QCD} is taken into account.

4.12.2 Comparison of 2nd jet to 345th jet

2nd jet has a different E_T distribution from 345th jet as shown in Figure 4.1. Both the P_{raw} and F_{QCD} differ significantly between 2nd and 345th jet. Figure 4.13 shows jet to photon fake rate in plug region using 2nd jet. The ratio of the 2nd jet fake rate to 345th jet fake rate is taken as a systematic uncertainty since it represents an uncertainty on the procedure.

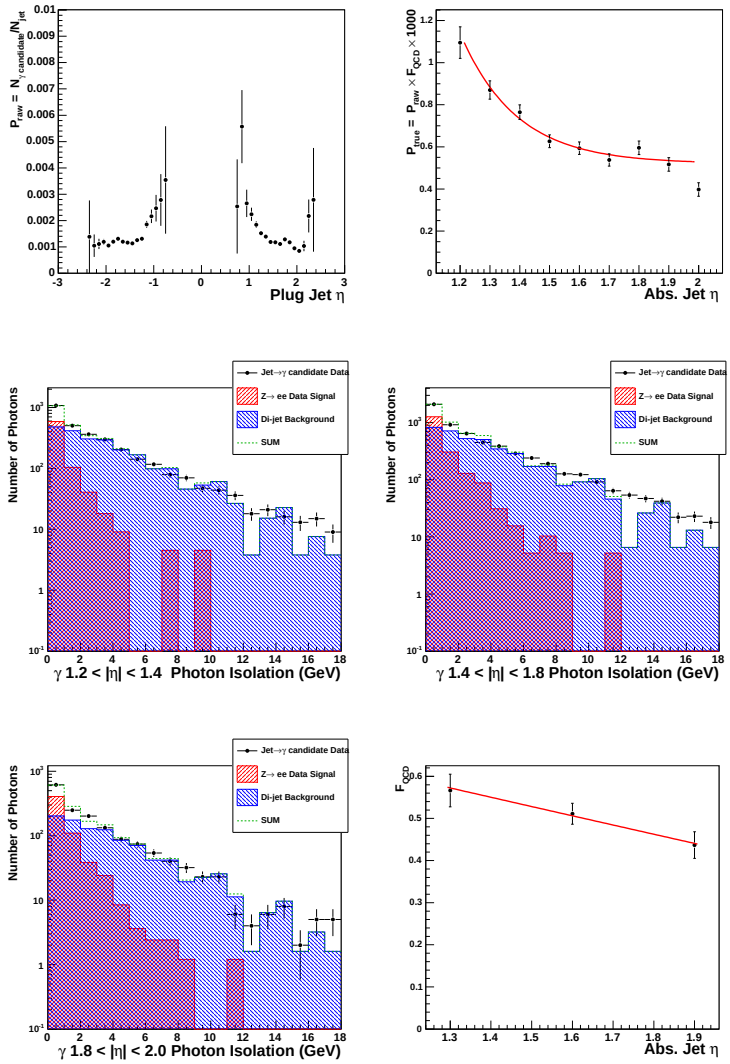

Figure 4.13: P_{raw} and P_{true} using 2nd jet (upper). Isolation distribution for jet $\rightarrow \gamma$ candidate (black point) fitted with prompt photon template (red) and fake photon template (blue) in $1.2 < |\eta| < 1.4$, $1.4 < |\eta| < 1.8$ and $1.8 < |\eta| < 2.0$ and F_{QCD} versus η.

4.12.3 EM base fake rate

We tested the fake rate measurement using EM object (electromagnetic energy clusters) instead of a jet. The EM based fake rate is measured from EM objects which has $1.2 < |\eta| < 2.0$ and $E_T > 15$ GeV. Because EM Objects contain only calorimeter information, they do not distinguish between electrons and photons. In order to exclude electrons, we required EM objects not matching to track. Also EM objects matching to 1st jet or 2nd jet are excluded. Both P_{raw}^{EM} and F_{QCD}^{EM} are different from the jet based fake rate shown in Figure 4.14. The EM fake rate is applied to W+EMobject events which has $1.2 < |\eta| < 2.0$, no associated track, and separated from the lepton $\Delta R > 0.7$. E_T distribution of W+jet applied W+jet based fake rate and W+EM object applied W+EM based fake rate after subtracting $W\gamma$ signal contamination are shown in Figure 4.15. The two methods are in good agreement. The difference between the two methods is included in systematic uncertainty.

4.12.4 Difference of Quark/gluon fraction between W sample and jet sample

We have measured a fake rate using jet triggered data and then will apply it to the W+jet data. This only will be valid if the jet in the W+jet data has the same properties as the 345th jet in jet triggered data. Figure 4.1 shows W+jet and 345th jet have same E_T distributions. We took into account the difference of quark/gluon fraction between di-jet Monte Carlo and W+jet Monte Carlo. The quark/gluon matching criterion are

- if a jet matching to a quark(gluon) within $\Delta R < 0.4$, label it "quark jet"("gluon jet").
- if a jet can match to more than one partons, take the parton which has the closest energy to the true level.

The fake rate is calculated by generator level information. $P_{jet\to\gamma}$ = [Number of a jet match to a reconstructed photon originated from the decay of π^0]/[Number of jet]. Figure 4.16 shows the fake rate using generator level information.

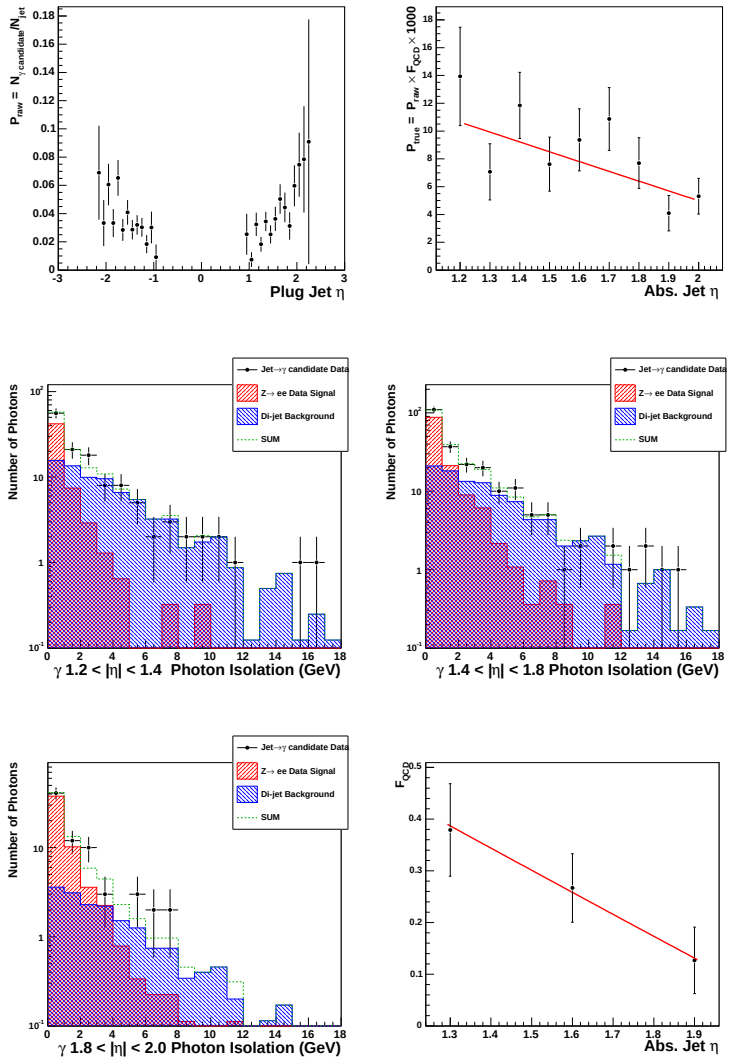

Figure 4.14: P_{raw} and P_{true} using EM object (upper). Isolation distribution for jet $\rightarrow \gamma$ candidate (black point) fitted with prompt photon template (red) and fake photon template (blue) in $1.2 < |\eta| < 1.4$, $1.4 < |\eta| < 1.8$ and $1.8 < |\eta| < 2.0$ and F_{QCD} versus η.

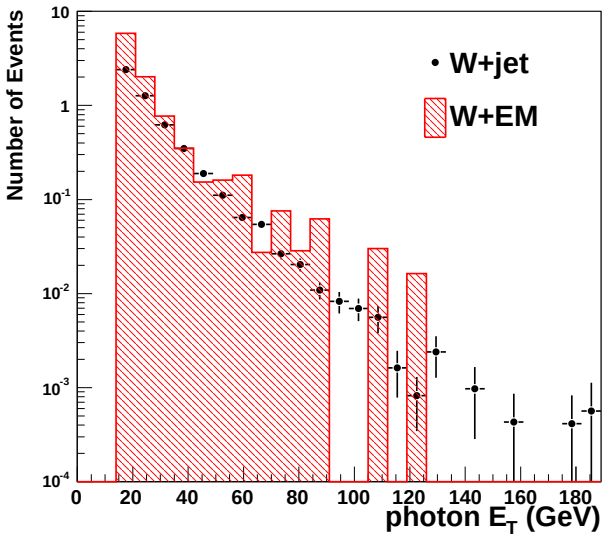

Figure 4.15: E_T distribution of W+jet applied W+jet based fake rate and W+EM object applied W+EM based fake rate after subtracting $W\gamma$ signal contamination.

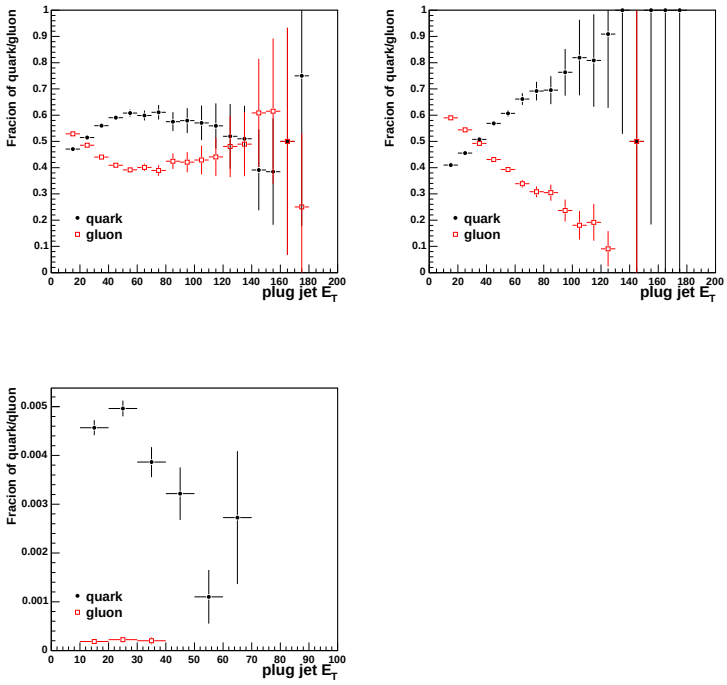

Figure 4.16: The quark/gluon fraction in W+jet Monte Carlo(left) and the quark/gluon fraction in di-jet Monte Carlo(right), used jets within $1.2 < |\eta| < 2.0$. The fake rate using generator level information from di-jet Monte Carlo (bottom).

Chapter 5

Results

5.1 $W + \gamma$ Monte Carlo

5.1.1 Leading Order Monte Carlo Generator

As Monte Carlo samples we use the samples:

- The $W\gamma \to \ell\nu\gamma$ process is simulated using the Monte Carlo program by U. Baur [12]. It contains initial and final state photon radiation and the tri-linear gauge coupling process, $W\gamma \to e\nu\gamma$ $W\gamma \to \mu\nu\gamma$ for signal and $W \to \tau\nu$ for background.
- The $Z\gamma$ background is determined using the U. Baur [60].

Generation was performed with using following input parameters detailed in Table 5.1. The geometrical selection is required in $W\gamma$ generation listed in Table 5.2.

5.1.2 Next to Leading Order Correction

The Baur's Monte Carlo generator is a leading order generator. To account for next-to-leading order corrections they are corrected by the k-factor determined in Ref. [61, 62] for the process of initial state radiation and the tri-linear coupling process. They are:

$$k(W\gamma, m(l\nu) > 76 \text{ GeV}) = 1.4308 + 2.042 \times 10^{-3} \cdot p_T - 6.761 \times 10^{-6} \cdot p_T^2$$

shown in Figure 5.1 fitted with photon p_T function. For the final state radiation process (selected by requiring invariant mass $M(l, \nu) < 76$ GeV) the k-factors of $\sigma_{NNLO}/\sigma_{LO} = 1.36$ for W and Z production are used. Here M is the invariant mass at generator level.

Variable	**Input Parameters**
Beam type	$p\bar{p}$
$\sqrt{s}$	1.96 TeV
PDF	CTEQ5L
α_s	0.127
M_W	80.41 GeV
M_Z	91.695 GeV
$\sin^2\theta_W$	0.231
α_{EM}	1/127.51
G_F	1.6637×10^{-5} GeV^{-2}
Γ_W	2.103 GeV
Γ_Z	2.514 GeV
M_{top}	175 GeV

Table 5.1: $W\gamma$ L.O. process Monte Carlo generation initial setting.

Photon Selection	
$\|\eta\|$	< 10
E_T	> 5 GeV
Lepton Selection	
$\|\eta\|$	< 10
E_T	> 0 GeV
Neutrino Selection	
$\|\eta\|$	< 10
E_T	> 0 GeV
$\Delta R(l,\gamma)$	> 0.2
Transverse mass $M_T(l,\, \nu)$	> 0 GeV
Cluster transverse mass $M_T(l,\, \nu,\, \gamma)$	> 0 GeV

Table 5.2: Geometrical selection in $W\gamma$ L.O. process Monte Carlo generation.

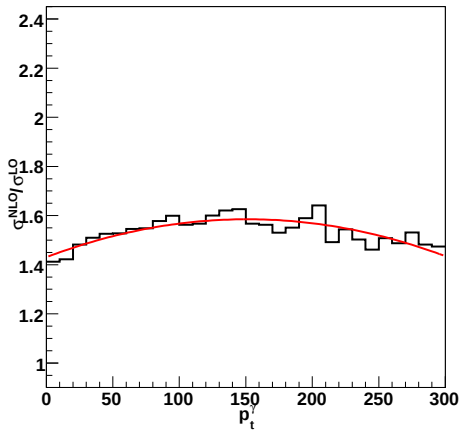

Figure 5.1: The k-factor for $W\gamma$ initial state radiation and the tri-linear coupling process.

5.2 Cross Section Measurement

The cross section times the branching ratio is calculated as

$$\sigma(p\bar{p} \to l\nu\gamma) = \frac{N_{data} - N_{BG}}{\mathcal{A} \times \epsilon \times \int \mathcal{L}dt}$$

where N_{data} is the number of data events, N_{BG} the number of background events, $\mathcal{A} \times \epsilon$ is the acceptance times the efficiency, and $\int \mathcal{L}dt$ is the integrated luminosity of the dataset.

The individual results are given for W+central photon (W decays to CEM, PHX electron or CMUP CMX muon) in Table 5.3, for W+ plug photon (W decays to CEM, CMUP, or CMX) in Table 5.4. The results for the full combined dataset are given in Table 5.5. Using photons with $E_T^\gamma > 15$ GeV and $|\eta^\gamma| < 2.0$ we obtain

$$\begin{aligned} \sigma(p\bar{p} \to W\gamma + X) \times \mathcal{B}(W \to l\nu) &= 7.36 \pm 0.35 \text{ (stat.)} \pm 0.75 \text{ (sys.)} \pm 0.43 \text{ (lumi.) pb} \\ &= 7.36 \pm 0.93 \text{ pb} \end{aligned}$$

The measurement agrees well with the Standard Model prediction of 8.2 ± 0.6 pb.

Figure 5.2 show the E_T^γ, $\Delta R(l,\gamma)$, the $M_T(l,\nu)$ and the cluster transverse mass, $M_T(l\gamma,\nu)$ distributions of W+ central photon. Figure 5.3 show distributions of W+ plug photon. The combined distributions of W+ central and plug photon are shown in Figure 5.4.

W+central photon	Number of Events
$W\gamma$	438.62±6.25(stat.)±11.27(sys.)
W+jet	125.21±0.33(stat.)±48.84(sys.)
$Z\gamma$	57.40±0.44(stat.)±1.55(sys.)
$W\gamma(\tau)$	8.75±0.88(stat.)±0.22(sys.)
Number of Total Expected Events	629.98±6.34(stat.)±51.27(sys.)
Number of Observed	549

Table 5.3: W+central photon: luminosity, number of data and background events for 1 fb^{-1} data.

W+plug photon	Number of Events
$W\gamma$	259.10±6.25(stat.)±6.80(sys.)
W+jet	11.11±0.55(stat.)±9.88(sys.)
$Z\gamma$	41.09±0.44(stat.)±1.14(sys.)
$W\gamma(\tau)$	6.95±0.88(stat.)±0.18(sys.)
Number of Total Expected Events	318.25±6.36(stat.)±12.78(sys.)
Number of Observed	328

Table 5.4: W+plug photon: luminosity, number of data and background events for 1 fb^{-1} data.

Combined Result(Central+Plug)	Number of Events
$W\gamma$	697.72±6.25(stat.)±17.63(sys.)
W+jet	136.31±0.28(stat.)±58.73(sys.)
$Z\gamma$	98.50±0.44(stat.)±2.43(sys.)
$W\gamma(\tau)$	15.70±0.88(stat.)±0.40(sys.)
Number of Total	948.23±6.34(stat.)±63.20(sys.)
Number of Observed	877

Table 5.5: $W + \gamma$ (Combined central + plug): luminosity, number of data and background events for 1 fb^{-1} data.

Anomalous couplings between the W boson and photons would result in an excess of the data compared to the Standard Model prediction at high E_T^γ. At high cluster transverse mass one could expect contributions from e.g. excited W bosons decaying to a photon and a W boson.

The data agree well with the Standard Model in all cases. The highest photon E_T event has $E_T^\gamma = 186$ GeV, and the highest mass event has Cluster transverse mass = 398 GeV.

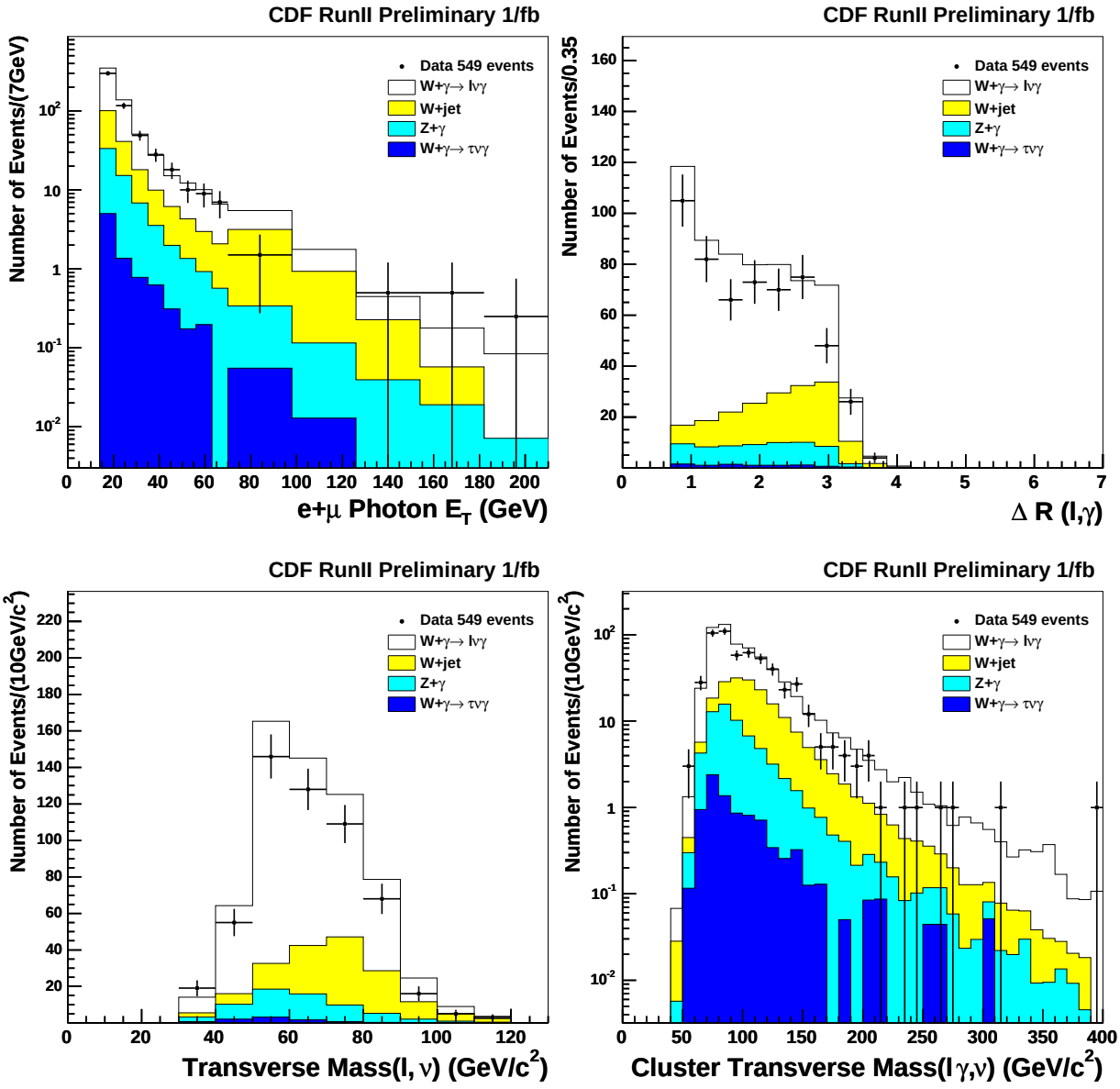

Figure 5.2: Central photon E_T, $\Delta R(\ell, \gamma)$, $M_T(\ell, \not\!\!E_T)$ and cluster transverse mass for 1 fb^{-1} data.

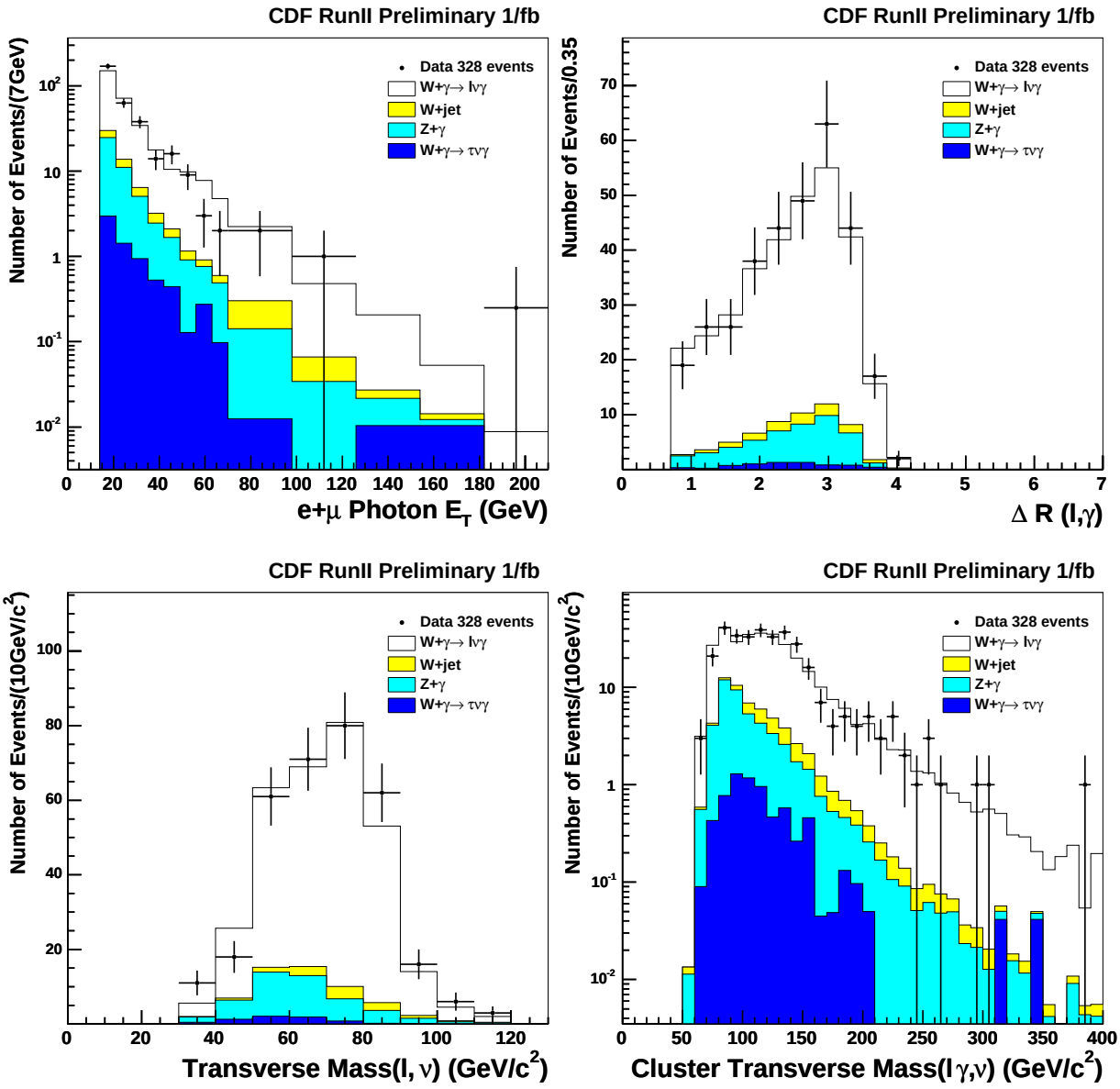

Figure 5.3: Plug photon E_T, $\Delta R(\ell, \gamma)$, $M_T(\ell, \not\!\!E_T)$ and cluster transverse mass for 1 fb^{-1} data.

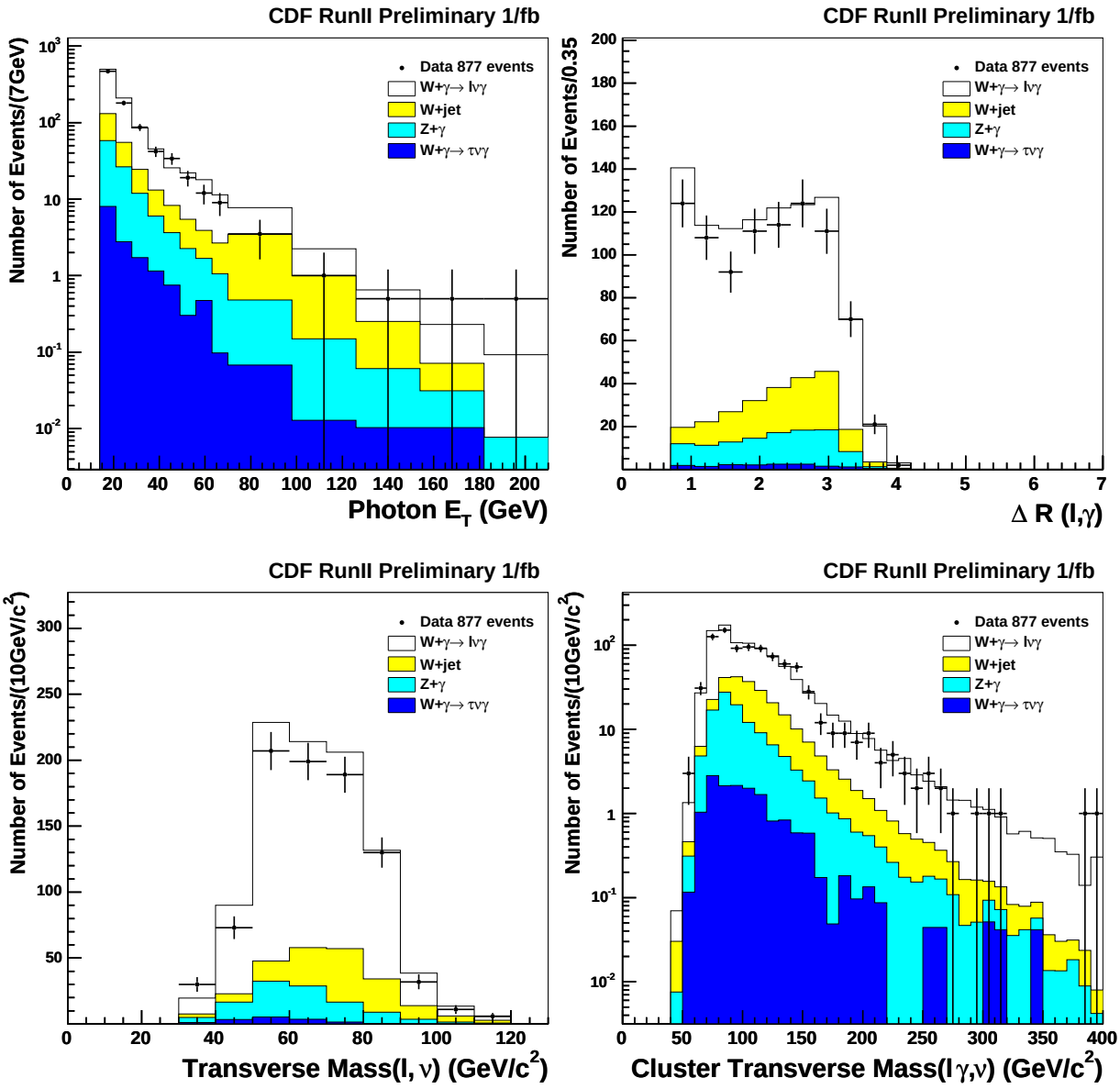

Figure 5.4: Combined photon of central and plug E_T, $\Delta R(\ell, \gamma)$, $M_T(\ell, \not\!\!E_T)$ and cluster transverse mass for 1 fb^{-1} data.

5.3 Cross Section Systematic Uncertainty

The following systematic uncertainties on the measurement are considered:

- A luminosity uncertainty of 5.8%. The uncertainty is dominated by the uncertainty in the absolute normalization of the CLC acceptance for a single $p\bar{p}$ inelastic collision.

- A 0.6% uncertainty on the lepton identification efficiencies [67].The detector simulation does not always give a good description of the detector response and as a consequence difference between data and Monte Carlo are observed.

- A 0.7% uncertainty on the lepton trigger efficiencies [67]. The data samples are collected via high p_T lepton only trigger path. The three level trigger system reduces the beam interaction rate into final event collection rate. The efficiency is determined from the product of the efficiencies measured for each of the levels. The measured efficiency for a specific level of the trigger is based on the subset of reconstructed track candidates that satisfy the trigger requirements of the levels beneath it.

- A 0.20% uncertainty on the track efficiency. The efficiency for the reconstructing the track of the high p_T lepton in the COT is required in this analysis. The tracking efficiency measurement is obtained from the fraction of events in $W \rightarrow e\nu$ sample which have a COT track pointing to the electromagnetic cluster.

- A 0.21% uncertainty on the luminosity contained outside the 60 cm window [69]. The fraction of $p\bar{p}$ collisions that occur within $\pm$60 cm of the center of the detector along the z-axis. We impose this requirement as a fiducial cut to ensure that $p\bar{p}$ interactions are well-contained within the geometrical acceptance of the detector. The z-coordinate of the event vertex for a given event is taken from the closest intersection point of the reconstructed high p_T lepton track with the z-axis. Since event selection criteria can bias our samples against events originating in the outer interaction region, the efficiency of our vertex position requirement is measured directly from the observed vertex distribution in minimum bias events.

- A 0.2% uncertainty on the electron energy scale results in a 1.2% uncertainty on the acceptance. The model of cluster E_T scale and resolution for the electromagnetic

sections of the calorimeter can change the acceptance estimates for the minimum cluster E_T requirements on electrons.

- A 1% uncertainty on the photon energy scale [70] results in a 1% uncertainty on the acceptance. Comparison of the $Z \to ee$ invariant mass distributions in the data and the simulation are used to tune the cluster E_T scale in the simulation. T

- A 3% uncertainty on the photon selection efficiency [68]. The photon reconstruction efficiency is measured using $Z\gamma \to \ell\ell\gamma$ decays. Events are based on the selection of a very pure photon source from final state radiation in $Z\gamma \to \ell\ell\gamma$. This measurement of photon selection efficiency is limited by statistics.

- A 0.5% uncertainty on the amount of photon conversions. A photon can lose a significant fraction of their energy prior to entering the calorimeter via conversion originating from interactions with detector material. The modeling of detector material in the simulation affects the estimation of photon conversion probability. Uncertainty arises from a 10% uncertainty on the detector material.

- A E_T^γ dependent systematic uncertainty on the rate of jets to fake photons. It ranges from 30% at low E_T^γ to 300% at high E_T^γ.

The resulting systematic uncertainty on the acceptance is 4.1% which directly translates into a 4.1% uncertainty on the cross section. The background uncertainty is about 30% resulting in a 13% uncertainty on the $W\gamma$ cross section.

The theoretical cross section prediction for $W\gamma$ production was evaluated to be 8.2$\pm$0.6 pb [66]: it has a 5% uncertainty due to the parton distribution functions and a 3% uncertainty due to higher order corrections.

Chapter 6

Conclusion

Associated production of the W boson and the photon in proton-antiproton collisions at a center-of-mass energy of 1.96 TeV has been studied. The data were collected and correspond to an integrated luminosity of 1 fb^{-1} using the CDF detector. The W boson is identified through its leptonic decay mode $W^{\pm} \rightarrow \ell^{\pm}\nu$, where $\ell^{\pm}$ is and electron or a muon. The photon is identified in the kinematic region $E_T > 7$ GeV and $\Delta R(\ell, \nu) > 0.7$, where $\Delta R = \sqrt{(\Delta\eta)^2 + (\Delta\phi)^2}$ is the distance between the lepton and the photon in η-ϕ space. The production cross section is measured to be

$$\sigma(p\bar{p} \rightarrow W\gamma + X) \times \mathcal{B}(W \rightarrow l\nu) = 7.36 \pm 0.93 \text{ pb}$$

It agrees well with the theoretical cross section of 8.2 ± 0.6 pb. Also the kinematic distributions such as the photon transverse energy, the ΔR, the transverse mass of the lepton and the neutrino and the cluster transverse mass of the photon, the lepton, and the neutrino are in good agreement with the Standard Model prediction.

Bibliography

[1] S.Weinberg, "A Model of Leptons", Phys. Rev. Lett., **19** (1967) 1264.

[2] A. Salam, "Elementary Particle Theory", **N.Svartholm** (1961).

[3] S.L. Glashow, "Weak Interactions with Lepton-Hadron Symmetry", Phys. Rev. D **2** (1970) 1285.

[4] M. Veltman, "Perturbation Theory of Massive Yang-Mills fields", Nucl. Phys. B **35** (1968) 637.

[5] G. 'tHooft, "Renormalizable Lagrangians for Massive Yang-Mills Fields", Nucl. Phys. B **35** (1971) 167.

[6] G. 'tHooft, "Combinatorics of Gauge Fields", Nucl. Phys. B **50** (1972) 318.

[7] M.Kobayashi and T. Masukawa, Prog. Theor. Phys. **49** (1973) 652.

[8] N. Cabibbo, Phys. Rev. Lett. **10** (1963) 531.

[9] K. Hagiwara, R.D. Peccei, D. Zeppenfield and K. Hikasa, "Probing the weak boson sector in $e^+e^- \to W^+W^-$", Nucl. Phys. B **282**, (1987) 253.

[10] U. Baur and D. Zeppenfield, "Probing the $WW\gamma$ vertex at future collider", Nucl. Phys. B **308** (1988) 127.

[11] K. Gaemers and G. Gounaris, Z. Phys. C **1** (1979) 259.

[12] U. Baur and E.L. Berger, "Probing the $WW\gamma$ vertex at the Fermilab Tevatron Collider", Phys. Rev. D **41**, 1476 (1990).

[13] J. Cortes, K. Hagiwara and F. Herzog, "Testing the $WW\gamma$ coupling of the standard model at $p\bar{p}$ colliders", Nucl. Phys. B **278**, (1986) 26.

[14] K.O. Mikaelian and M.A.Samuel, "Magnetic Moment of Weak Bosons Produced in pp and $p\bar{p}$ Collisions", Phys. Letter **11**, (1979).

[15] U. Baur, S. Errede, and G. Landsberg, "Rapidity correlations in $W\gamma$ production at hadron colliders", Phys. Rev. D **50**, 3 (1994).

[16] OPAL Collaboration, "Measurement of the triple gauge boson coupling $\alpha = W\phi$ from W^+W^- production in e^+e^- collisions at $\sqrt{s} = 161$ GeV", Phys. Lett. B **397**, (1997) 147.

[17] OPAL Collaboration, "Measurement of the triple gauge boson coupling from W^+W^- production at $\sqrt{s} = 172$ GeV", Eur. Phys. J. C. **2**, (1998) 597.

[18] OPAL Collaboration, "W^+W^- production and triple gauge boson couplings at LEP energies up to 183 GeV", Eur. Phys. J. C. **8**, (1999) 191.

[19] OPAL Collaboration, "W^+W^- production and triple gauge boson couplings at LEP energies up to 189 GeV", Eur. Phys. J. C. **19**, (2001) 1.

[20] DELPHI Collaboration, "Measurement and interpretation of the W-pair cross-section in e^+e^- interactions at $\sqrt{s} = 161$ GeV.", Phys. Lett. B. **397**, (1997) 158.

[21] DELPHI Collaboration, "Measurement of tri-linear gauge couplings in e^+e^- interactions at 161 GeV and 171 GeV.", Phys. Lett. B. **423**, (1998) 194.

[22] DELPHI Collaboration, "Measurement of the trilinear gauge couplings $WWV(V \equiv \gamma, Z)$ in e^+e^- collisions at 183 GeV.", Phys. Lett. B. **459**, (1999) 382.

[23] DELPHI Collaboration, "Measurement of the triple-gauge boson couplings of the W boson at LEP.", Phys. Lett. B. **467**, (1999) 171.

[24] DELPHI Collaboration, "Measurement of the trilinear gauge couplings $WWV(V \equiv \gamma, Z)$ in e^+e^- collisions at 189 GeV.", Phys. Lett. B. **502**, (2001) 9.

[25] L3 Collaboration, "Pair production of W bosons in e^+e^- interactions at $\sqrt{s} = 161$ GeV.", Phys. Lett. B. **398**, (1997) 223.

[26] L3 Collaboration, "Measurements of mass, width and gauge couplings of the W boson at LEP.", Phys. Lett. B. **413**, (1997) 176.

[27] L3 Collaboration, "Measurement triple-gauge-boson couplings of the W boson at LEP", Phys. Lett. B. **467**, (1999) 171.

[28] L3 Collaboration, "Production of single W bosons in e^+e^- interactions at LEP.", Phys. Lett. B. **403**, (1997) 168.

[29] L3 Collaboration, "Production of single W bosons in e^+e^- interactions at $130 < \sqrt{s} < 183$ GeV and limits on anomalous $WW\gamma$ couplings", Phys. Lett. B. **426**, (1998) 417.

[30] L3 Collaboration, "Production of single W bosons at $\sqrt{s} = 189$ GeV and measurement of $WW\gamma$ gauge couplings", Phys. Lett. B. **487**, (2000) 229.

[31] L3 Collaboration, "Production of single W bosons at LEP and measurement of $WW\gamma$ gauge coupling parameters", Phys. Lett. B. **547**, (2002) 151.

[32] ALEPH Collaboration, "Measurement of trilinear gauge-boson couplings of the W boson at LEP. ", Phys. Lett. B. **422**, (1998) 369.

[33] ALEPH Collaboration, "Measurement of triple gauge-boson couplings at LEP energies up to 189 GeV. ", Eur. Phys. J.C. **21**, (2001) 423.

[34] ALEPH Collaboration, "A study of single W production in e^+e^- collisions at $\sqrt{s} = 161$-183 GeV. ", Phys. Lett. B. **462**, (1999) 389.

[35] ALEPH Collaboration, "Measurement of triple gauge WW couplings at LEP2 using photonic events. ", Phys. Lett. B. **445**, (1998) 239.

[36] OPAL Collaboration, "Measurement of charged current triple gauge boson couplings using W pairs at LEP ", Eur. Phys. J.C. **33**, (2004) 463.

[37] G. Gaunaris, "Triple Gauge Boson Couplings ", Eur. Phys. J.C. **33**, (2004) 463.

[38] LEP Collaboration, "A Combination of Preliminary Electroweak Measurements and Constrains on the Standard Model ", CERN-EP/2003-091, hep-ph/0312023.

[39] CDF Collaboration, "Measurement of W-Photon Couplings in p-$\bar{p}$ Collisions at $\sqrt{s} = 1.8$ TeV. ", Phys. Rev. Lett. **74**, (1995) 1936.

[40] CDF Collaboration, "Limits on WWZ and $WW\gamma$ Couplings from WW and WZ production in $p\bar{p}$ Collisions at $\sqrt{s} = 1.8$ TeV. ", Phys. Rev. Lett. **75**, (1995) 1017.

[41] DØ Collaboration, "Limits on anomalous WWZ and $WW\gamma$ couplings. ", Phys. Rev. Lett. **58**, (1998) 031102.

[42] DØ Collaboration, "Limits on anomalous WWZ and $WW\gamma$ couplings. ", Phys. Rev. Lett. **58**, (1998) 031102.

[43] DØ Collaboration, "Limits on anomalous WWZ and $WW\gamma$ couplings from W boson pair production. ", Phys. Rev. Lett. **58**, (1998) 051101.

[44] DØ Collaboration, "Studies of WW and WZ production and limits on anomalous $WW\gamma$ and WWZ couplings. ", Phys. Rev. D. **60**, (1999) 072002.

[45] DØ Collaboration, "Limits on anomalous WWZ and $WW\gamma$ couplings from $WW/WZ \rightarrow e\nu jj$ production. ", Phys. Rev. D. **62**, (2002) 052005.

[46] A. Pich "The Standard Model of Electroweak Interactions", arXiv:0705.4264v1 [hep-ph]

[47] J. Sjorlin *et al.* (CDF collaboration), "Limits on Anomalous Triple Gauge Couplings in ppbar Collisions at $\sqrt{s}$=1.96 TeV", arXiv:0705.2247v2 [hep-ex].

[48] V. M. Abazov *et al.* (DØ collaboration), "Measurement of the $p\bar{p} \rightarrow W\gamma + X$ cross section at $\sqrt{s}$=1.96 TeV and WWγ anomalous coupling limits", Phys. Rev. D 71 , 091108 (2005)

[49] F. Abe *et al.*, "THE CDF DETECTOR: AN OVERVIEW. FERMILAB-PUB-88-25-E, Feb 1988. 40pp", Nucl.Instrum.Meth.A271:387-403,1988.

[50] C. S. Hill *et al.*, "L00: Operational Experience and Performance of the CDFII Silicon Detector", Nucl. Instrum. Meth. A530:1-6, 2004.

[51] A. Sill. *et al.*, "SVX-II: CDF Run II Silicon Tracking Projects", Nucl. Instrum. Meth. A447:1-8, 2000.

[52] A. Affolder *et al.*, "ISL: Intermediate Silicon Layers Detector for the CDF Experiment", Nucl. Instrum. Meth. A453:84-88, 2000.

[53] T. Affolder *et al.*, "COT Central Outer Tracker", Nucl. Instrum. Meth. A526: 249, 2004.

[54] L. Balka *et al.*, "THE CDF CENTRAL ELECTROMAGNETIC CALORIMETER", Nucl.Instrum.Meth.A267:272,1988

[55] S. Bertolucci *et al.*, "THE CDF CENTRAL AND ENDWALL HADRON CALORIMETER.", Nucl.Instrum.Meth.A267:301,1988.

[56] Y. Fukui *et al.*, "CDF END PLUG ELECTROMAGNETIC CALORIMETER USING CONDUCTIVE PLASTIC PROPORTIONAL TUBES.", Nucl.Instrum.Meth.A267:280,1988.

[57] G. Ascoli,*et al.*, "CDF CENTRAL MUON DETECTOR. FERMILAB-PUB-87/179-E, Jul 1987. 33pp.", Nucl.Instrum.Meth.A268:33,1988

[58] D. Acosta *et al.*, "The CDF Luminosity Monitor", Nucl.Instrum.Meth.A461:540-544,2001

[59] http://www-cdf.fnal.gov/internal/dqm/goodrun/v17/goodv17.html

[60] U. Baur and E.L. Berger, "Probing the weak-boson sector in $Z\gamma$ production at hadron colliders", Phys. Rev. D **47**, 4889 (1993).

[61] U. Baur, T. Han and J. Ohnemus, "QCD corrections to hadronic W gamma production with nonstandard W W gamma couplings," Phys. Rev. D **48**, 5140 (1993).

[62] U. Baur, T. Han and J. Ohnemus, "QCD corrections and Anomalous Couplings in $Z\gamma$ Production at Hadron Colliders", Phys. Rev. D **57**, 2823 (1998).

[63] A. Abulencia *et al.* (CDF collaboration), Phys. Rev. Lett. 94, 091803 (2005).

[64] E.L. Berger *et al.* "The minimum invariant mass - A Technique for heavy quark searches at collider energy." , Phys. Lett. **140B**, 259 (1984).

[65] A. Nagano *et al.* CDF note 8516.

[66] D. Benjamin *et al.*, CDF note 6619.

[67] U. Grundler *et al.*, CDF note 7956 and CDF note 8262.

[68] J. Deng *et al.* CDF note 8889.

[69] W. Sakumoto, CDF note 8318.

[70] A. Bhatti, F. Canelli, B. Heinemann *et al.*, "Determination of the Jet Energy Scale at CDF", Nucl. Instr. Methods A**566**, 375-412 (2006).

[71] Andrew W. Askew *et al.*,"Measurement of the $W\gamma \rightarrow \mu\nu\gamma$ cross section, Limits on Anomalous Trilinear Vector Boson Couplings, and the Radiation Ampliude Zero in $p\bar{p}$ Collisions at $\sqrt{s} = 1.96$ TeV".